CFD modeling and analysis of anode supported solid oxide fuel cells

by

Ahmed Khaled Elkashat

A thesis submitted in partial fulfillment of the requirements for the degree of

Master of Science

Department of Mechanical Engineering
University of Alberta

Abstract

Solid Oxide Fuel Cells (SOFCs) are promising energy conversion devices that offer high efficiency and low environmental impact. In order to understand and accurately estimate the SOFCs performance, advanced modeling techniques are required due to SOFCs complicated multi-physics nature and complex fluid flow patterns. This thesis focuses on adopting a computational fluid dynamics (CFD) analysis approach to study the performance of SOFCs in terms of electrical power output, thermal gradients across the cell, and fuel and oxidant consumption through the cell's gas channels.

Two different three-dimensional models were developed and experimentally validated for tubular and planar SOFCs. The effect of the cell's operating conditions and structure properties on its performance was studied. Additionally, the planar cell thermal gradients as a function of the operating conditions were studied.

The results show the effect of operating temperature on cell performance and the hydrogen and oxygen mass fraction across the fuel and air channels, respectively, for both tubular and planar models.

Finally, a parametric analysis was conducted to study the effect of the cell's structure parameters, such as anode porosity, anode thickness, and electrolyte thickness, on the tubular and planar cells' performance. Additionally, the effect of changing operating parameters such as the inlet temperature and flow rate of fuel and oxidant on the thermal gradient across the planar cell

Preface

This thesis is submitted for the master's degree at the University of Alberta. The research described herein was conducted under the supervision of Dr. Mahdi Shahbakhti in the Department of Mechanical Engineering between May 2021 and July 2023. The design of experiments was done by Ahmed ElKashat, while the majority of laboratory work for the SOFC instrumentation and the test setup development was done by Dr. Amir Hanifi, Dr. Sajad Vafaeenezhad, and Shakiba Sharifi. All the modeling work was conducted by Ahmed ElKashat.

Part of this work has been included in the following publication, in which the six-page paper has been presented in The Canadian Society for Mechanical Engineering located at the University of Alberta in 2022:

ElKashat AK, Razmi AR, Vafaeenezhad S, Hanifi AR, Etsell TH, Shahbakhti M. Experimental and thermodynamic analyses of a novel anode supported solid oxide fuel cell.

Acknowledgements

The culmination of an ongoing process of academic exploration and personal development is this thesis. I am thrilled and honoured to share this work, which is the result of weeks, months, or even years of hard effort, study, and reflection.

I would like to extend my sincere appreciation to everyone who has supported me along the way. I would like to start by expressing my gratitude to my thesis supervisor, Dr. Mahdi Shahbakhti, for his great advice, knowledge, and persistent dedication to my accomplishment. His support and intelligent criticism were crucial in helping me shape my work and push myself to the limit. And special thanks to Dr. Amir Hanifi for his dedication, guidance, and support. Last but not least, thanks to Dr. Sajad Vafaeenezhad and Shakiba Sharif for their unconditional assistance in providing the needed data for this thesis.

Furthermore, I would like to express my heartfelt appreciation to my family, especially my wife, my daughter, my son, and my parents, for being a continual source of encouragement, inspiration, and understanding throughout this challenging journey.

This thesis represents an significant milestone in my academic career both personally and intellectually. My goal is that this work will further contribute to the body of knowledge in its sector and encourage additional research.

Despite making every effort attempts to ensure the accuracy and validity of the data presented here, I recognise that research is a continuous process with potential gaps and opportunities for improvement. I encourage further academic study and research to expand on this work and pursue novel avenues of exploration.

Table of Contents

List of Tables

List of Figures

List of Symbols

$\dot{m}$	Mass flow rate (kg/s)
$\dot{v}$	Volume flow rate (SCCM)
a	Stoichiometric Coefficient
C_p	Specific Heat Capacity ($J/kg.K$)
D_{eff}	Effective Diffusivity Coefficient
D_{ij}	Diffusion Coefficient in the bulk fluid
F	Faraday's constant (96400 $coulomb/mole$)
h	Enthalpy of Species (J/mol)
i	Current Density (A/cm^2)
i_0	Exchange Current Density (A/cm^2)
K	Coefficient of Thermal Conductivity ($W/m.K$)
k_g	Gas Phase Permeability (m^2)
n	Number of electrons transferred during the electrode reaction
p	Pressure (Pa)
Q	Heat generation (W)
R	Gas Constant (8.314 $J/mol.K$)
R_{ohmic}	Ohmic Resistance (Ω)
S	Energy Source or Sink (J)
T	Temperature (K)
U	Utilization factor
V	Cell Output Voltage (V)
x	Species Mole Fraction

y Species Mass Fraction

Greek

α Anodic and cathodic Transfer Coefficient

δ layer Thickness (μm)

η Cell Overpotential (V)

γ Concentration Dependence

μ Gas Viscosity (kg/ms)

ϕ Electrical Potential (V)

ρ Material Density (kg/m^3)

σ Electrical Conductivity ($\Omega^{-1}m^{-1}$)

τ Tortuosity

ε Material Porosity

$\vec{v}$ Velocity Vector

Subscripts

a Air

act Activation Losses

con Concentration Losses

eff Effective property

$elec$ Electrolyte

f Fuel

i Specie i

j Specie j

$ohmic$ Ohmic Losses

Superscripts

$\circ$ Standard or Reference State

Abbreviations

AFC Alkaline Fuel cell.

AS Anode-supported.

CFD Computational Fluid Dynamics.

CRO rare earth doped ceria.

CS Cathode-supported.

DOE Department of Energy.

EIS Electrochemical Impedance Spectroscopy.

ES Electrolyte-supported.

Gtoe Gigatons of Oil Equivalent.

IEA International Energy Agency.

LSGM lanthanum strontium magnesium galate perovskite.

MCFC Molten Carbonate Fuel Cell.

OCV Open Circuit Voltage.

PAFC Phosphoric Acid Fuel Cell.

PEMFC Polymer Exchange Membrane Fuel Cell.

SEM Scanning Electron Microscopy.

SOFC Solid Oxide Fuel Cell.

SSZ scandia stabilized zirconia.

YSZ yttria stabilized zirconia.

Chapter 1

Introduction

Nowadays, energy security and strengthened climate policies present the biggest global challenges. Based on the International Energy Agency's (IEA) World Energy Outlook 2022, the global energy consumption has grown between 2010 and 2019 by an average rate of 1.4% per year. Due to the COVID-19 pandemic, the energy consumption reduced by 3% in 2020. The global economic recovery played a great role in increasing the consumption by about 5% in 2021 and 2.1% in 2022 to cause about 11.8 Gtoe. These led to 6.3% increase in CO_2 emissions in 2021 and 1.9% increase in 2022, causing about 28.3 $GtCO_2$ [1]. A large number of studies have been conducted to develop and enhance power generation technologies. Fuel cells supplied by green hydrogen have gained significant attention because of their great potential for electricity generation with high efficiency and the decarbonization of global energy systems.

1.1 Fuel Cell Background

A fuel cell is an energy conversion device. It converts energy from one form to another. More specifically, a fuel cell converts the chemical energy stored in the fuel to electric and thermal energy without combustion. Over 150 years ago, fuel cells were first developed. The British chemist Humphry Davy was the first person who described the fuel cell scientific concepts in 1801 [2]. Then the German-Swiss chemist Christian Friedrich described the electrochemical reaction between hydrogen and oxygen inside the fuel cell in 1838 [3]. In 1842, the Welsh chemical physicist William Robert Grove was the first to use platinum electrodes, hydrogen, and oxygen to produce electricity; this fuel cell prototype was called a gas voltaic battery [4].

In 1889, Charles Langer and Ludwig Mond were the first to introduce the term "fuel cell" by developing a fuel cell fed by air and industrial coal gas [5].

In the 1930s, the British chemical engineer Francis Bacon resumed Langer and Ludwig's work and developed a 5 KW alkaline fuel cell in 1950. After that, NASA used the first alkaline fuel cell on Apollo space missions in the 1960s [6]. In 1959, Willard Thomas Grubb and Leonard Niedrach invented the proton exchange membrane fuel cell, the commonly used fuel cell type nowadays [7]. In 1966, General Motors invented the first concept car powered by a fuel cell; it was called the Electrovan [8]. In the 1970s and 1980s, formidable efforts were made to reduce the reliance on imported petroleum. The United States Navy considered using fuel cells in submarines because of their high efficiency, zero emissions, and near-silent operation [9]. In the 1990s, attention turned to fuel cell technology to be used in supplying energy to residential micro-combined heat and power systems.

In the 2000s, fuel cells started to spread in various transportation applications in different vehicle types, such as trains, buses, forklifts, boats, and motorcycles. In 2014, Toyota introduced the first commercial fuel cell car that used hydrogen as its fuel. Toyota named this car Mirai, which is a Japanese word that means "future" [10].

Fuel cells are classified based on the kind of electrolyte they use. This classification not only specifies the type of electrochemical processes that occur in the cell, but also the types of catalysts that are needed, the fuel cells' operating temperature range, the fuel required, and other factors. These properties have an impact on the applications that these cells are best suited for.

The following is a list of the five most common types of fuel cells:

- Polymer Exchange Membrane Fuel Cell (PEMFC)
- Alkaline Fuel cell (AFC)
- Solid Oxide Fuel Cell (SOFC)
- Phosphoric Acid Fuel Cell (PAFC)
- Molten Carbonate Fuel Cell (MCFC)

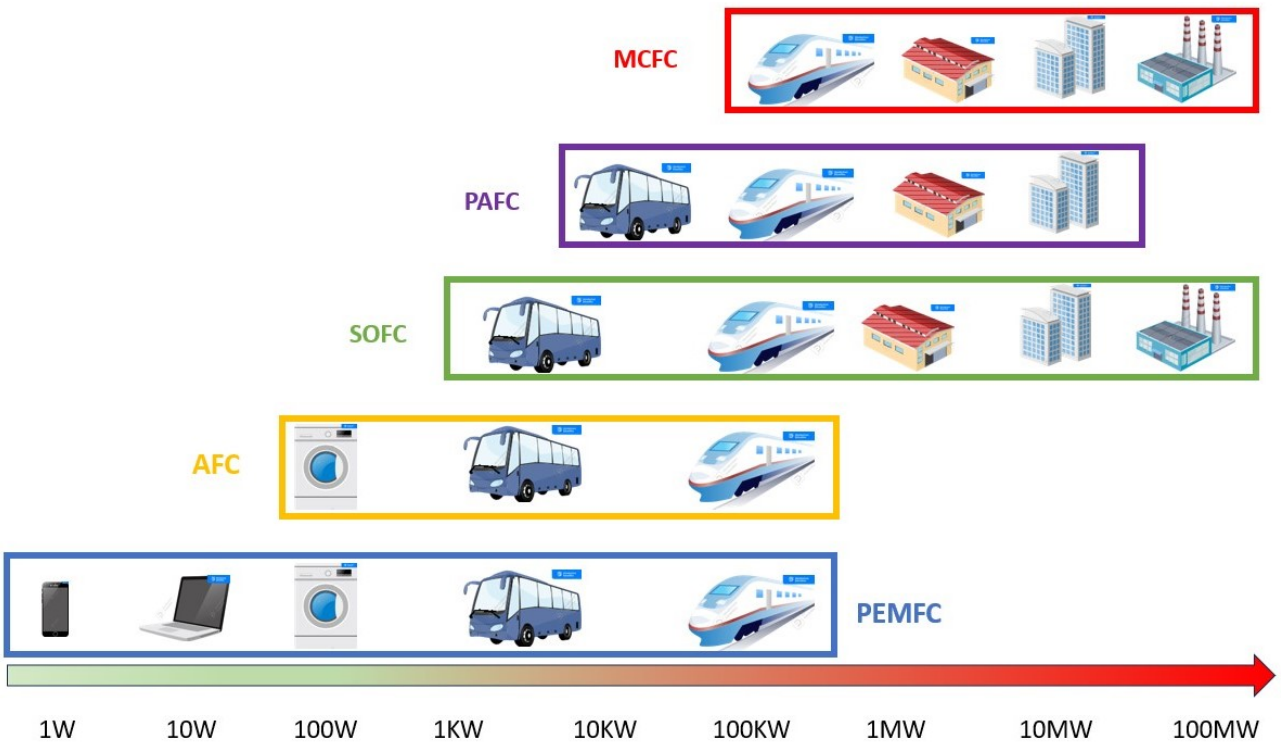

Figure 1.1: Fuel cell types' power range and suitable applications.

Figure 1.2 shows the products, reactants, and operation temperatures of different fuel cell types and how charge carriers transfer through their electrolytes [11]. As a result of solid oxide and molten carbonate fuel cells' significant high operating temperature, they have different operating principles and have diverse applications. Typically, pure hydrogen is used as the fuel in low temperature fuel cells, which means that all fuel must first be converted to hydrogen

before being supplied into the low temperature fuel cells such as the PEMFCs. Compared to low-temperature fuel cells, one of the advantages of high-temperature fuel cells such as SOFCs and MCFCs is that they have the ability to internally convert CO or other hydrocarbon fuels to hydrogen.

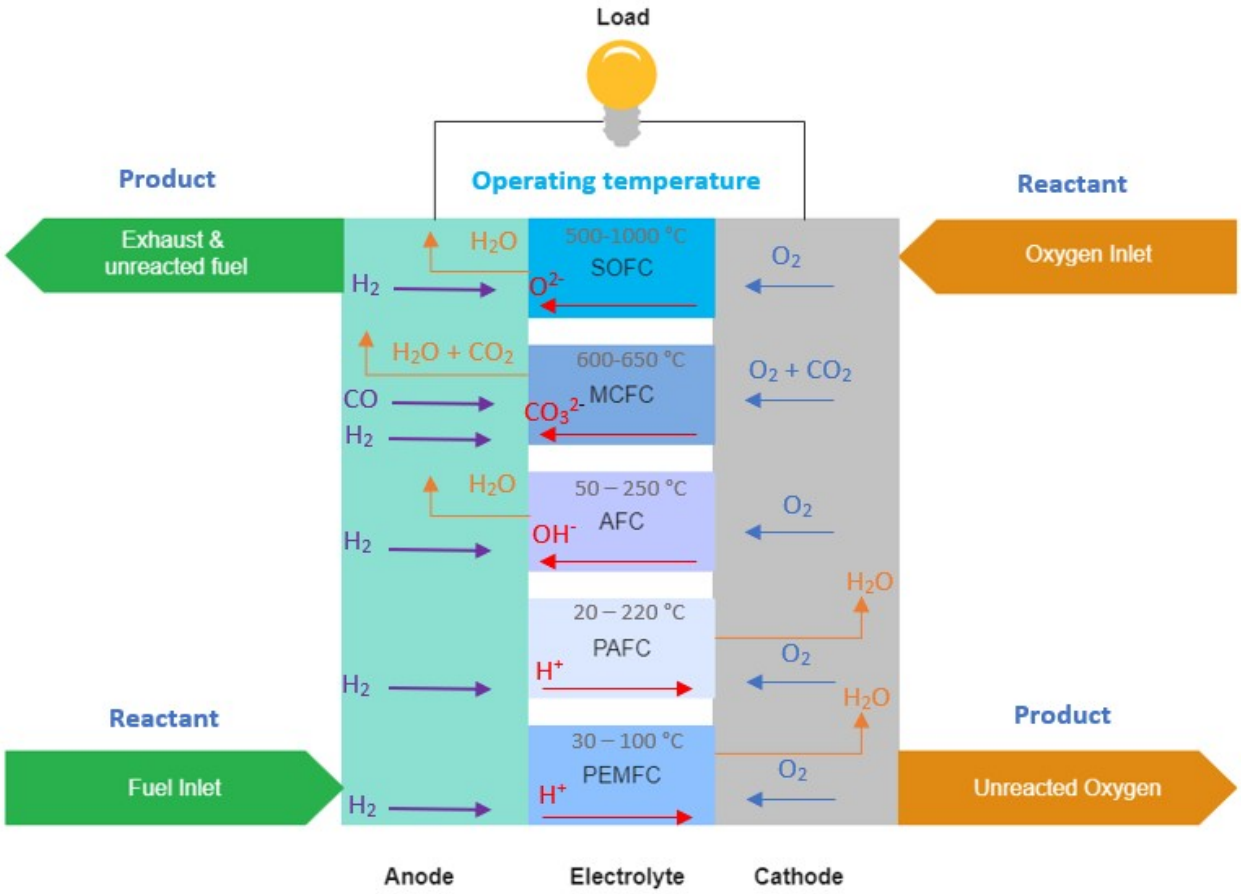

Figure 1.2: Comparison of the five types of fuel cells.

1.2 Solid Oxide Fuel Cell (SOFC)

The solid oxide fuel cell earned its name, because it is a solid-state device and all of its components are solid by nature. The issues of corrosion, electrolyte management, and transportation are significantly reduced with the elimination of liquid electrolyte. SOFC is an electrochemical energy-conversion technology that holds great potential for producing clean, efficient electricity while also offering major environmental advantages when it comes to fuel flexibility [12]. As mentioned before, SOFC is a high-temperature technology; the current operating temperature of the SOFC is between 500 and 1000 °C. The high operating temperature provides a combination of challenges and benefits. Issues with cell interconnect, sealing, and stack hardware are among the challenges. Moreover, the cells have a high degradation rate, mechanical instability, and thermal expansion matching problems. On the other hand, it has a number of benefits, including high efficiency, the ability to use waste heat for heating applications, and fuel flexibility [13]. Table 1.1 shows the advantages and disadvantages of SOFC:

Table 1.1: Advantages and disadvantages of SOFCs.

Advantages	**Disadvantages**
• Solid-state	• High degradation rate
• No need for precious metals, corrosive acids, or molten, materials	• Sealing problems
• Fuel flexibility, the cell can be supplied with natural gas or hydrogen	• Thermal expansion compatibility problems
• High-quality waste heat for heating applications because its high operating temperature > 500 °C	• Long start-up time

1.2.1 SOFC principles

SOFC contains a dense electrolyte layer that is placed between two porous electrodes as shown in figure 1.3, the anode and cathode. Fuel, typically hydrogen, is fed to the anode side where the hydrogen oxidation reaction takes place while the oxidant, typically air, is fed to the cathode where the oxygen reduction reaction takes place. The electrodes are solid porous structures that permit the diffusion of fuel and air to the electrolyte as well as the diffusion of the by-products of the electrochemical reaction on the anode side away from the electrolyte. The oxygen ions produced from the oxygen reduction reaction at the cathode side migrate through the electrolyte to the anode side, where they react with the hydrogen molecule to produce water vapour and release electrons that produce electricity when they are transported through an external circuit [14]. Figures 1.3 and 1.4 show SOFC components and how molecular flows through the cell.

The chemical reactions of SOFC are [15]:

Overall reaction:

$$H_2 + 1/2\ O_2 \rightarrow H_2O \tag{1.1}$$

Hydrogen oxidation reaction:

$$H_2 + O^{2-} \rightarrow H_2O + 2e^- \tag{1.2}$$

Oxygen reduction reaction:

$$1/2\ O_2 + 2e^- \rightarrow O^{2-} \tag{1.3}$$

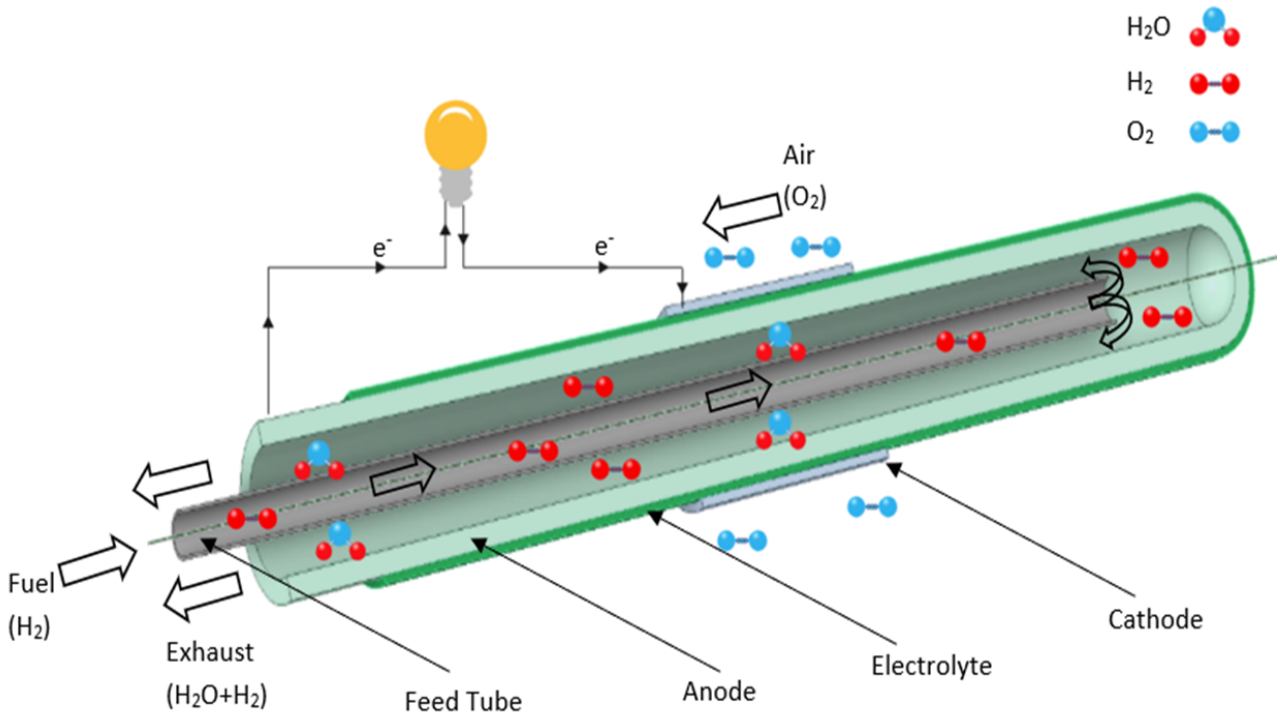

Figure 1.3: Operating principle of SOFC.

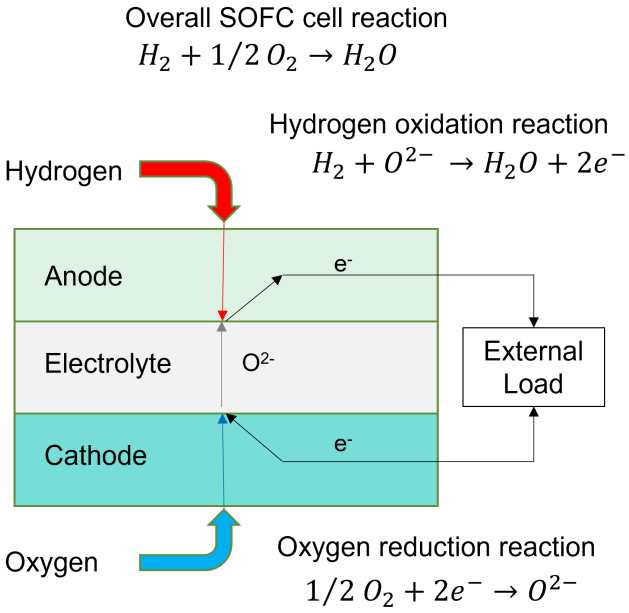

Figure 1.4: SOFC reactions and electrons transfer.

1.2.2 SOFC classifications

From a geometrical point of view, SOFC configurations can be classified into planar or tubular types. Although both types have the same operating concepts, each geometry type has its own advantages and disadvantages. The planar cell provides a relatively simple design and higher volumetric power densities; however, it has more sealing problems, a thermal expansion mismatch, and cracking potential. The tubular cell design is mechanically robust, can withstand thermal stresses, and has better sealing; on the other hand, it has a longer current path, which increases the ohmic resistance [16]. Figure 1.5 illustrates the two types of SOFC geometry configurations:

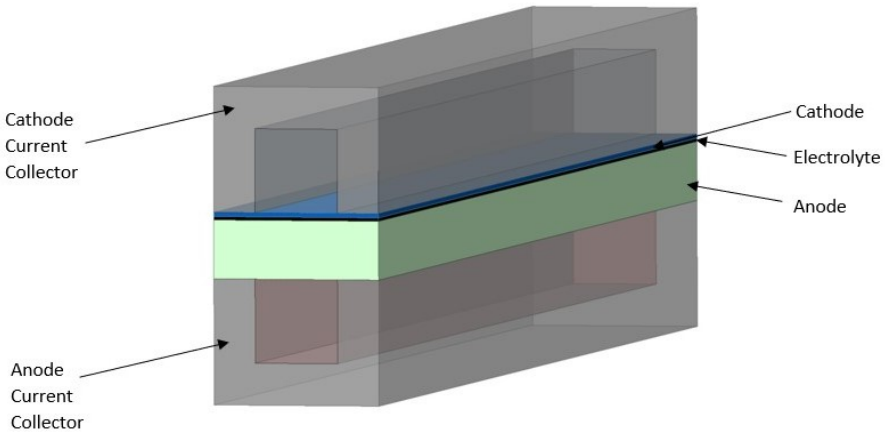

(a) Planar

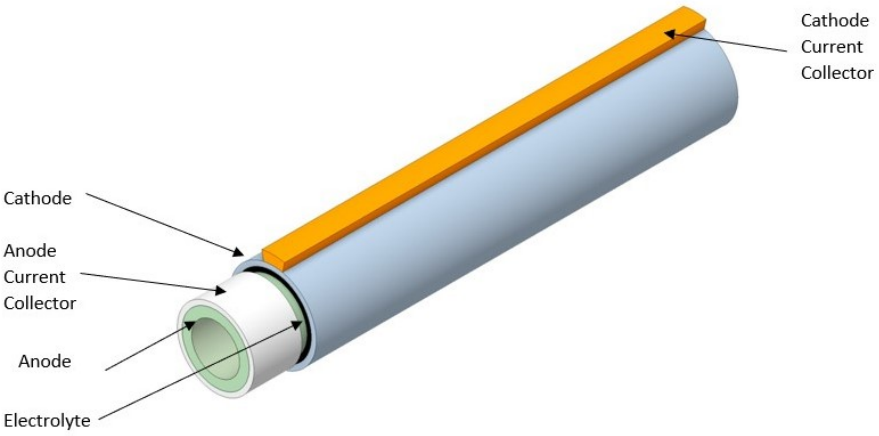

(b) Tubular

Figure 1.5: Schematic diagrams of (a) Planar and (b) Tubular type geometries of SOFCs.

SOFC are classified according to whether they are self-supporting or externally supported. This study focuses only on the self-supporting SOFC. In a self-supporting SOFC, the electrolyte, anode, or cathode represent the supporting element. Figure 1.6 illustrates the schematic for the three different SOFC supporting components. The electrolyte-supported (ES) design has a relatively thicker electrolyte, which increases the cell's strength and decreases the probability of mechanical failure; however, the thick electrolyte layer increases the internal resistance sharply [17]. The cathode-supported (CS) cell is not commonly used because it has a relatively low power density, but it has better phase stability [18]. Lastly, the anode-supported (AS) design is considered in this study for experiments and modeling. It has a cheaper design and relatively high conductivity. However, it has some significant issues, such as anode re-oxidation and the limitation of the transfer of gases because of the thick anode layer [19]. Table 1.2 presents some of the advantages and disadvantages of SOFC with different self-supporting elements [20].

Table 1.2: SOFC with different self-supporting elements features.

SOFC Supporting Type	Advantages	Disadvantages
Electrolyte-Supported (ES)	• Relatively stronge structure • Less failure probability due to anode reoxidation	• High ohmic resistance • Needs to be operate at higher temperature (above 800 °C)
Cathode-Supported (CS)	• No oxidation problems • Low operating temperature (from 800 °C to 1000 °C)	• Mass transport limitation • Low conductivity
Anode-Supported (AS)	• Higher conductivity • Lower operating temperature (below 800 °C)	• Mass transport limitation • Anode reoxidation problems

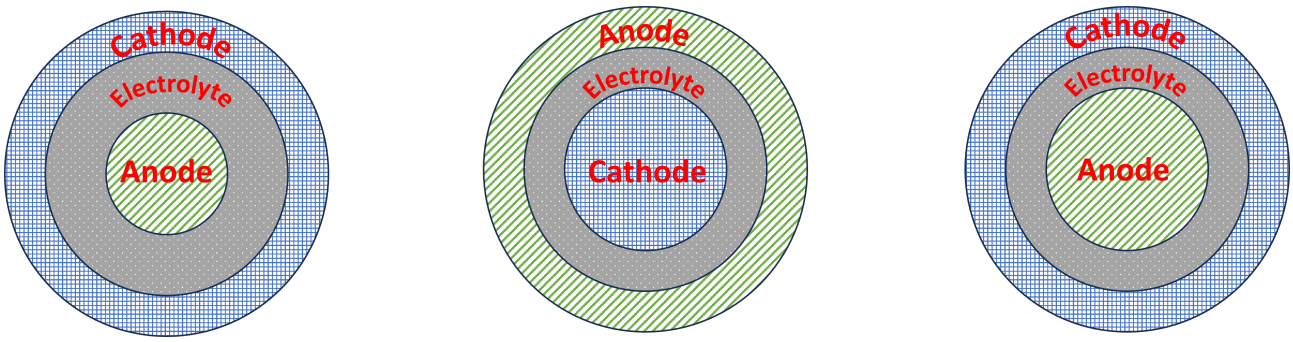

Figure 1.6: Schematics of different types of self-supporting components in SOFCs.

1.2.3 SOFC materials

SOFC material selection for the electrodes and electrolyte has been extensively studied since 1960s. Because its high operating temperature, the main goal of material selection studies is to find the materials that can provide a cheaper cost, better stability, and less degradation rate. In 1966, General Electric studies and designed a SOFC cell with $ZrO_2 - CaO$ or $ZrO_2 - Y_2O_3$ tubular electrolyte, carbon anode, and impregnated liquid silver cathode with porous zirconia. This cell was supplied with CH_4 as its fuel [21]. In 2002, Dokiya investigated the development of cheap, compact size, reduced temperature, and the feasibility of anode supported SOFCs by investigating the usage of four different electrolyte types: SSZ, YSZ, CRO, and LSGM [22]. In 2005, Kendall discussed the progress in solid oxide fuel cell materials as materials become more widely available; anodes composed mostly of ceramics made of nickel and yttria-stabilized zirconia (YSZ). To reduce its internal resistance, this cermet anode is now frequently utilised as the support material and has a thin coating of YSZ printed on it [23]. In 2015, Mahato et al considered the ceria-impregnated Ni-YSZ as the best choice of anode material because it has a high melting point (1453 °C) and is immune to sulfur poisoning caused by using hydrocarbon fuels [24]. In 2020, Hussain and Yangping published a report to review the most recent used materials for anode, cathode, and electrolyte SOFCs manufacturing and the importance of developing nanostructure which can reduce the SOFC operating temperature and the operating cost as well [25].

Microstructure properties of SOFCs has been studied extensively throughout the last two decades. In 2003, Lee et al investigated the impact of anode substrate microstructure on the SOFC electrical conductivity, gas permeability, polarization loss, and power-generating characteristics [26]. Zhenjun Jiao et al explained SOFC Ni-YSZ Anode microstructure degradation how it increases anode-reference polarization impedance and ohmic resistance [27].

1.3 SOFC research goals and modeling importance

Although SOFC has great potential, it still has many limitations and challenges. The main reason for these limitations and challenges is the high operating temperature. The thermal management, the mass and current transport across the cell, and reducing the operating temperature represent the main challenges. The United States Department of Energy (DOE) has set a number of goals to track the progress toward achieving SOFC design development. These goals are listed below [28]:

- Achieve SOFC efficiency[1] up to 60%
- Achieve a proven lifetime of 40,000 hours or more
- Achieve degradation rate less than 0.2 percent per 1,000 hours
- Achieve SOFC stack cost lower than $225/kilowatt

Mathematical and computational models provide a powerful tool for designing, predicting, and evaluating the performance of SOFCs. The importance of the models comes from the fact that they can avoid costly design changes, expensive experimental evaluation techniques, and increase the confidence of the design phase. For example, after the model is validated, we can run the model at various operating conditions and evaluate the cell performance with much less time and cost compared to the experimental methods; moreover, the models can be used to study the effectiveness of design changes before consuming time and resources to apply them in reality.

[1] The cell's electrical efficiency without applying the carbon capture techniques

The main goals of this CFD model are to predict the products and reactants concentration distributions, heat and mass transfer across the cell, the current density distribution, the temperature distribution, and the polarization curve. Two different models have been developed in this thesis: one is for anode-supported tubular SOFC fabricated in-house, and the other is for planar commercial anode-supported tubular SOFC. These models are used to carry out parametric analysis for various structure and operation parameters to optimise the SOFC design, which could provide better performance and a lower degradation rate.

1.4 Literature review

This section seeks to highlight current research, significant findings from earlier literature, and how this thesis can provide a fresh perspective on understanding SOFC. This thesis literature review is based on two main streams: experimental research and modeling research, which is divided into zero-dimensional modeling (0-D) and multi-dimensional modeling (2-D and 3-D).

Figure 1.7: Prior Zero-dimensional and multi-dimensional modeling work in the SOFC literature.

1.4.1 Zero-dimensional modeling (0-D)

This section provides an overview of works on the zero-dimensional mathematical modeling of tubular and planar designs of solid oxide fuel cells (SOFCs). Both configurations are broken down into four subsystems in this work, and internal operations including mass, energy, and momentum transfer, diffusion via porous media, electrochemical reactions, and polarisation losses are discussed. The zero-dimensional mathematical modeling considers the system as one point; although it does not take into account the system geometry, unlike the multi-dimensional models, it is fast and could be used for control applications and real-time fault diagnostics.

Izzo Jr et al. [39] investigated the diffusion of gas through the porous anode of an anode-supported tubular SOFC and the subsequent gas flow across it. The diffusion equations for the porous anode layer depend on the experimentally determined micro-structural parameters porosity, tortuosity, and effective diffusion coefficients. The results showed the diffusion rate in the anode layer plays a crucial part in how well a tubular SOFC performs. Also demonstrated a low concentration of hydrogen and a high concentration of water at the reactive triple phase boundary (TPB), where the ion-conducting phase of the electrolyte, the electron-conducting phase, and the gaseous fuel phase come together in the fuel stream, causing a low cell output voltage. Meng Ni et al. [40] used mathematical modeling to conduct a parametric analysis to determine the activation, concentration, and ohmic overpotential relationships with the cell microstructures (porosity and pore size) and operational parameters (temperature, pressure, and gas composition). Moreover, they discussed how the cell's performance could be improved by increasing the hydrogen content in the fuel stream and the operating pressure. Yang et al. [41] tested a 10 x 10 cm^2 anode-supported SOFC for working temperatures 750 ℃, 800 ℃, and 850 ℃ to obtain the I-V curves at each operating temperature. After that, a mathematical model was developed to investigate how structural and operational parameters affect the performance of cells. The result of the model shows that the anode-supported cell's performance is dominated by the activation overpotential. Despite the thin electrolyte, which makes the ohmic overpotential less significant than the activation overpotential, the ohmic overpotential is still essential. The majority of the voltage loss was caused by the ohmic overpotential and

activation overpotential. Additionally, they described the effect of structural parameters such as electrolyte thickness, electrode thickness, TPB length, and porosity on cell overpotentials and cell performance. Moreover, the effect of operation parameters such as the operating temperature and pressure on cell activation, ohmic, and concentration losses. Yahya et al. [42] used mathematical modeling not only to investigate the dependence of the ohmic, activation, and concentration overpotentials on the operating temperature, but also the effect of fuel dilution with nitrogen and water vapour on the cell's anodic activation and the effect of hydrogen molar fraction and fuel flow rate on the cell's performance.

1.4.2 Multi-dimensional modeling (2-D and 3-D)

Due to the significant advances in CFD modeling and how it provides a powerful tool to help with understanding SOFCs working principles and the complicated fluid flow and heat transfer processes that occur inside the cell, a huge number of publications have adopted CFD modeling for SFOCs.

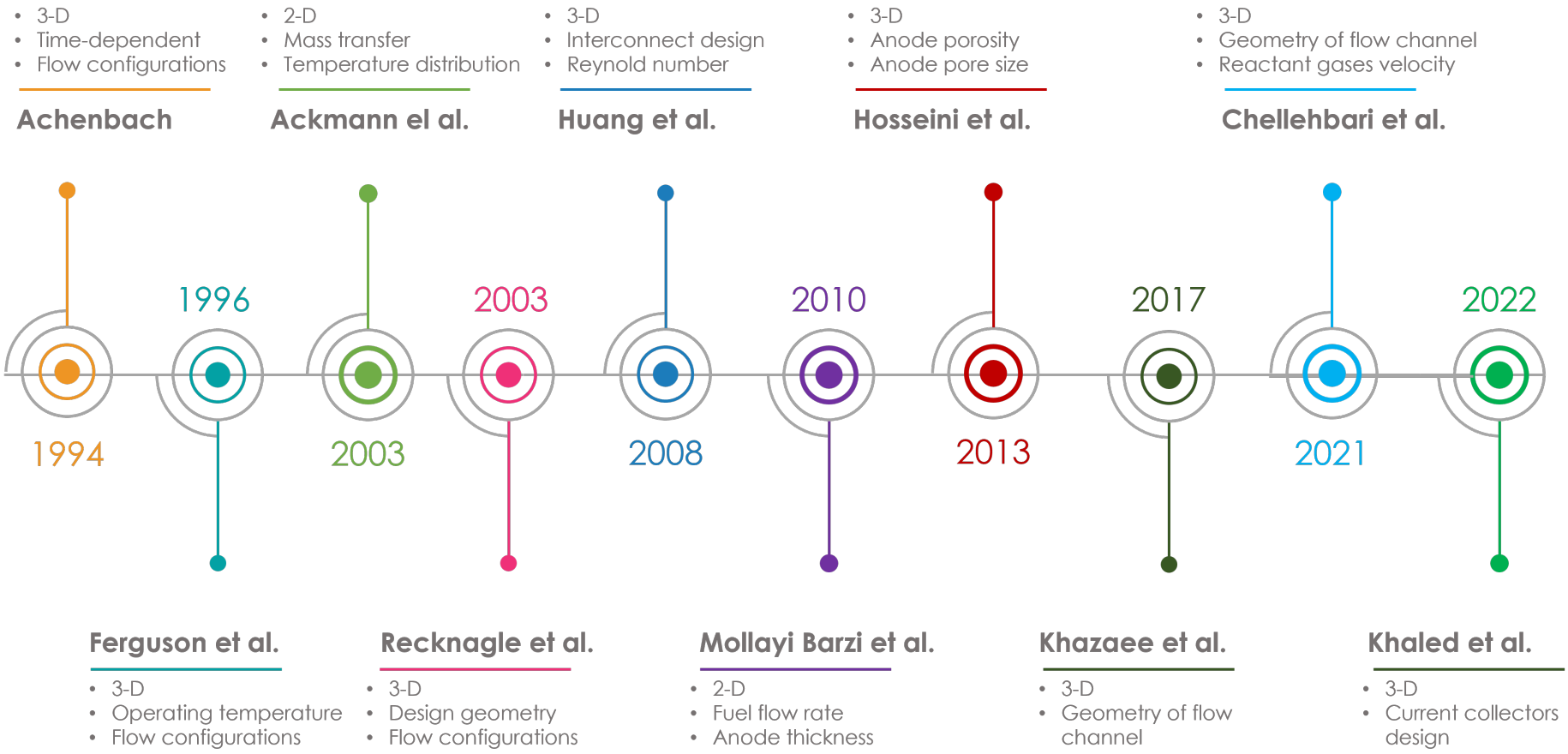

Figure 1.8: Major SOFC CFD modeling in literature, including timeline and items investigated.

Achenbach [31] developed a 3D and time-dependent SOFC stack model with internal methane-steam reforming, anode gas recycling, and conductive, convective, and radiative heat transfer. This study discussed the effect of different flow configurations such as cross-flow, co-flow, or counter-flow on the cell performance. The results show for counter-flow, the highest cell efficiency is obtained, while co-flow has the most uniform current density distribution, and cross-flow was responsible for the highest temperature gradients. Ferguson et al. [32] developed a 3D model which allows the computation of the local distributions of the electrical potential, temperature and concentration of the chemical species. The numerical findings illustrate how the potential, temperature, and current distributions behave when different electrolyte materials, cell geometry, and channel temperature are changed. Ackmann el al. [29] developed two-dimensional simulations for SOFCs using partially prereformed methane as the anode and cathode substrates. They modeled mass transfer through diffusion and the distribution of temperature in the porous structure using ANSYS FLUENT and MATLAB. Their model made it possible to figure out the temperature and concentration profiles in a SOFC's porous substrates; therefore, they assume that their model is useful for conducting sensitivity analysis of operating and structural parameters to optimise the mass transport inside the electrodes by changing the structural parameters.

Recknagle et al. [33] developed a tool for modeling a planar SOFC which combines a verified electrochemistry calculation approach with the versatility of a commercial computational fluid dynamics simulation. The main objective of this model is to predict temperature and current distribution, fuel utilisation, fuel flow and distribution at the anode and oxidant distribution at the cathode. Also, the design geometry and the flow configuration were studied, and the results show the co-flow configuration had the most uniform temperature distribution and the smallest thermal gradients, which significantly reduced the cell thermal stresses. Huang et al. [34] investigated flow homogeneity in various interconnects and how it affects a planar SOFC's cell performance. Their results of numerical analyses show that Reynolds's number has a significant impact on cell performance and Reynolds's number values that are appropriate for the anode and cathode sides have been identified in order to achieve a reasonable peak power density while maintaining an economical fuel utilisation rate and minimising temperature gradients in

the single-cell stack. Mollayi Barzi et al. [30] developed a 2-D numerical model to predict and evaluate the performance of an anode-supported SOFC button cell. The model has two main functions: firstly, it allowed to study the effect of various fuel flow rates and humidification on the button cell SOFC performance. The results show that the activation overpotential increases while increasing the inlet vapour concentration. Secondly, it allowed to study the effect of the anode thickness on the cell's performance.

Hosseini et al. [35] developed a CFD model to investigate the combined impacts of the anode diffusion layer's macro and micro structural characteristics and flow field design. The study discussed how the anode diffusion layer thickness, porosity, and pore size influence cell performance. Khazaee et al. [36] studied the effect of the interconnect, rectangular duct gas flow channels, gas diffusion electrodes, and electrolyte layer on the performance of a planar SOFC. Additionally, the paper studied various fuel cell channel geometries, from being rectangular to triangular and trapezoidal shapes, ensuring that each cell's active area and other operating conditions are the same. According to the results, the rectangular channel design performs better when compared to the trapezoidal channel design in terms of cell performance. Chellehbari et al. [37] developed a 3D CFD model for a planar SOFC; in this work, equations associated with mass, energy, and momentum transport are simultaneously solved in order to better understand electrochemical reactions. The main functions of the model were, firstly, to investigate how various fuel channel designs and the number of obstacles across them affect fuel cell performance. Secondly, investigations were conducted on the effects of operating conditions on the SOFC's electric output, including integrated transport phenomena and electrochemical reactions, inlet gas velocity in anode and cathode channels, and electrode porosity and permeability. Khaled et al. [38] introduced a novel tubular SOFC current collector design and numerically analysed its performance using CFD simulation. The flow channel in the new current collector design has a trapezoidal structure. The impacts of several channels, including four, eight, and twelve, on cell performance were investigated and compared. The results show the current collector design with twelve channels has the best cell performance among the other designs; however, it has a higher hydrogen concentration at the outlet compared to the designs with four and eight channels.

1.5 What this thesis offers

This thesis aims to study and analyse tubular and planar anode-support solid oxide fuel cells. The thesis not only investigates the effect of various operating and structural parameters on the SOFCs performance but also their effect on cells temperature profile and thermal gradients, which have a significant impact on SOFCs lifetime. To achieve that, this thesis depends not only on CFD modeling but also building an experimental setup to validate the tubular and planar SOFCs models and provide a limited range of experimental analysis. The main outcomes from this thesis are listed as follows:

- Experimental analysis:
  - Building the experimental setup and design of experiments: An experimental setup was designed and built under Dr. Sajad Vafaeenezhad supervision. These include fuel and oxidant supply systems, temperature control systems, and data gathering systems. The design of experiments was performed to develop the test scheme required for models validation and SOFC experimental studies.
  - Measuring cell temperature distribution: An innovative way was designed to install thermocouples across the tubular anode-support SOFC to provide a better understanding of the cell temperature profile at different operating conditions. The temperature measurements were then used for thermal management analysis of the cell.
- Zero-dimensional modeling (0D):
  - Modeling SOFC at various operating temperatures: A computationally-efficient 0D model was designed to simulate the effect of various operating temperatures on tubular anode-support SOFC performance in real-time.
  - Predicating the cell overpotentials: Activation, ohmic, and concentration cell overpotentials are predicted based on the 0D model, and their relationship with operating temperatures is studied.

- CFD modeling (3D):
  - Design and validation of the CFD model: A CFD model is designed and experimentally validated for both tubular and planar SOFCs.
  - Modeling the fluid flow and heat transfer: The developed CFD model can describe the complex flow distribution and heat transfer processes taking place within the SOFC system. To this end, the model takes into account the processes of heat exchange, species transportation inside the electrodes, and reactant gas flow.
  - Modeling various operating conditions: Examined how the SOFC system performs under various operating conditions, such as varying operating temperatures, fuel compositions, and geometrical arrangements.
  - Optimizing the design and operation of the SOFCs: This thesis uses CFD analysis to enhance the SOFC system's operation and design. This includes an investigation into design aspects including the cell's macro- and micro-structure and thermal management.

1.6 Thesis structure

This thesis is organized in seven chapters as shown in 1.9. Chapter 2 includes the experimental setup and test scheme for tubular and planar cells to gather the experimental data used for models validation. Chapter 3 discusses the SOFCs' electrochemical reactions and governing equations. Then chapter 4 shows the validation and results of the tubular cell 0D model and 3D CFD model. While chapter 5 shows the validation and results of the planar cell 3D CFD model. The parametric analysis for tubular and planar structural and operating parameters is discussed in chapter 6. Finally, conclusions along with recommendations for future work are presented in chapter 7.

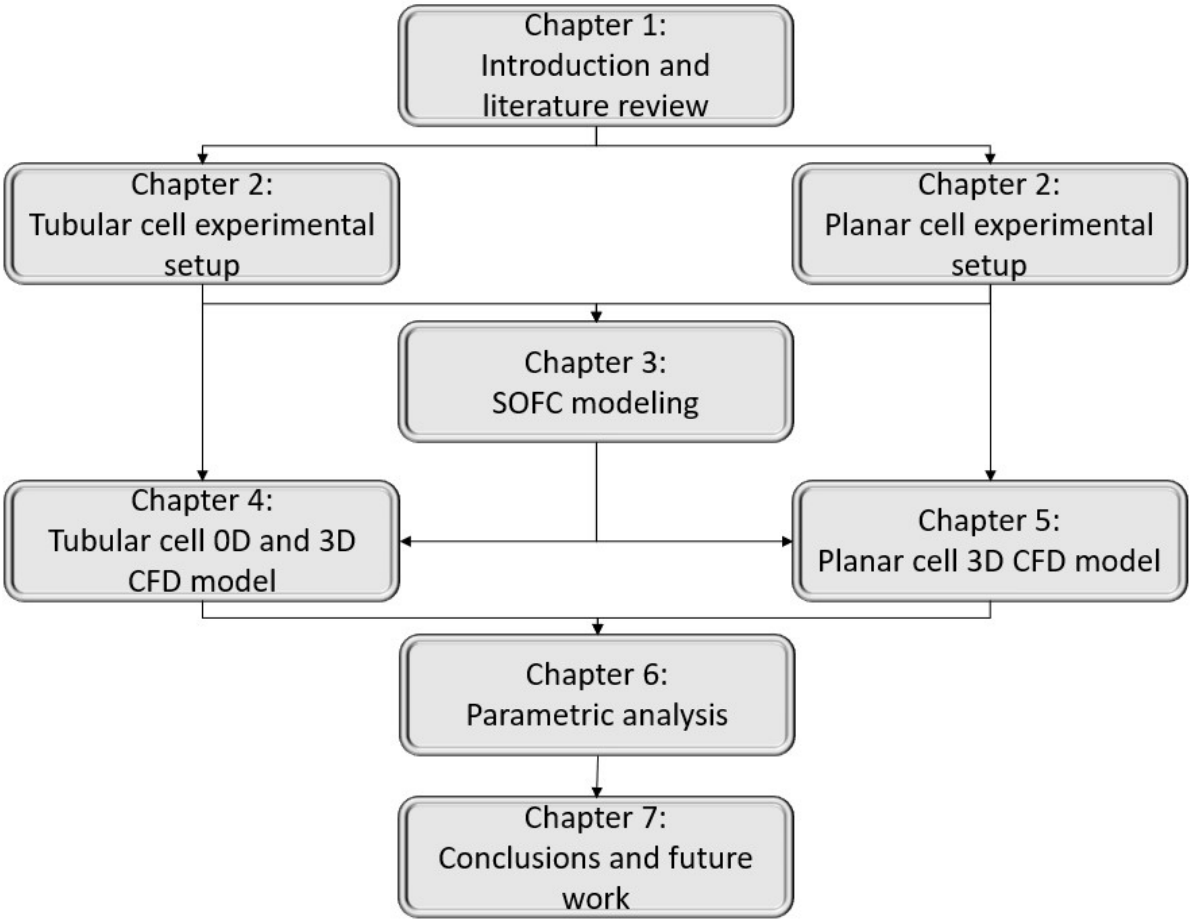

Figure 1.9: Schematic of the thesis organization

Chapter 2

Experimental set-up

In this chapter, two experimental setups are developed to study the performance of tubular and planar cells. The two experiments are in charge of: first, regulating the operating temperature of the cell to assess the performance of the cell at various operating temperatures. Secondly, controlling the flow rates of reactant gases (hydrogen, nitrogen, and air). Lastly, measuring the open circuit voltage (OCV), current, voltage, and impedance by using electrochemical impedance spectroscopy (EIS) on a Metrohm Autolab potentiostat with a 10 A booster.

2.1 Planar experimental setup

A schematic of the planar cells test setup is shown in Figure 2.1. The isolation valves (1) are used to isolate the test setup and close the inlet gases pathways. The flow rate of the incoming gases is regulated by the flow control valves (2). The flow and pressure measuring devices (3) are used to measure the flow rates and pressures of the incoming gases. The dry hydrogen and nitrogen mixture is hydrated using the humidifier (4). The gases preheaters (5) are used to increase the inlet temperature of air, nitrogen, and hydrogen by the temperature controller (6). The furnace (14) is used to control the cell operating temperature, which can be monitored and controlled by the temperature controller (6) and the cell thermocouple (7). Furthermore, the furnace height can be adjusted based on the number of cells inside the SOFC planar stack by using the fed motor (10) and the furnace height adjustment mechanism (11). The air compressor (8) and the piston cylinder (9) are used to provide external compression to the planar stack (15). The unreacted hydrogen and nitrogen mixture exhaust is from vent

(13) and the air exhaust is from vent (12). Figure 2.2 shows how the actual testing setup components look like.

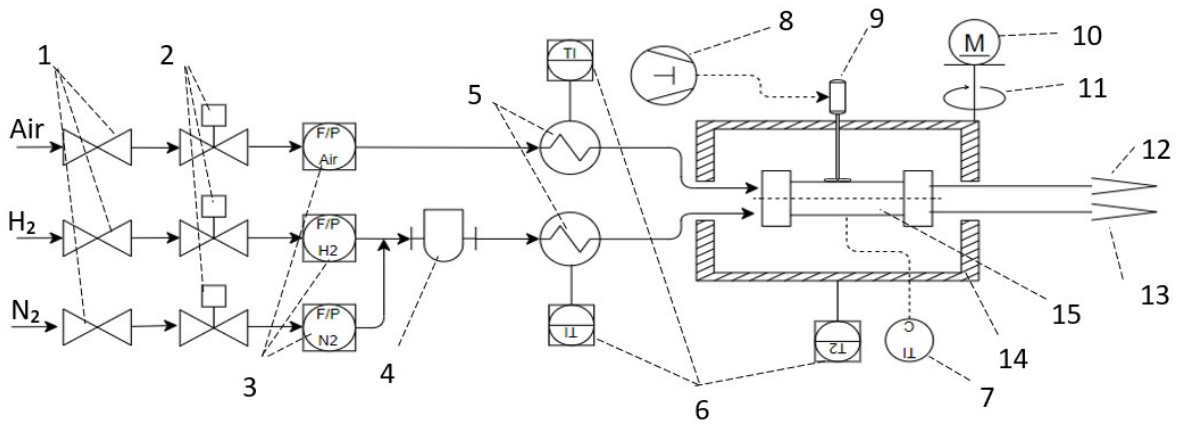

1- Isolation Valve
2- Flow Control Valve
3- Flow and Pressure Measuring Device
4- Humidifier
5- Gases Preheater
6- Temperature Controller
7- Thermocouples
8- Compressor
9- Pneumatic Cylinder
10- Fed Motor
11- Furnace Height adjust Mechanism
12- Air Outlet
13- H_2 Outlet
14- Furnace
15- Planar Cell

Figure 2.1: Schematic for the planar test set-up

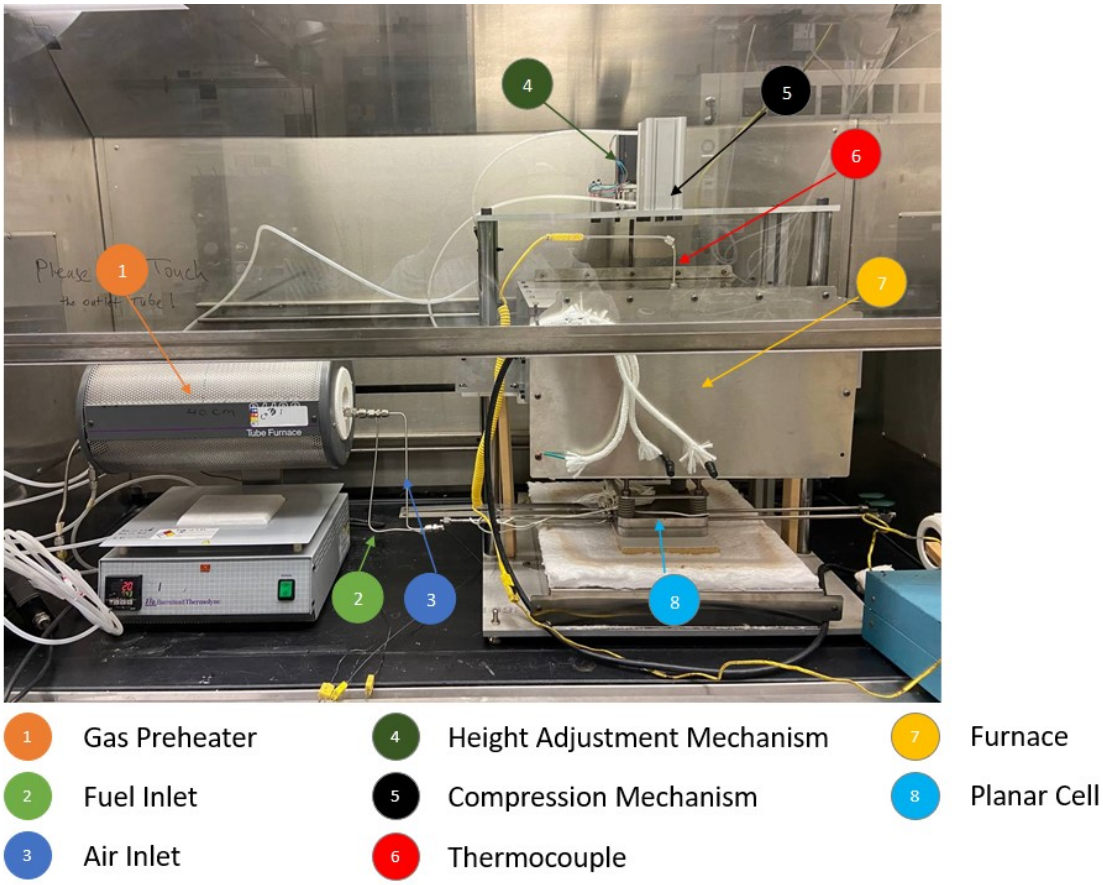

Figure 2.2: Planar cells stack test set-up components

Table 2.1: Specification of tubular SOFC test setup components.

Instrument	**Specifications**	**Range / Accuracy**
Isolation valves	Brand/Model: Swagelok / Stainless Steel 1-Piece 40G Series Ball Valve, 0.2 Cv, 1/8 in. Swagelok Tube Fitting	Working pressure range: up to 2500 psig at 37°C Working temperature range: 10 to 65°C
Thermocouples	Brand/Model: OMEGA / K-type-CHAL-010-BW-24 Butt-Welded Unsheathed Fine	Measuring range: 0 to 1250°C Accuracy: 2.2°C or 0.75%
Mass Flow Meters and Controllers	Brand/Model: ALICAT / MC-500SCCM	Mass flow measuring range: 0 to 500 SCCM Pressure measuring range: 0 to 160 psia Accuracy: ±0.6%
Electrochemical impedance spectroscopy (EIS)	Brand/Model: Metrohm PGSTAT30 Potentiostat Galvanostat Electrochemical System combined with FRA32M	Potential range: +/- 10 V Potential accuracy: ±0.2% Current range: +/- 10 A Current accuracy: ±0.2%
Temperature Controller	Brand/Model: OMEGA / CN7400 Series temperature/process limit controller	Temperature range: -129 to 1371°C Accuracy: ±0.25%
Gases preheater	Brand/Model: BARNSTEAD THERMOLYNE CORPORATION / Thermolyne F21100 Tube Furnace	Temperature range: 100 to 1200°C Electrical Ratings 1350 Watts Accuracy: ±0.75%
Box furnace	Brand/Model: Sentro Tech / ST-1600C-101012 High Temperature Box Furnace	Temperature range: 100 to 1600°C Electrical Ratings 10 Kw Accuracy: ±1%
Compressor	Brand/Model: Mastercraft / AS-18	Working pressure range: 0 to 58 psig Air Flow: 0.7 CFM at 40 psig

2.2 Planar cell experimental procedures

The planar SOFC stack contains a single cell from Elcogen; the cell size is 9 cm x 9 cm and has an effective electrode area of 81 cm^2. The cell anode function layer and support layer are made from Ni-YSZ, while the electrolyte material is YSZ and the cathode material is Lanthanum Strontium Cobaltite (LSC). Table 2.2 shows the Elcogen planar cell specifications and figure 2.3 shows the Elcogen cell structure and its SEM photo. The stack consists of end plates, insulation plates, collector plates, single cell, metal spacers, nickel mesh, and corfer mesh, which are assembled together by means of compression forces. The assembly procedures are discussed in detail in the Appendix A.

Table 2.2: Elcogen planar cell specifications.

specifications	**Value**
Anode support layer composition	NiO/YSZ
Anode functional layer composition	NiO/YSZ
Electrolyte layer composition	YSZ
Cathode layer composition	LSC
Suggested operating temperature	600–800°C
Standard size (cell)	9 cm x 9 cm
Maximum working pressure	50 mbar(g)
Suggested External compression	300-600 g/cm^2

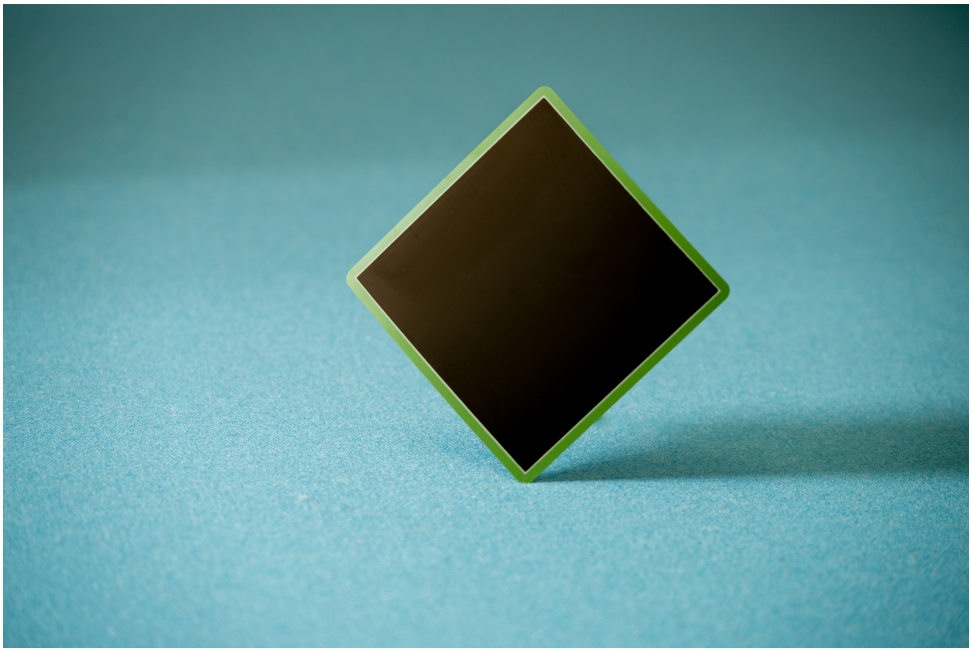

(a)

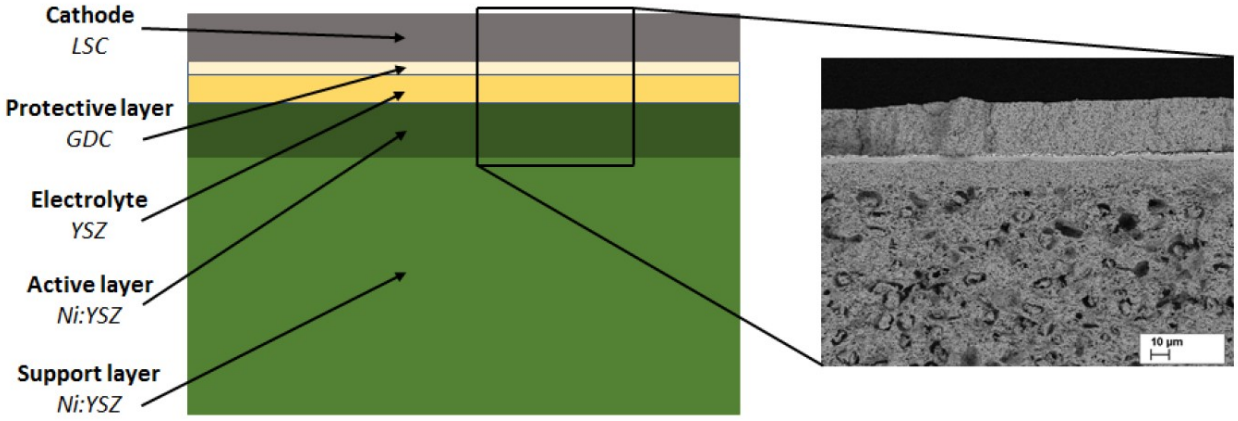

(b)

Figure 2.3: (a) Elcogen planar cell photo and (b) schematic structure of Elcogen's cells (left) with SEM photo (right).

Firstly, the cell is heated to 300 °C, which is the needed temperature for the Mica gaskets to seal properly, and an external compression force is applied by the pneumatic cylinder and left at this temperature for 3 hours. This step is important to stabilize the cell's internal strengths, enhance sealing, and improve contact with current collectors. Then the cell reduction process takes place: 25 SCCM of hydrogen is mixed with 375 SCCM of nitrogen and supplied to the anode side, while the cathode side is supplied with air and left for 2 hours to reduce the nickel oxide. After that, the furnace's temperature is increased to 650 °C with a ramp of 1 °C/min.

Finally, the hydrogen content is gradually increased until it reaches 100% and the open circuit voltage (OCV) stabilizes. If the OCV data does not show a fluctuation larger than +/- 5mV/3h, that means the system is in a steady state and the data acquisition process can start.

2.3 Planar experimental test scheme:

The planar cell experimental test scheme has 10 different operating conditions. The experimentally studied operating temperatures were 600 °C and 650 °C. The inlet gases flow rates and fuel composition were studied as well. The hydrogen flow rate was changed from 200 up to 400 SCCM, the nitrogen flow rate was changed by 0, 100, and 200 SCCM, and the air flow rate was changed from 300 up to 500 SCCM. Table 2.3 The table shows the operating temperatures and inlet gases flow rates used in the planar cell experimental test scheme.

Table 2.3: Planar SOFC test scheme.

Test	**Temperature °C**	H_2 **flow rate (SCCM)**	N_2 **flow rate (SCCM)**	**Air flow rate (SCCM)**
1	600	200	200	400
2	300	100	30	400
3	600	400	0	300
4	600	400	0	400
5	600	400	0	500
6	650	200	200	400
7	650	300	100	400
8	650	400	0	300
9	650	400	0	400
10	650	400	0	500

2.4 Tubular experimental setup

A schematic of the tubular cells test setup is shown in Figure 2.4. As the planar cell setup, the isolation valves (1) are used to isolate the test setup and close the inlet gases pathways. The flow rate of the incoming gases is regulated by the flow control valves (2). The flow and pressure measuring devices (3) are used to measure the flow rates and pressures of the incoming gases. The dry hydrogen and nitrogen mixture is hydrated using the humidifier (4) (3 vol.% H_2O). The gases preheaters (5) are used to increase the inlet temperature of air, nitrogen, and hydrogen by the temperature controller (6). The tubular cell (7) is placed inside a tubular furnace (8) to control the cell's operating temperature. There are three thermocouples (9) attached to the cell to measure the temperature distribution along the cell, which is mainly used to validate the cell temperature distribution. The unreacted hydrogen and nitrogen mixture and air exhaust are both from vent (10). Table 2.4 shows the specifications of the main experimental components used in the tubular cell setup:

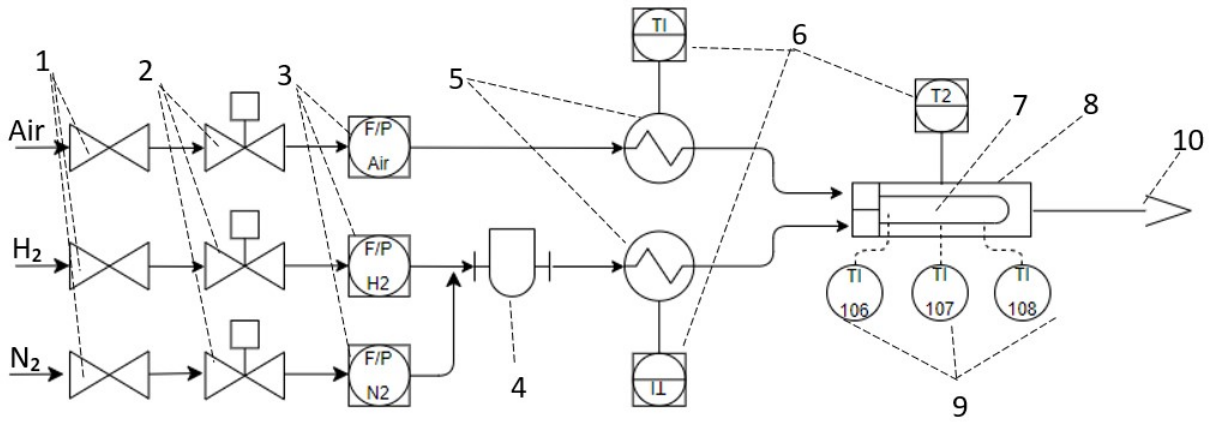

1- Isolation Valve
2- Flow Control Valve
3- Flow and Pressure Measuring Device
4- Humidifier
5- Gases Preheater
6- Temperature Controller
7- Tubular Cell
8- Tubular Furnace
9- Thermocouples
10- Cell Exhaust Vent

Figure 2.4: Schematic for the tubular test set-up

Table 2.4: Specification of tubular SOFC test setup components.

Instrument	**Specifications**	**Range / Accuracy**
Isolation valves	Brand/Model: Swagelok / Stainless Steel 1-Piece 40G Series Ball Valve, 0.2 Cv, 1/8 in. Swagelok Tube Fitting	Working pressure range: up to 2500 psig at 37°C Working temperature range: 10 to 65°C
Thermocouples	Brand/Model: OMEGA / K-type-CHAL-010-BW-24 Butt-Welded Unsheathed Fine	Measuring range: 0 to 1250°C Accuracy: 2.2°C or 0.75%
Mass Flow Meters and Controllers	Brand/Model: ALICAT / MC-500SCCM	Mass flow measuring range: 0 to 500 SCCM Pressure measuring range: 0 to 160 psia Accuracy: ±0.6%
Electrochemical impedance spectroscopy (EIS)	Brand/Model: Metrohm PGSTAT30 Potentiostat Galvanostat Electrochemical System combined with FRA32M	Potential range: +/- 10 V Potential accuracy: ±0.2% Current range: +/- 10 A Current accuracy: ±0.2%
Temperature Controller	Brand/Model: OMEGA / CN7400 Series temperature/process limit controller	Temperature range: -129 to 1371°C Accuracy: ±0.25%
Gases preheater	Brand/Model: BARNSTEAD THERMOLYNE CORPORATION / Thermolyne F21100 Tube Furnace	Temperature range: 100 to 1200°C Electrical Ratings 1350 Watts Accuracy: ±0.75%
Tubular furnace	Brand/Model: BARNSTEAD THERMOLYNE CORPORATION / Thermolyne F79300 Tube Furnace	Temperature range: 100 to 1200°C Electrical Ratings 2880 Watts Accuracy: ±0.75%

Figure 2.5 illustrates the location of the three K-type thermocouples. The thermocouple (A) is placed at the fuel exhaust stream to measure the temperature of the fuel outlet, while the thermocouple (B) is placed on top of the active area to measure the cathode temperature. Lastly, the thermocouple (C) is placed at the distance between the active area and the cell's close end.

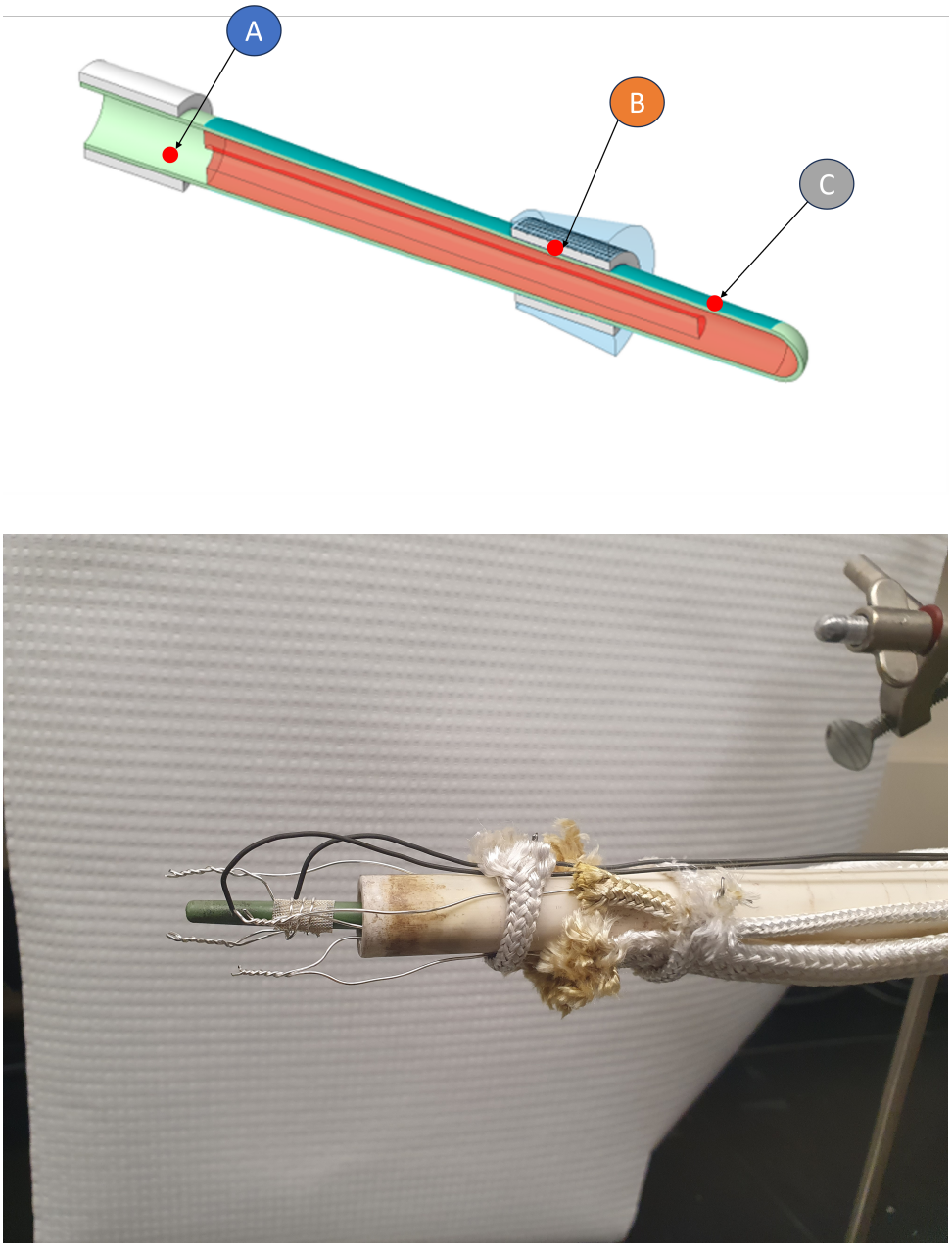

Figure 2.5: The thermocouples placement for the tubular cell test setup.

2.5 Tubular experimental procedures:

Ceramabond 552 (Aremco) cement was used to connect the tubular cell to the mullite tube. The cell was put in a tubular furnace's hot zone and the three aforementioned thermocouples were placed to measure the cell temperature at certain locations. Then a mixture of nitrogen and humidified hydrogen was used to reduce the anode for a period of 24 hours with the following flow rates 43 and 7 standard cubic centimeters per minute (SCCM), respectively. After that, for a period of 1 hour, the gas composition was gradually changed to 50 SCCM of hydrogen and 0 SCCM of nitrogen. The air was supplied to the cathode side with 100 SCCM.

2.6 Tubular experimental test scheme:

The experimental test scheme of the tubular cell contains 36 different operating conditions. The experiment studied the tubular cell performance under mainly three different operating conditions. Additionally, it studied the effect of changing the fuel composition, fuel flow rate, and air flow rate on the cell's performance. Various combinations of hydrogen, nitrogen, and air flow rates were selected for this study. The hydrogen flow rate was altered from 20 upto 150 SCCM, the nitrogen flow rate was altered from 0 upto 60, and the air flow rate was altered from 50 upto 300 SCCM. Table 2.5 represents the temperature and flow rate values for each test of the test scheme.

Table 2.5: Tubular SOFC test scheme.

Test	**Temperature °C**	H_2 **flow rate (SCCM)**	N_2 **flow rate (SCCM)**	**Air flow rate (SCCM)**
1	650	90	60	300
2	650	120	30	150
3	650	120	30	300
4	650	150	0	150
5	650	150	0	300
6	650	90	60	150
7	650	20	30	50
8	650	20	30	100
9	650	35	15	50
10	650	35	15	100
11	650	50	0	50
12	650	50	0	100
13	700	90	60	300
14	700	120	30	150
15	700	120	30	300
16	700	150	0	150
17	700	150	0	300
18	700	90	60	150
19	700	20	30	50
20	700	20	30	100

Test	**Temperature °C**	**H_2 flow rate (SCCM)**	**N_2 flow rate (SCCM)**	**Air flow rate (SCCM)**
21	700	35	15	50
22	700	35	15	100
23	700	50	0	50
24	700	50	0	100
25	750	90	60	300
26	750	120	30	150
27	750	120	30	300
28	750	150	0	150
29	750	150	0	300
30	750	90	60	150
31	750	20	30	50
32	750	20	30	100
33	750	35	15	50
34	750	35	15	100
35	750	50	0	50
36	750	50	0	100

Chapter 3

SOFC modeling

In this thesis, both zero-dimensional and three-dimensional CFD models are developed for SOFC simulations. The 0-D model provides an estimation of the cell performance and the cell overpotential. This model can be used for SOFC control and real-time monitoring. While a CFD model is developed to provide in-depth analysis of SOFCs for design and diagnostic purposes. This chapter focuses on describing the SOFC electrochemical reactions and governing equations, while chapter four will provide experimental validation of the models.

3.1 Zero-dimensional model (0-D)

Mathematical modeling provides a platform to estimate the performance of SOFCs. The zero-dimensional model for SOFCs incorporates various physical and electrochemical processes occurring within the cell. The main advantage of the 0-D model over the CFD model is that it requires less computational time, so it can be used for control aspects and online performance optimization. On the other hand, although CFD modeling requires more computational time, it provides a more effective tool for understanding and evaluating the electrochemical processes, fluid flow, and heat transfer that take place inside the fuel cell. This provides a better way for heat and mass transfer through the cell, leading to enhancing the fuel cell's design.

The results of a personal prior publication are presented in this thesis; the paper title is "Experimental and thermodynamic analyses of a novel anode-supported solid oxide fuel cell". The paper adopted the 0-D mathematical model approach to study a tubular SOFC [43]. One of the aspects that this study focuses on is the effect of the cell operating temperature

on the SOFC performance and the relationship between the operating temperature and the cell overpotenial: activation overpotenial, ohmic overpotenial, and concentration overpotenial. Table 3.1 shows the 0-D model input parameters:

Table 3.1: SOFC model input parameters.

Parameter	**Value**	**Unit**
Active surface area	2	cm^2
Air flow rate	150	SCCM
Ambient temperature	25	°C
Conductivity of anode	$\frac{9.5*10^7}{T}exp(-\frac{1150}{T})$	Ω m
Conductivity of cathode	$\frac{4.2*10^7}{T}exp(-\frac{1200}{T})$	Ω m
Conductivity of electrolyte	$33.4*10^3exp(-\frac{10300}{T})$	Ω m
Transfer coefficient	0.5	–
Hydrogen flow rate	50	SCCM
Faraday's constant	96485	C mol^{-1}
SOFC operating pressure	1.01	bara
Thickness of the anode	388	μm
Thickness of the cathode	7.5	μm
Thickness of the electrolyte	6.5	μm

- Actual voltage:

  The performance of the fuel cell is characterized by the current voltage (I-V) diagram, which represents the fuel cell's outlet voltage with respect to different current densities. Theoretically, the voltage of a fuel cell is always lower than the ideal voltage calculated using thermodynamic laws. In addition, lower voltage values will be generated from the cell at higher current densities, restricting the overall power produced in reality [41], which is stated by the Nernst equation [13]:

$$\phi_{ideal} = \phi^\circ + \frac{RT}{2F}\ ln\left(\frac{p_{H_2}p_{O_2}^{1/2}}{p_{H_2O}}\right) \tag{3.1}$$

Where P_i is the partial pressure of component i, R is the universal gas constant, and T is the absolute operating temperature. While ϕ° is the open-circuit cell voltage. The open-circuit voltage or (OCV) is the highest voltage a fuel cell is capable of producing when there is no current drawn from the cell [13]:

$$\phi^\circ = -\frac{\Delta G^o}{nF} \tag{3.2}$$

ΔG^o is the Gibbs free energy at ambient pressure, n shows the number of electrons exchanged in the reaction, and F is Faraday's constant.

The actual output voltage of the fuel cell can be expressed by subtracting the voltage calculated based on thermodynamic laws from the voltage drop because of the different cell polarizations. The SOFC's output voltage can be calculated as [13]:

$$\phi_{cell} = \phi_{ideal} - \eta_{act} - \eta_{ohm} - \eta_{con} \tag{3.3}$$

Where η_{act} is the activation losses, η_{ohm} is the ohmic losses, and η_{con} is the concentration losses.

- Cell overpotential:

The fuel cell's performance and efficiency are affected by various cell overpotentials. The physical and chemical processes that take place inside the fuel cell are the cause of these losses. The fuel cell polarization losses are proportional to the electrical current drawn from the cell. There are three main forms of polarisation losses:

– Activation Losses:

Activation losses is the overpotential needed to overcome the activation energy to start the chemical reaction. The activation losses can be reduced by increasing the surface area of the electrodes, increasing the operating temperature, or by using catalysts to lower the activation energy of the reaction. The Butler–Volmer equation is used to calculate the activation polarization at each electrode–electrolyte interface [44]:

$$i = i_{0eff}\left[e^{\frac{\alpha_a \ n \ \eta_{act,a} \ F}{R \ T}} - e^{\frac{\alpha_c \ n \ \eta_{act,c} \ F}{R \ T}}\right] \tag{3.4}$$

where i_{0eff} is the effective exchange current density, the Butler-Volmer equation can be linearized, and from the slope of the polarization curve, i_{0eff} can be estimated. α_a is the oxidation transfer coefficient at the anode side and α_c is the reduction transfer coefficient at the cathode side.

Because the hyperbolic sine function behaves similarly to the profile of the corresponding ΔV_{act} against current density curve, a hyperbolic sine function is used as an approximation to the Butler–Volmer equation. Therefore, the activation overpotential can be determined explicitly if α_a and α_c are assumed to be equal:

$$\Delta\eta_{act} \cong \frac{RT}{\alpha F}\sinh^{-1}(\frac{i}{2i_0}) \tag{3.5}$$

– Ohmic Losses:

Ohmic losses happen as a result of the electrodes' and electrolyte's electrical resistance to the electrical current flow. Leading to the cell output voltage drop. These losses can be reduced by using materials with a lower resistance, such as highly conductive metals, or by increasing the thickness of the electrodes to reduce resistance. The cell electrolyte is responsible for the largest portion of the ohmic losses due to its low electrical conductivity. The electrolyte and the electrodes electrical conductivity are significantly influenced by the operating temperature; that is the main reason for the required SOFCs' high operating temperature to achieve high

electrical conductivity for the electrolyte and the electrodes, leading to lower ohmic losses.

Ohmic losses are directly proportional to current density and are affected by cell geometry, the selection of the materials, and the operation temperature. It can be described by using Ohm's law [13]:

$$\eta_{ohm} = iR_{ohmic} \tag{3.6}$$

where i is the current density, and R_{ohmic} is the total internal resistance of the cell:

$$R_{ohmic} = \frac{\delta_{anode}}{\sigma_{anode}} + \frac{\delta_{elec}}{\sigma_{elec}} + \frac{\delta_{cathode}}{\sigma_{cathode}} \tag{3.7}$$

where δ_{anode}, δ_{elec}, and $\delta_{cathode}$ are the thickness of the anode, the electrolyte and the cathode, respectively. σ_{anode}, σ_{elec}, and $\sigma_{cathode}$ are the conductivity of the anode, the electrolyte and the cathode, respectively.

– Concentration Losses:

Concentration losses occur due to mass transfer limitation inside the fuel cell when reactants or products gases cannot diffuse efficiently through the electrodes layer. As a result, it's possible to have a concentration gradient within the cell, which would slow the pace of reaction and lower the output voltage. These losses can be reduced by increasing the flow rate of the reactants or by improving the diffusion properties of the electrodes and electrolyte. The mass transport limitation causing the concentration Losses is expressed by [45]:

$$\eta_{con} = c\ ln(\frac{i_L}{i_L - i}) \tag{3.8}$$

Where, c is the concentration loss constant. The constant c is expressed as:

$$c = \frac{RT}{nF} \tag{3.9}$$

And i_L is the highest current that can be pulled from the cell when the concentrations of reactants at the catalyst active sites decrease to zero.

3.2 CFD model (3-D)

The model described in this thesis uses the ANSYS FLUENT SOFC module. Using commercial software, the set of partial differential equations is numerically solved to model SOFC electrochemical reactions, air and fuel flow, as well as heat, mass, and current transfer.

The computational fluid dynamics (CFD) modeling of solid oxide fuel cells is based on the modeling of the following phenomena [46]:

- Current and potential field transport: represents the transfer of ions and electrons and the calculation of the cell produced current and potential.
- Electrochemical Reactions: represents the release of ions and electrons from the electrochemical reactions.
- Heat Transfer: represents the conduction and convective heat transfer by solving the energy conservation equation.
- Mass Transfer: represents the mass conservation equation and the species conservation equation.
- Fluid Flow: represents the conservation of momentum to model the flow of fuel and air in the flow channels.

A set of assumptions are considered to model the aforementioned phenomena:

- Laminar and incompressible flow

  The flow in SOFCs typically involves low velocities.

- Steady state operation

  All the experimental data was collected at steady state condition and all the models do not include transient simulation.

- Constant thermal expansions for all components

  The high thermal compatibility of the anode, electrolyte, and cathode materials.

- Negligible heat loss

  Because all the used furnaces are properly insulated.

- Negligible radiation heat transfer

  The radiation heat transfer has a very minor effect, and it could be ignored for simplification.

3.3 CFD model equations

The CFD model contains a set of governing equations to capture fluid dynamics, thermodynamics, species transfer, heat transfer, and electrochemical reaction equations.

3.3.1 Electrochemical reactions

The overall reaction of the SOFC is the reaction between hydrogen and oxygen to produce water vapour. Hydrogen is fed to the anode side where the hydrogen oxidation reaction takes place while air is fed to the cathode where the oxygen reduction reaction takes place. The oxygen ions produced from the oxygen reduction reaction at the cathode side migrate through the electrolyte to the anode side, where they react with the hydrogen molecule to produce water vapour and release electrons that produce electricity when they are transported through an external circuit.

Species production and consumption rates are governed by [47]:

$$S = -\frac{ai}{nF} \tag{3.10}$$

$$S_m = S_{H_2} + S_{H_2O} + S_{O_2} \tag{3.11}$$

Where S is the source or sink of the species (molar flux), a is the stoichiometric coefficient, i is the current density, n is the number of electrons per mole of fuel, and F is the Faraday constant. S_m is the source terms, which are applicable at the interface electrode-electrolyte.

Overall reaction:

$$H_2 + 1/2\ O_2 \rightarrow H_2O \tag{3.12}$$

Hydrogen oxidation reaction:

$$H_2 + O^{2-} \rightarrow H_2O + 2e^- \tag{3.13}$$

$$S_{H_2} = -\frac{i}{2F} \tag{3.14}$$

$$S_O^{2-} = -\frac{i}{2F} \tag{3.15}$$

$$S_{H_2O} = -\frac{-(1)(i)}{2F} = \frac{i}{2F} \tag{3.16}$$

Oxygen reduction reaction:

$$1/2\ O_2 + 2e^- \rightarrow O^{2-} \tag{3.17}$$

$$S_{O_2} = -\frac{-(\frac{1}{2})(-i)}{2F} = -\frac{i}{4F} \tag{3.18}$$

$$S_O^{2-} = -\frac{i}{2F} \tag{3.19}$$

3.3.2 Conservation equations

The conservation of mass, momentum, charge, thermal energy, and species are the governing equations to represent the fundamental processes in fuel cells. These transport equations are combined with electrochemical processes using source-sink terms.

- Mass conservation:

  The conservation of mass equation of SOFC describes how the mass is conserved in the cell and provides a solution for the fuel and air channels and corresponding electrodes:

  $$\nabla.(\varepsilon\rho\vec{v}) = S_m \tag{3.20}$$

  Where, ρ is the gas density, $\vec{v}$ is the gas velocity, and ε is the material porosity. While ∇ is a vector differential operator, and it is used with the dot product (.) to give a scalar field called the divergence of the velocity field [48].

- Momentum conservation:

  The conservation of momentum equation of SOFC describes the relationship between the flow rate of the fuel and oxidant gases to the pressure drop.

  $$\nabla.(\varepsilon\rho\vec{v}\vec{v}) = -\nabla p + \nabla.(\varepsilon\mu\vec{v}) + \frac{\mu\varepsilon^2}{k_g}\vec{v} \tag{3.21}$$

  Where, p is the pressure, μ is the gas viscosity, and k_g is the gas phase permeability. Because of the low Reynolds number, the Darcy term is used within the porous electrodes [49].

- Species conservation:

  Equation 3.22 represents the species transfer within the gas phase inside SOFC.

  $$\nabla.\left(-\rho y_i \sum_{j\neq i}^{n} D_{eff,ij}\nabla x_j + \rho\vec{v}y_i\right) = S_i \tag{3.22}$$

  Where, y_i is the species mass fraction, D_{eff} is the effective diffusivity coefficient between species i and j, x_j is the species mole fraction, and S_i is the species source term.

The microscopic and tortuous pores of the composite allow for diffusion because the solid porous electrodes themselves are impermeable. The diffusion generally occurs over a greater distance than it would in a homogenous material because the pores are not straight. Diffusion occurs across a smaller cross sectional area than is possible in a homogeneous material because the solid is impermeable. The definition of the effective diffusion coefficient (D_{eff}) includes the impacts of longer pores and smaller areas [50].

$$D_{ij,eff} = \frac{\varepsilon}{\tau} D_{ij} \tag{3.23}$$

Where, D_{ij} is the diffusion coefficient in the bulk fluid, ε is the porosity and τ is the tortuosity.

- Energy conservation:

  The energy equation describes the heat transfer through the SOFC and the production of electricity due to the electrochemical reaction. The energy equation for an SOFC can be expressed as follows [51]:

$$\nabla.(\varepsilon \rho c_p \vec{v} T) = \nabla.(k_{eff} \nabla T) + S_h \tag{3.24}$$

  Where, c_p is the specific heat capacity, K_{eff} is the coefficient of thermal conductivity, and S_h is the volumetric source or sink of energy.

  Ohmic heating is taken into consideration in the energy equation as a source term for all electrically conducting zones, such as electrodes, current collectors, and interconnects.

$$S_h = i^2 R_{ohmic} \tag{3.25}$$

  Where, R_{ohmic} is the ohmic resistance.

- Charge conservation:

  Based on the conservation of charge, the potential field is calculated throughout the conductive regions.

$$\nabla.i = 0 \tag{3.26}$$

$$i = -\sigma\nabla\phi \tag{3.27}$$

  Where, σ is the electrical conductivity and ϕ is the electrical potential. From the two equations 3.26 and 3.27 the charge conservation in SOFC is governed by the electric field is the Laplace equation [51]:

$$\nabla.(\sigma\nabla\phi) = 0 \tag{3.28}$$

3.3.3 Cell potential

When there is no electrical load and hydrogen flow, the oxygen electrochemical reduction reaction takes place at the triple phase boundary at the cathode electrode. The oxygen molecules react with electrons and produce oxygen ions based on the following reaction:

$$1/2\ O_{2,cathode} + 2e^- \Leftrightarrow O^{2-}$$

At the triple phase boundary at the anode electrode, the oxygen electrochemical oxidation reaction takes place:

$$O^{2-} \Leftrightarrow 1/2\ O_{2,anode} + 2e^-$$

The cell's hydrogen oxidation reaction is altered when the anode electrode consumes hydrogen:

$$H_2 + O^{2-} \Leftrightarrow H_2O + 2e^-$$

The cell ideal voltage becomes:

$$\phi_{ideal} = \phi^{\circ} + \frac{RT}{2F}\ ln\left(\frac{p_{H_2} p_{O_2}^{1/2}}{p_{H_2O}}\right) \tag{3.29}$$

Where, ϕ° is the open-circuit cell voltage (OCV) which is the highest voltage a fuel cell is capable of producing when there is no current drawn from the cell.

The actual OCV depends on the electrodes' temperature and gas composition. However, the cell's actual voltage is lower than the OCV because of the cell's polarisation losses which discussed earlier in the zero-dimensional section. Equation 3.30 determines the actual cell voltage:

$$\phi_{cell} = \phi_{ideal} - \eta_{act} - \eta_{ohm} - \eta_{con} \tag{3.30}$$

Where, η_{act} is the activation losses, η_{ohm} is the ohmic losses, and η_{con} is the concentration losses.

3.3.4 Heat generation in the cell

The ohmic heating contributes to some of the heat generation, however there is additional heat generated or lost as the result of electrochemical reactions and the cell's overpotentials. The enthalpy flux of all species is used to calculate the total energy balance at the electrolyte interface. The total energy balance is the balance between the heat generated due to the chemical energy entering the system and the work done by the system, which is the power produced by the cell. The heat loss is ignored in the following equation based on the highly insulated used furnaces.

$$\dot{Q} = \dot{m}_{H_2}\ h_{H_2} + \dot{m}_{O_2}\ h_{O_2} - \dot{m}_{H_2O}\ h_{H_2O} - I\Delta V \tag{3.31}$$

Where, $\dot{Q}$ is the heat generation, h is the enthalpy of species, and I is the current.

Developing a CFD model for SOFCs is a multidisciplinary work which has a certain requirements to carefully consider various aspects to accurately simulate the behavior of these devices. In this thesis Ansys Fluent is used as a solver to handle the following complexities of multiphysics simulations of SOFCs:

- Fluid flow, heat transfer, and mass transfer in porous electrodes media (anode and cathode) and gas channels.
- Electrochemical reactions take place on the anode and cathode sides.
- Transport of current and potential field in porous electrodes media and solid conducting regions

All aspects of hydrodynamics, species transport and heat transfer in the flow channels and the porous electrodes are handled by ANSYS Fluent, while the electrochemical reactions and the transport of the current and the potential field in the porous electrodes and in the solid conducting regions are handled by the ANSYS SOFC module. Figure 3.1 illustrates how ANSYS Fluent and the ANSYS SOFC module are combined together to couple and solve the SOFC governing equations [52]:

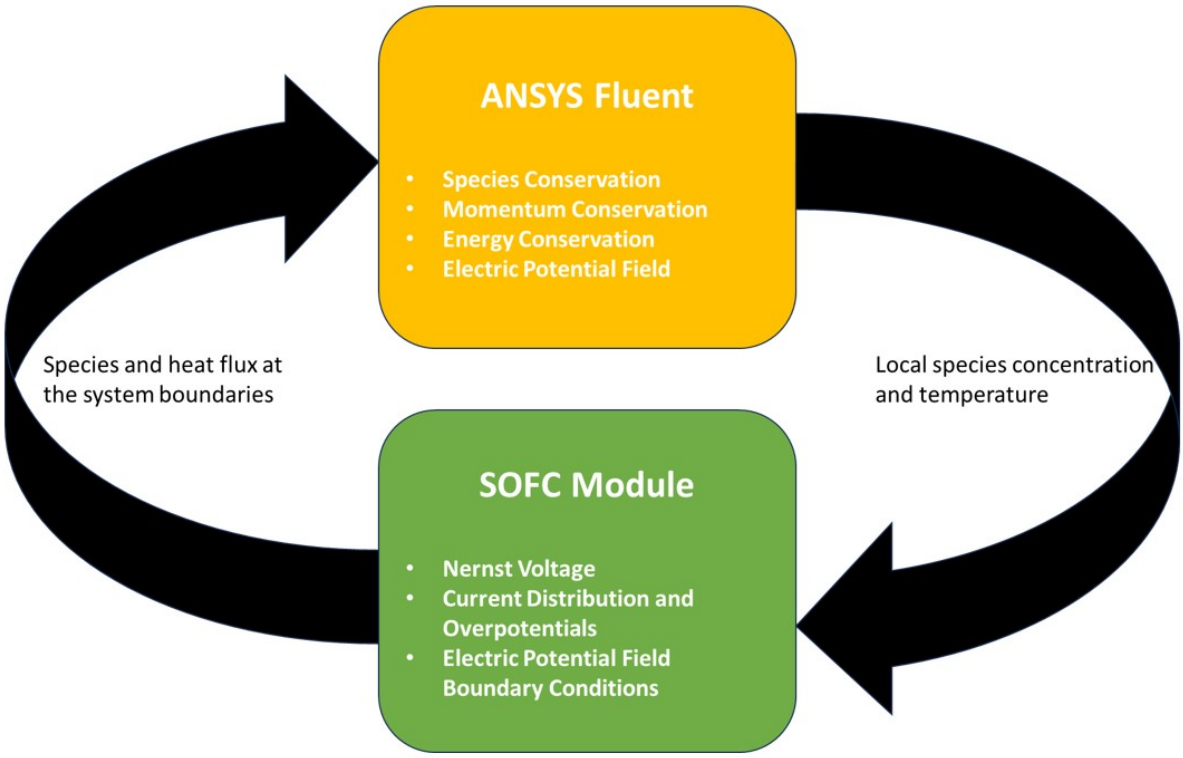

Figure 3.1: The operation structure of the SOFC model in ANSYS Fluent.

Chapter 4

Tubular cell model

Two different models are used to study the performance of tubular SOFC. The first one uses a zero-dimensional model (0-D) is dedicated to evaluate the performance and overpotentials of the tubular SOFC at relatively low operating temperatures of 500 °C, 550 °C, and 600 °C. This temperature range is lower than the typical operating temperature range of SOFCs, which is between 650 °C and 950 °C [53]. While the second tubular SOFC model is a three-dimensional CFD model to not only evaluate the cell performance at three different operating temperatures (650 °C, 700 °C, and 750 °C), but also to study the tubular cell fuel and oxidant utilization, the generated heat from the cell, and the effect of changing the cell structural parameters such as anode porosity, anode thickness, and electrolyte thickness.

4.1 Tubular 0-D model

4.1.1 Tubular 0-D model validation

Figure 4.1 represents the validation process of the 0-D model, and it shows a comparison between the 0-D mathematical model and the experimental data for this study. The validation process considered three different operating temperatures: 500 °C, 550 °C, and 600 °C. The validation process results show the 0-D model has a maximum error lower than 7%, and an average mean square error and average error lower than 4%.

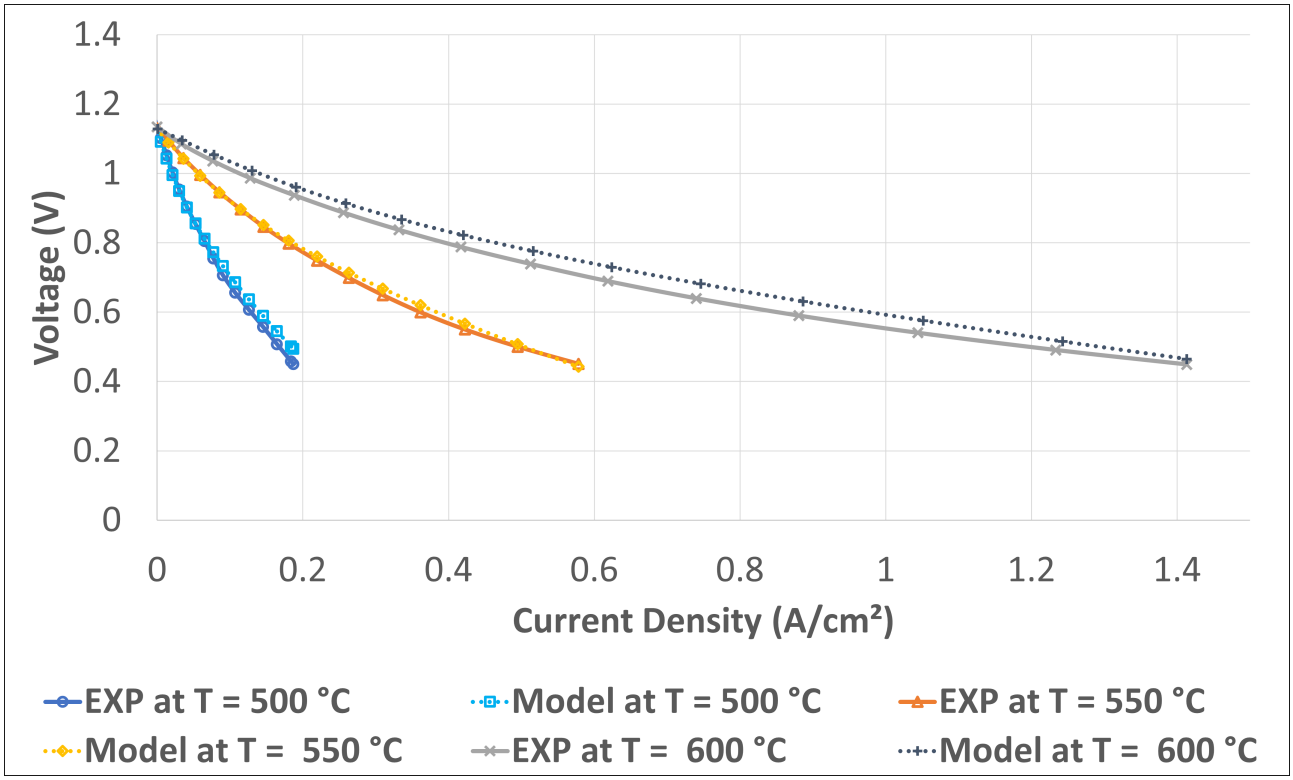

Figure 4.1: Comparison between 0-D model results and experimental data for the tubular cell.

4.1.2 Tubular 0-D model results

The performance of a Solid Oxide Fuel Cell (SOFC) and its associated cell overpotentials are significantly influenced by its operating temperature. The following bullet points discuss how the cell output voltage, activation overpotential, ohmic overpotential, and concentration overpotential are affected by the cell operating temperature:

- Cell output voltage: As a result of the temperature dependency of electrochemical processes, the cell operating temperature strongly influenced the cell performance. The main reason for that is that increasing the operating temperature improves the electrolyte's ionic conductivity, which accelerates oxygen ion transportation and improves the efficiency of electrochemical processes at electrode-electrolyte interfaces. Leading to better cell performance and higher cell voltage and power density. Figure 4.2 shows how increasing the operating temperature improves the performance of the studied tubular cell by illustrating the I-V curve and power density curve at three different operating temperatures.

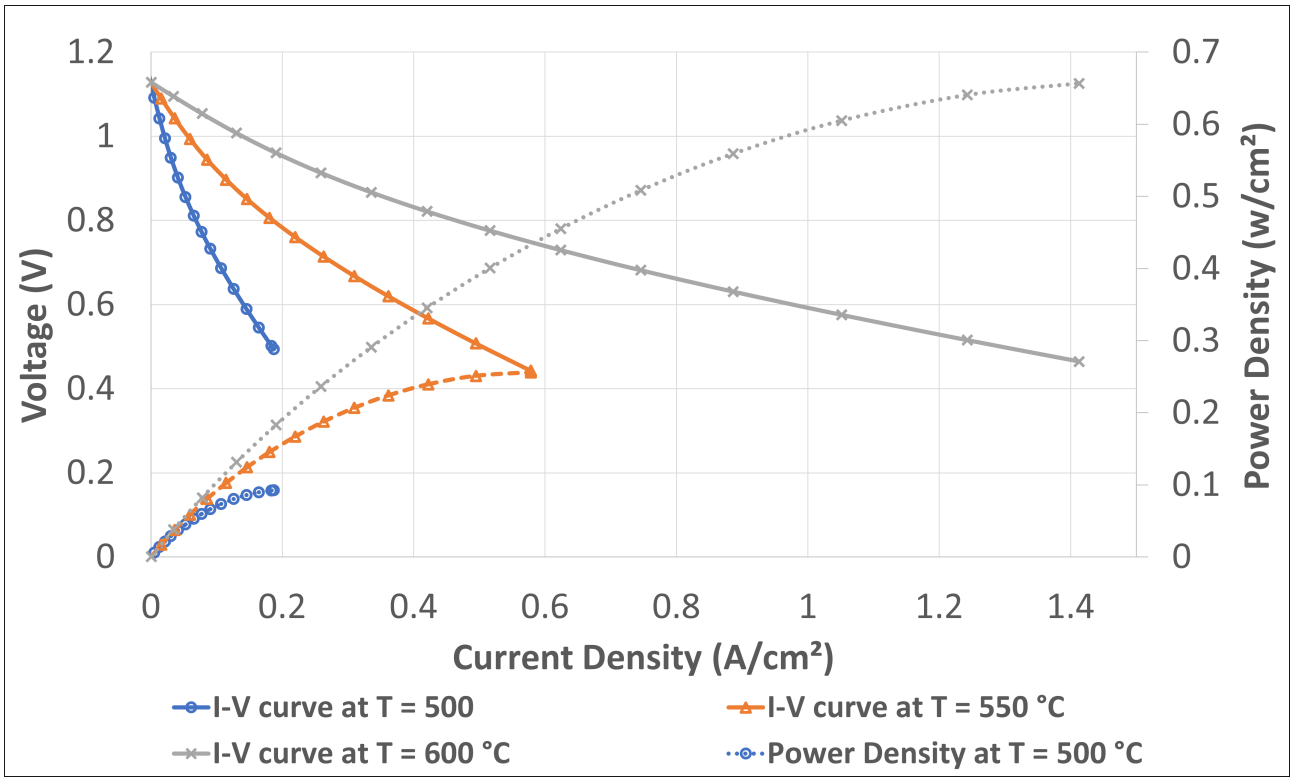

Figure 4.2: The effect of cell's operating temperature on the performance of the tubular cell.

- Activation Overpotential: Activation overpotential refers to the voltage losses associated with the activation energy of the electrochemical reactions at the electrodes. Figure 4.3 shows how lowering the activation overpotential and improving overall cell performance are both achieved by raising the operating temperature. The results show that the 15% reduction in the cell temperature could increase the cell activation overpotential by about 150% at constant current density.

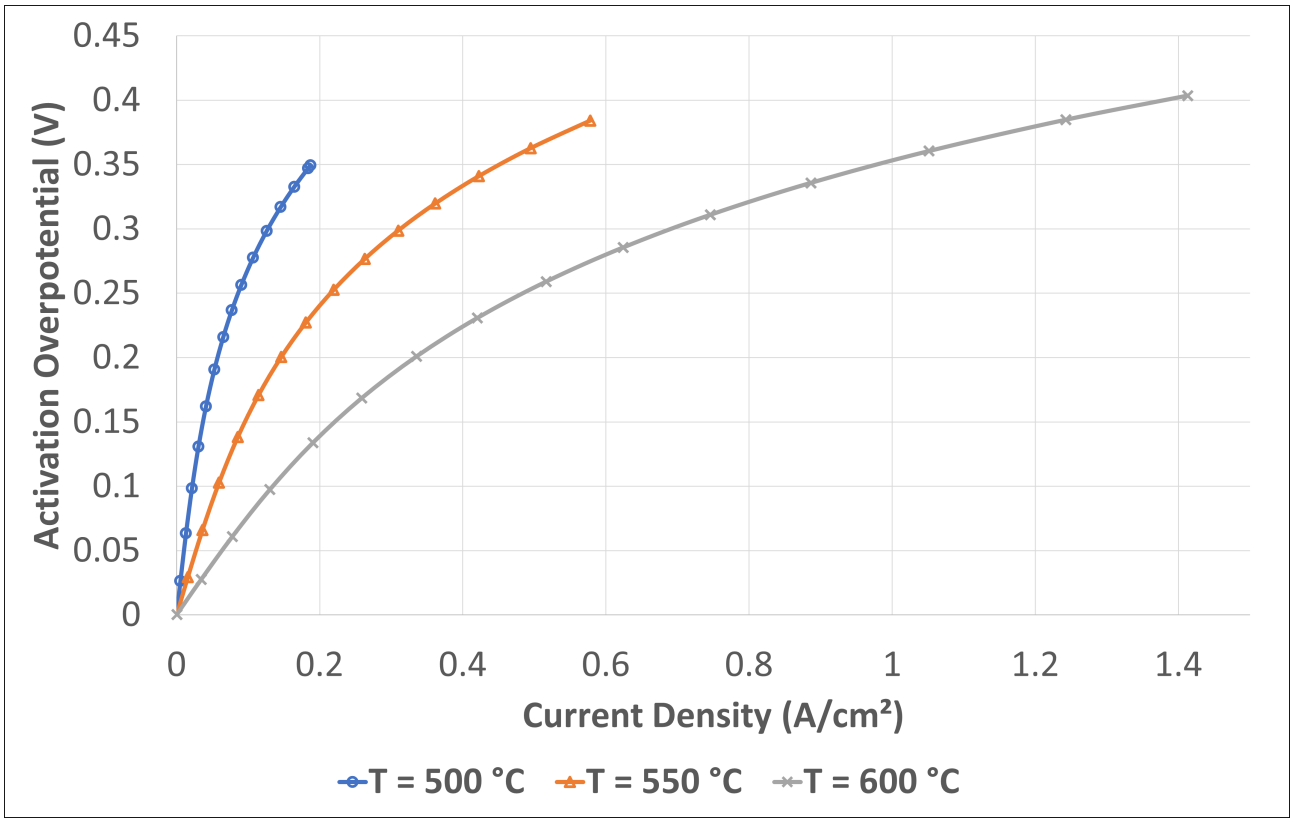

Figure 4.3: The effect of cell's operating temperature on the activation overpotential of the tubular cell.

- Ohmic Overpotential: Ohmic overpotential refers to the voltage losses associated with the resistance of the electrolyte and electrode materials to the charge flow. Since the ionic conductivity of the electrolyte and the electronic conductivity of the electrodes both increase proportionally with increasing operating temperatures. Figure 4.4 shows that higher operating temperatures lead to lower ohmic overpotentials. The results show that the 10% reduction in the cell temperature could lead to a three-times higher cell ohmic overpotential at constant current density.

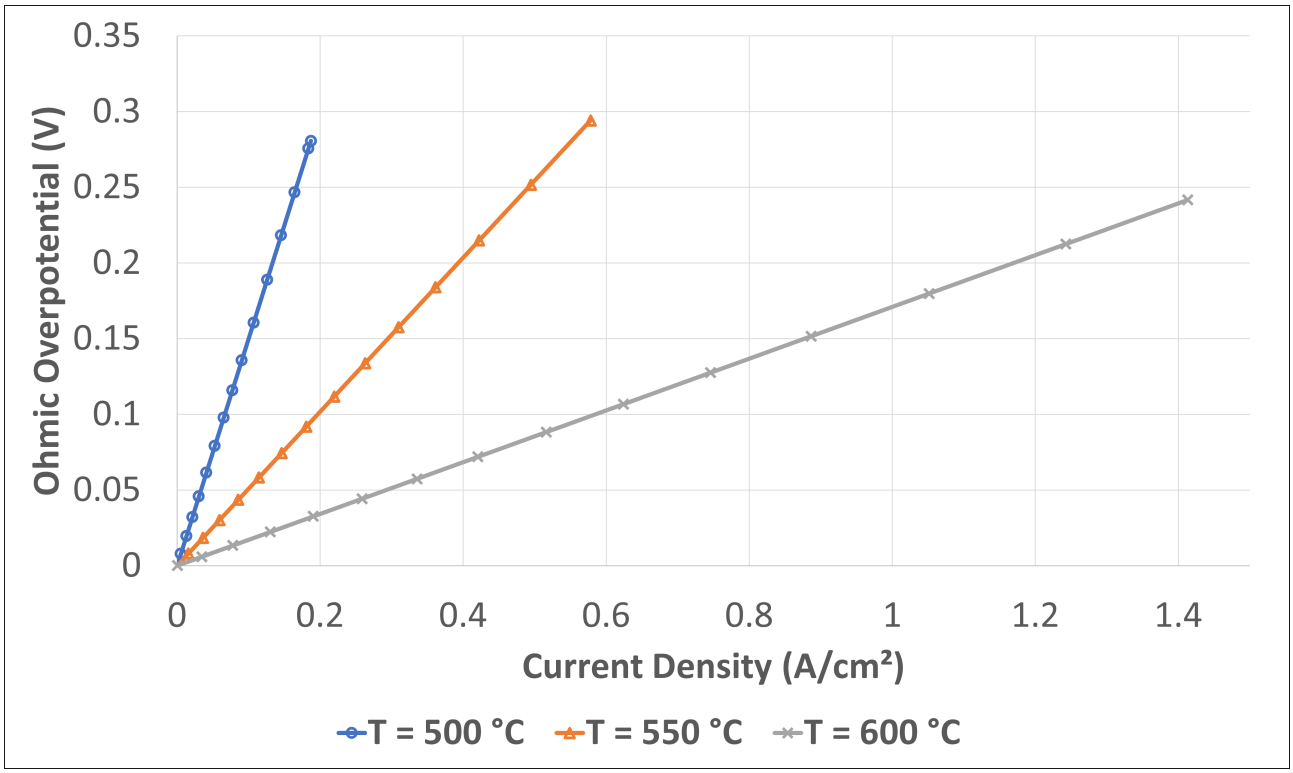

Figure 4.4: The effect of cell's operating temperature on the ohmic overpotential of the tubular cell.

- Concentration Overpotential: Concentration overpotential refers to the voltage losses associated with mass transfer limitations for fuel and oxidant gases in the cell. Despite the fact that higher operating temperatures enhance the diffusion rate of fuel and oxidant gases to where the reactions take place, it significantly reduces the gas density, leading to a higher concentration overpotential. Figure 4.5 shows there is a slight increase in the concentration losses while increasing the operating temperature. The results show that the 15% reduction in the cell temperature could decrease the cell concentration overpotential by less than 5% at constant current density.

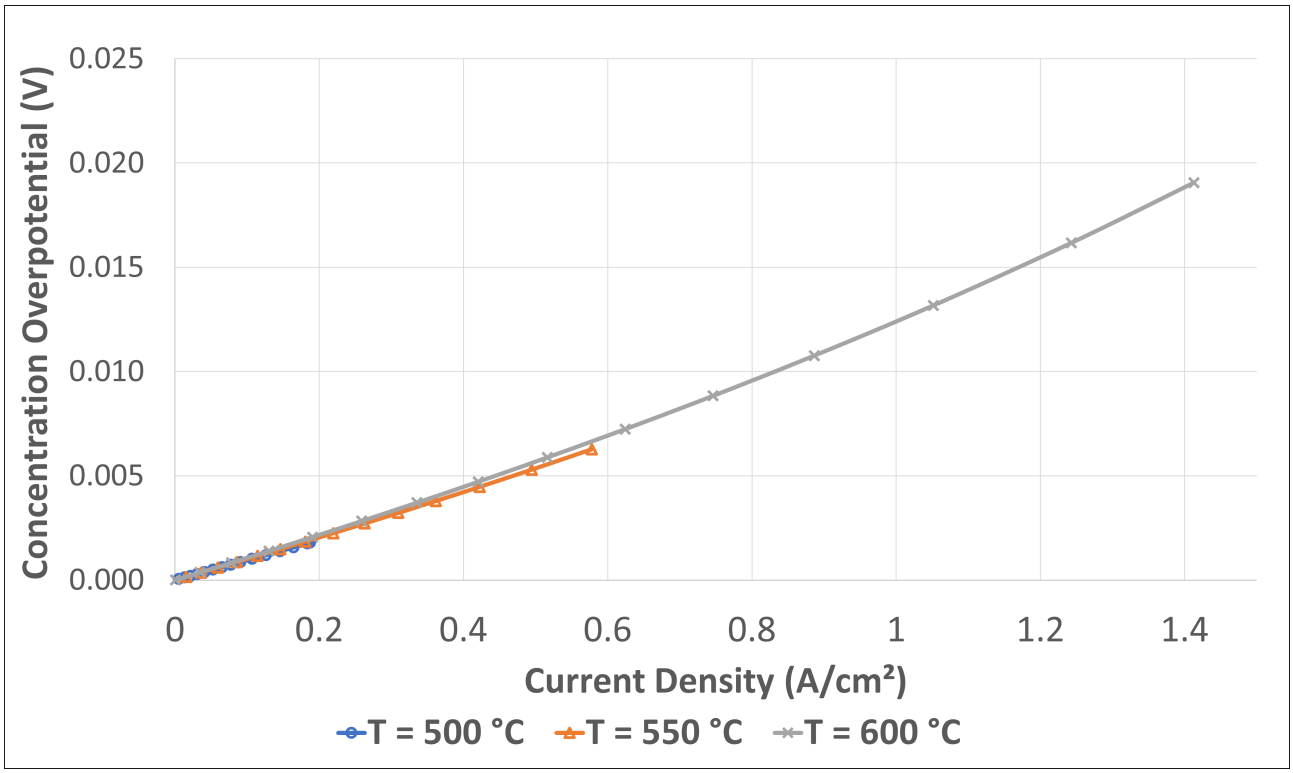

Figure 4.5: The effect of cell's operating temperature on the concentration overpotential of the tubular cell.

Generally, increasing operational temperatures enhances SOFC performance. However, there are several limitations to that, such as high thermal stresses and material compatibility, which significantly affect the cell's durability and lifetime. Since the balance between performance, durability, and system requirements is the SOFC's main challenge, it is crucial to use CFD analysis to investigate how operating temperature affects SOFC performance and to provide a better understanding of temperature distribution, fluid flow, and heat transfer.

4.2 Tubular 3-D model

4.2.1 Tubular geometry model

In this thesis two different geometry models are created: the first one is for a tubular SOFC with 1.5 cm^2 active area, and the second one is for a planar SOFC with 81 cm^2 active area. The tubular geometry illustrated in Figure 4.6 is for 45 mm long concentric tubular cell, with different layers of electrolyte, electrodes, and current collectors. The inner tube represents the fuel channel while the outer tube represents the air channel. Table 4.1 and Figure 4.7 show the dimensions of each layer of the tubular cell.

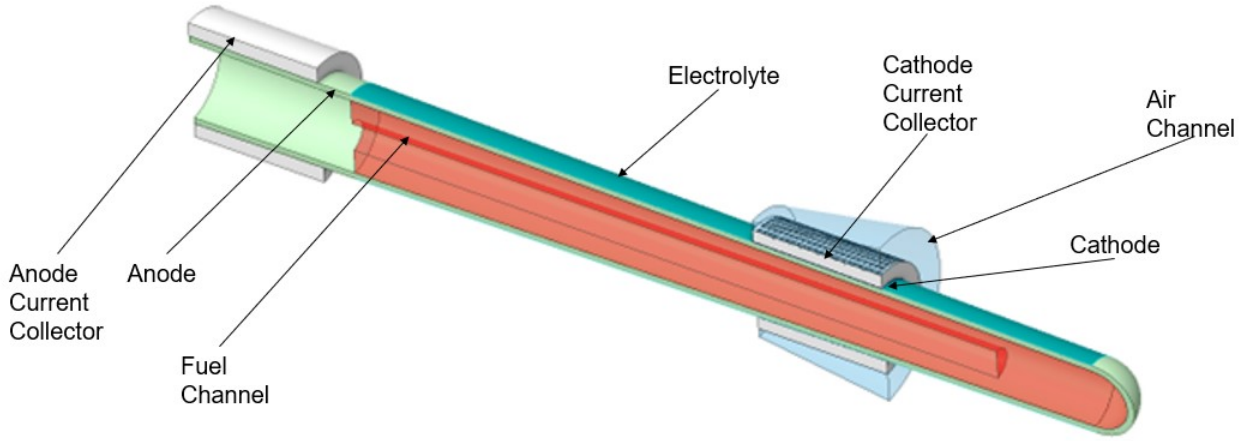

Figure 4.6: Cross section of tubular SOFC model.

Table 4.1: Fabricated 45-mm-long tubular SOFC dimensions.

Zone	**Material**	**Thickness**
Anode support Layer thickness	NiO-YSZ	368 μm
Anode functional layer thickness	NiO-YSZ	20 μm
Electrolyte thickness	YSZ	6.5 μm
Cathode thickness	PNO	7.5 μm

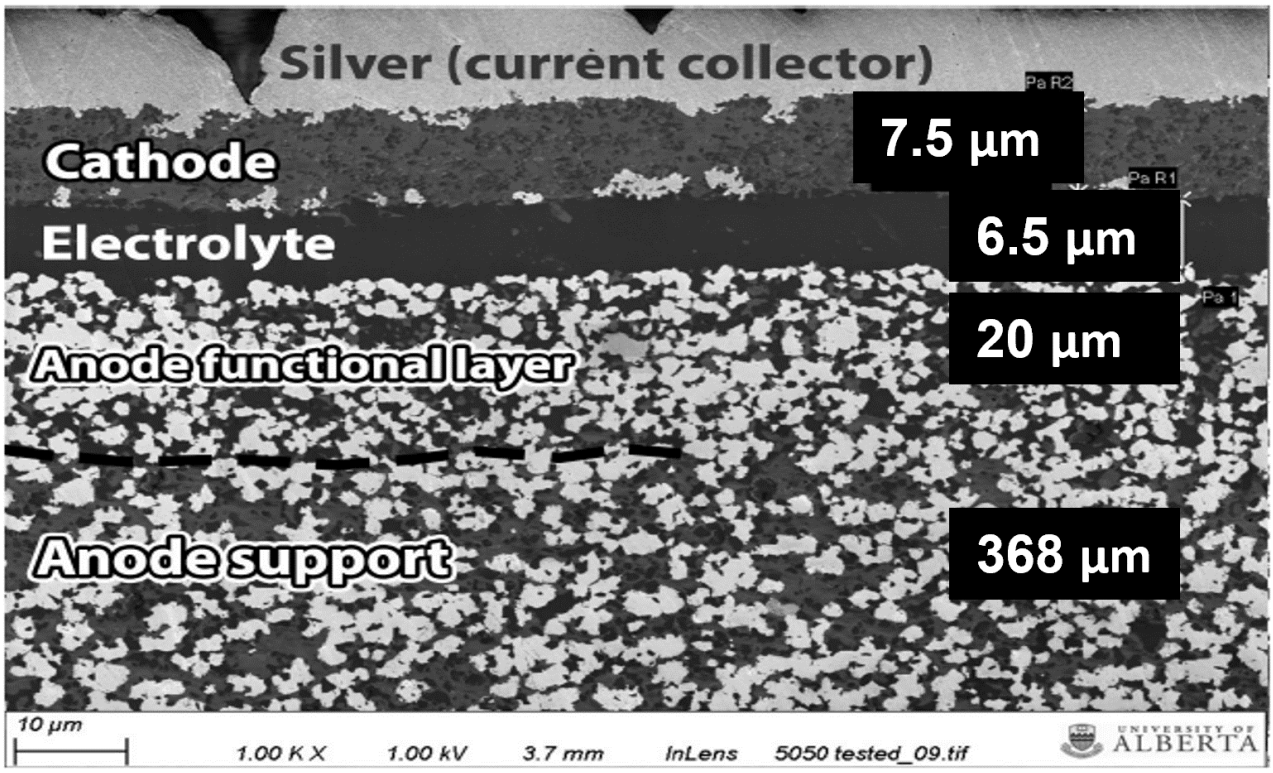

Figure 4.7: SEM image for the tubular anode-supported SOFC shows the thickness of each layer.

4.2.2 Generated mesh properties for the tubular 3-D model

Figure 4.8 represents the mesh independence study of the tubular cell CFD model. The purpose of the mesh independence study was to determine the optimum number of elements and minimise computational time while ensuring adequate model accuracy. The study investigated four different grids, each with a various number of elements (87491, 265174, 783522, 1557083), in order to investigate the impact of changing the mesh size on the cell current density at a cell voltage of 0.5 V. The study shows there isn't a significant change in the current density value after refining the mesh to beyond mesh 3 (783522 elements). Also, Figure 4.9 illustrates the model error percentage at each grid and shows the accuracy of the mesh 3 is very close to the accuracy of mesh 4 with much lower number of elements which significantly reduces the computational time needed:

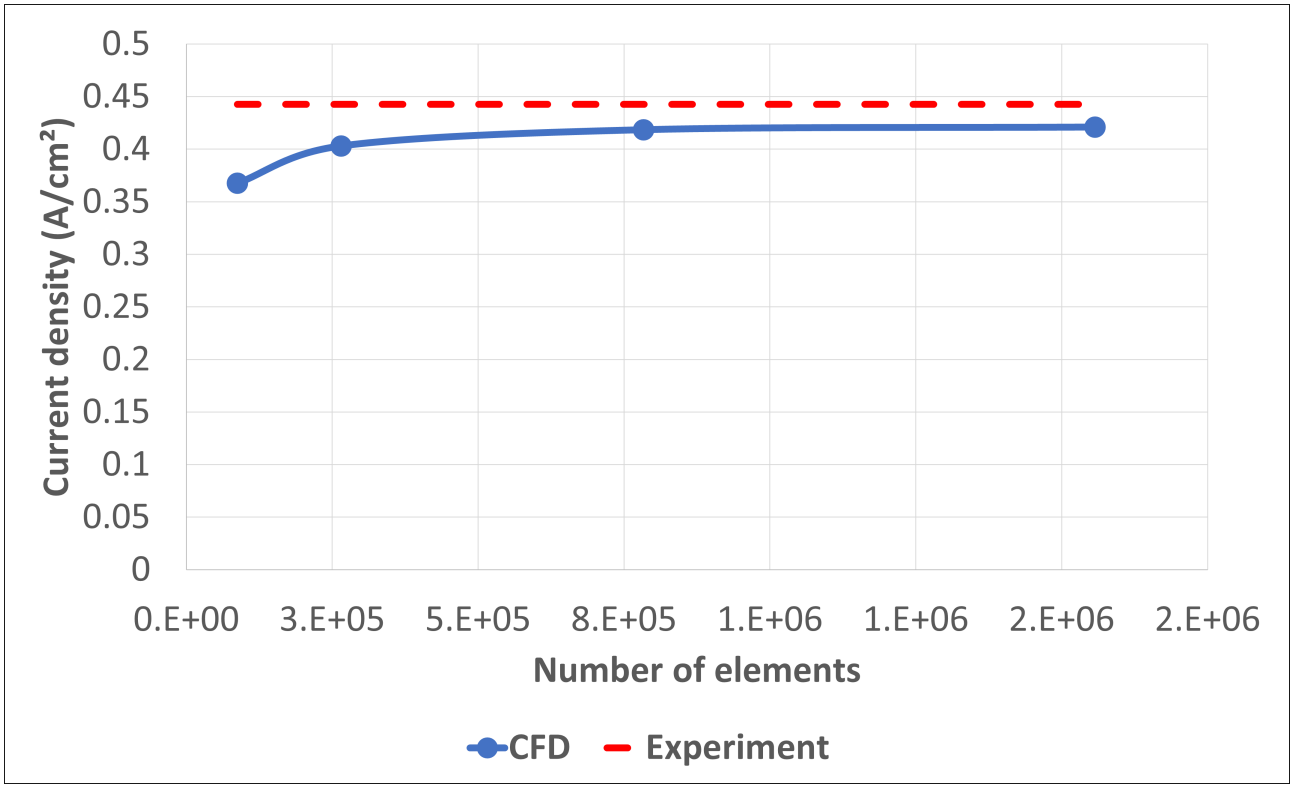

Figure 4.8: Tubular CFD model mesh independence study.

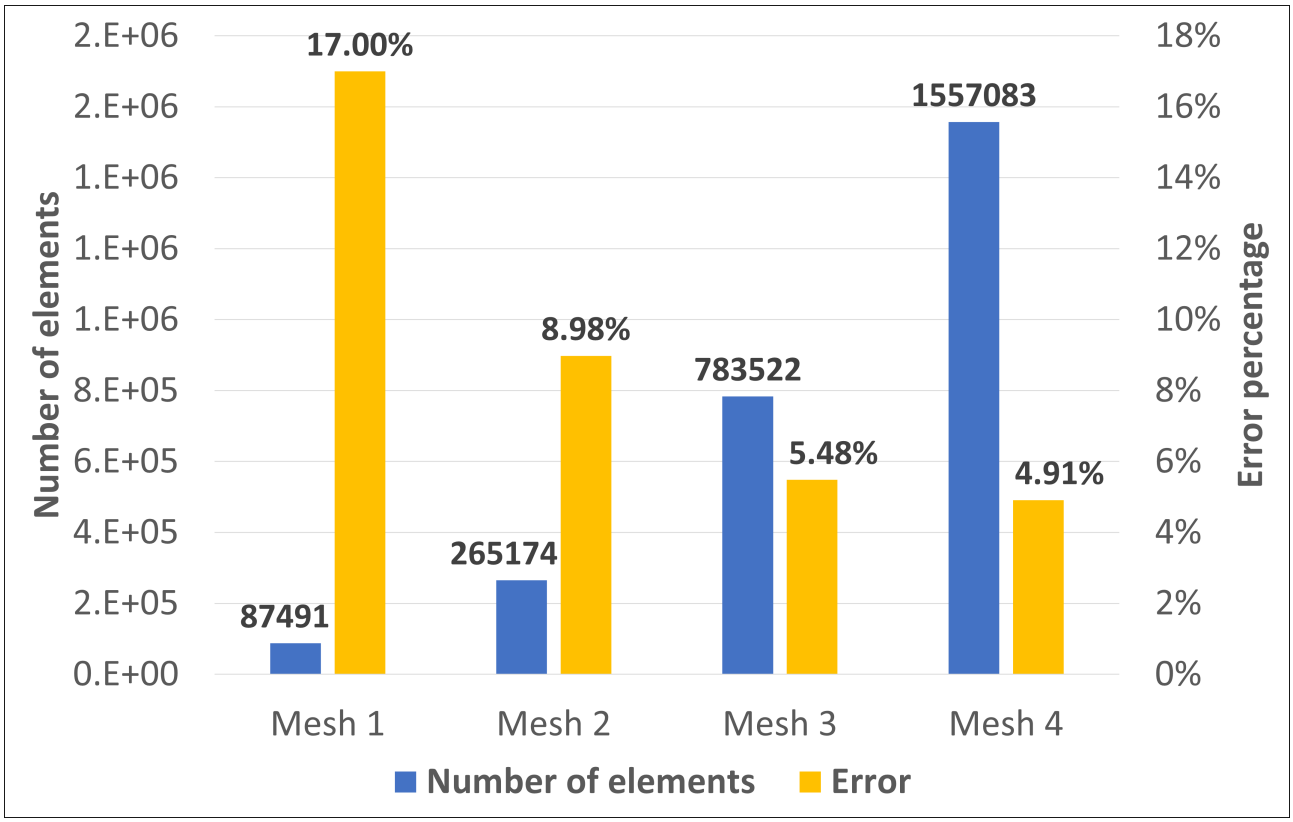

Figure 4.9: Tubular CFD model number of elements and error percentage at each grid.

Figure 4.10 shows the mesh used for a single tubular cell. Based on the mesh independence study, the used mesh scheme is mainly made of hexahedral elements with an element number equal to 783522 and an element size equal to 0.1 mm. The generated mesh important grid metrics are shown in table 4.2:

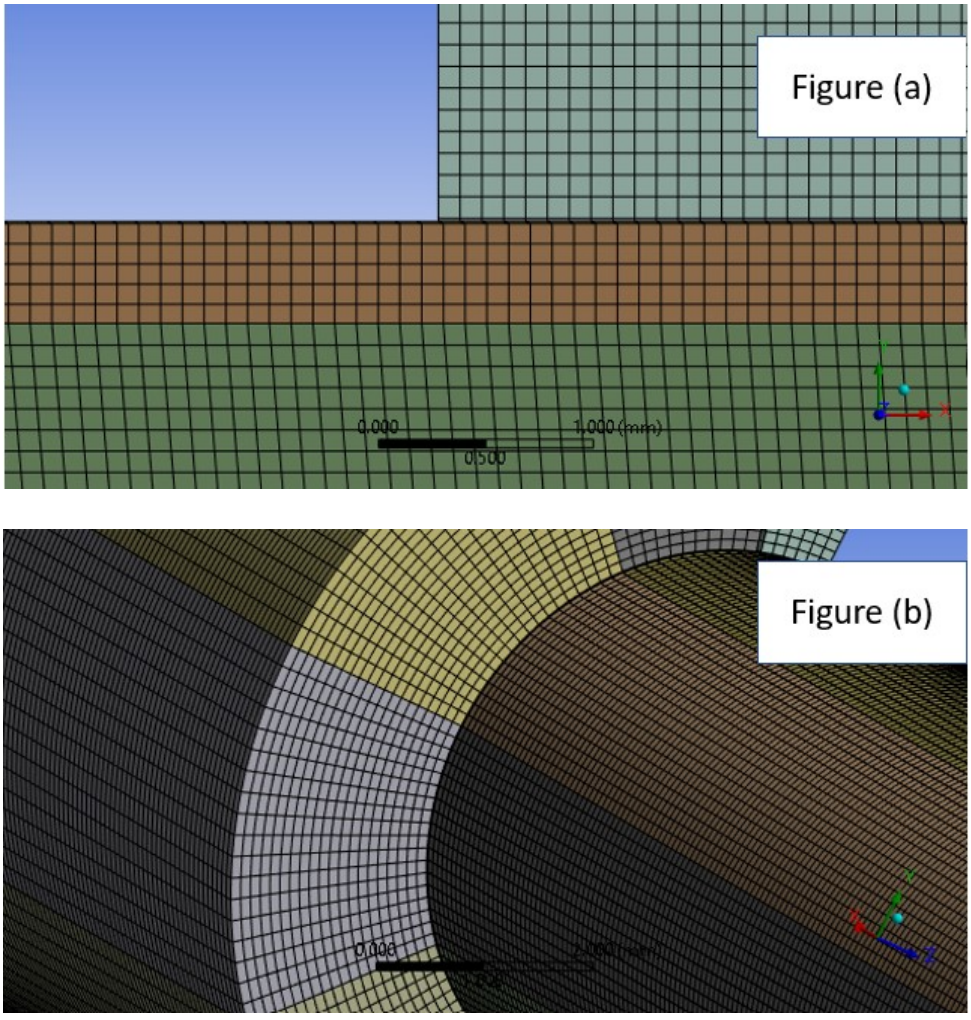

Figure 4.10: Mesh views for tubular cell: a) the cell side view; b) the cell isometric view.

Table 4.2: Tubular SOFC model grid metrics.

Metrics	**Value**
Elements Number	783522
Element Size	0.1 mm
Element Quality	0.896
Aspect Ratio	1.7
Skewness	0.099

4.2.3 Tubular CFD 3-D model validation

The tubular CFD model validation utilised the experimental data for the tubular cell at three different operating conditions. The operating conditions have the same gas flow rates: air flow rate is equal to 100 SCCM, nitrogen flow rate is equal to 0 SCCM, and hydrogen flow rate is equal to 50 SCCM, while the operating temperature varies between 650 °C, 700 °C, and 750 °C. The model average error was lower than 5%, the root mean square error was 5%, and the maximum error was about 10% which is considered an acceptable degree of accuracy for SOFC modeling. Due to the more simplicity of the 0-D model, it has a better accuracy than the CFD 3-D model. Figure 4.12 shows the comparison between the CFD model results and the experimental data results at three different operating conditions:

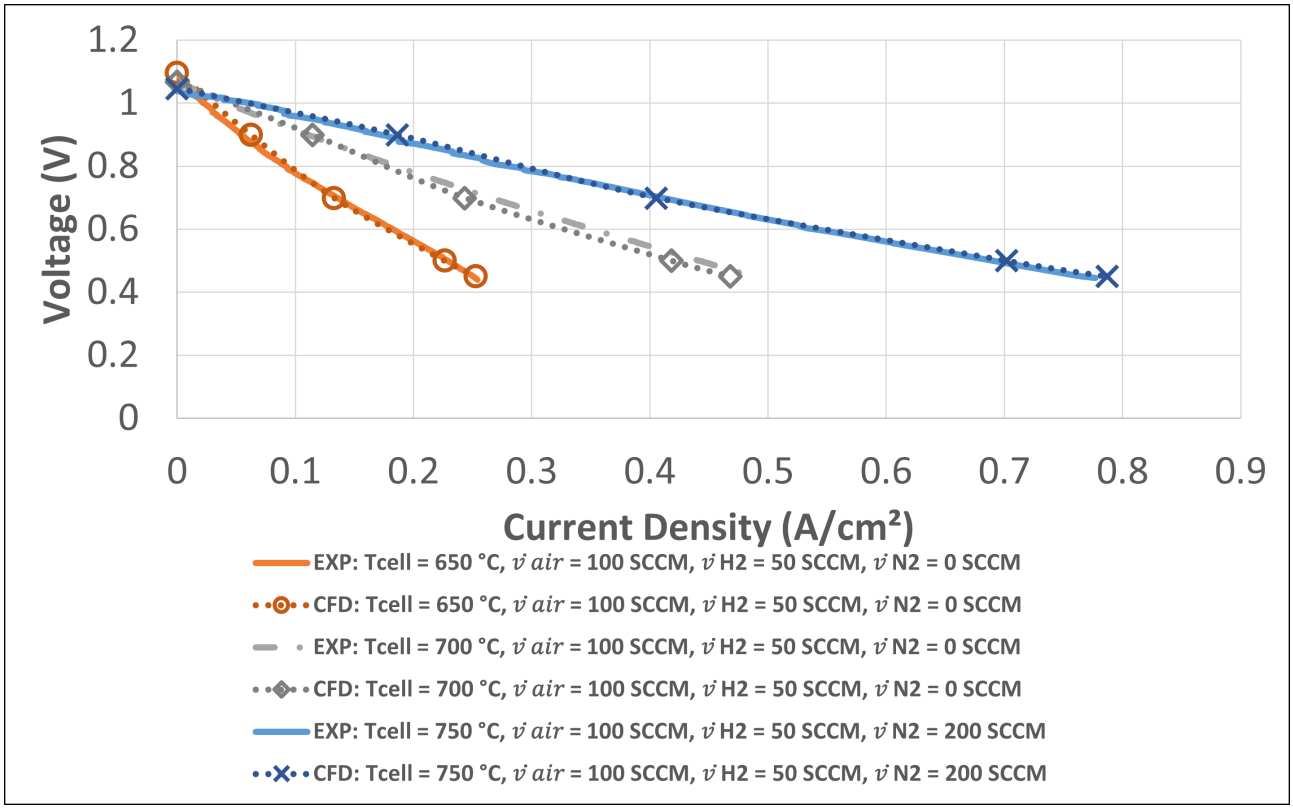

Figure 4.11: Comparison between CFD 3-D model results and experimental data for tubular cell.

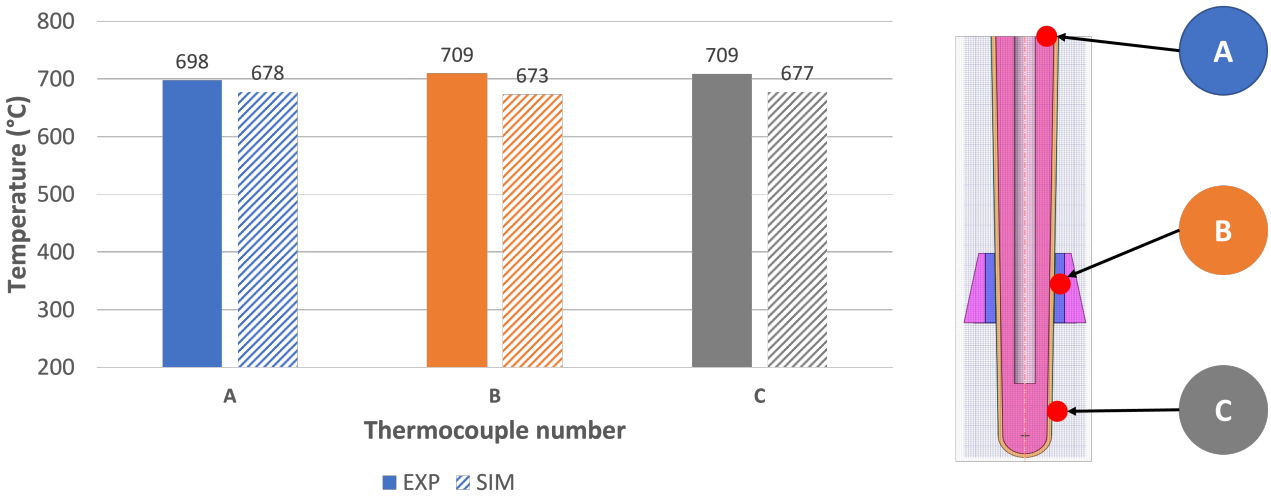

Figure 4.12: Comparison between the temperature measurements of CFD model results and experimental data for tubular cell.

4.2.4 Tubular CFD 3-D model results

After successfully completing the validation process, a set of operating conditions was selected to extensively study the tubular cell. The selected operating parameters are as follows: The hydrogen flow rate was 50 SCCM, the air flow rate was 100 SCCM, the hydrogen inlet temperature was 700 °C, the air inlet temperature was 700 °C, the cell operating temperature was 700 °C, and the fuel flow contains 97% hydrogen and 3% of water vapor, and the air flow contains 79% nitrogen and 21% oxygen. Table 4.3 shows the operating conditions of the tubular cell study.

Table 4.3: Operating condition of the tubular cell study.

Parameter	**Value**
Hydrogen flow rate	50 SCCM
Air flow rate	100 SCCM
Hydrogen inlet temperature	700 °C
Air inlet temperature	700 °C
Cell temperature	700 °C
Fuel flow species (mass fraction)	97% H_2, 3% H_2O
Air flow species (mass fraction)	79% N_2, 21% O_2

Figure 4.13 shows the I-V curve, the power density, and the generated heat shown earlier in equation 3.31 of the tubular cell. The x-axis represents the current density, the right y-axis represents the cell voltage, and the right y-axis represents the power density and the generated heat per area (w/cm^2). The figure describes how the generated heat from the cell is proportionally increased at high current density because the higher the current density, the higher the cell overpotenials, which leads to higher heat generated from the cell. For example, the electrical power produced and the generated heat represent 45% and 55% respectively, of the total cell output power at a current density equal to 0.45 A/cm^2. The model could be used not only to estimate the electrical power output of the cell, which is important for electrical load calculation and evaluating the cell performance at various electrical loads, but also to calculate the generated heat from the cell for proper cell thermal management to prevent overheating

and thermal stress failures and to utilise the surplus heat for heating applications if needed.

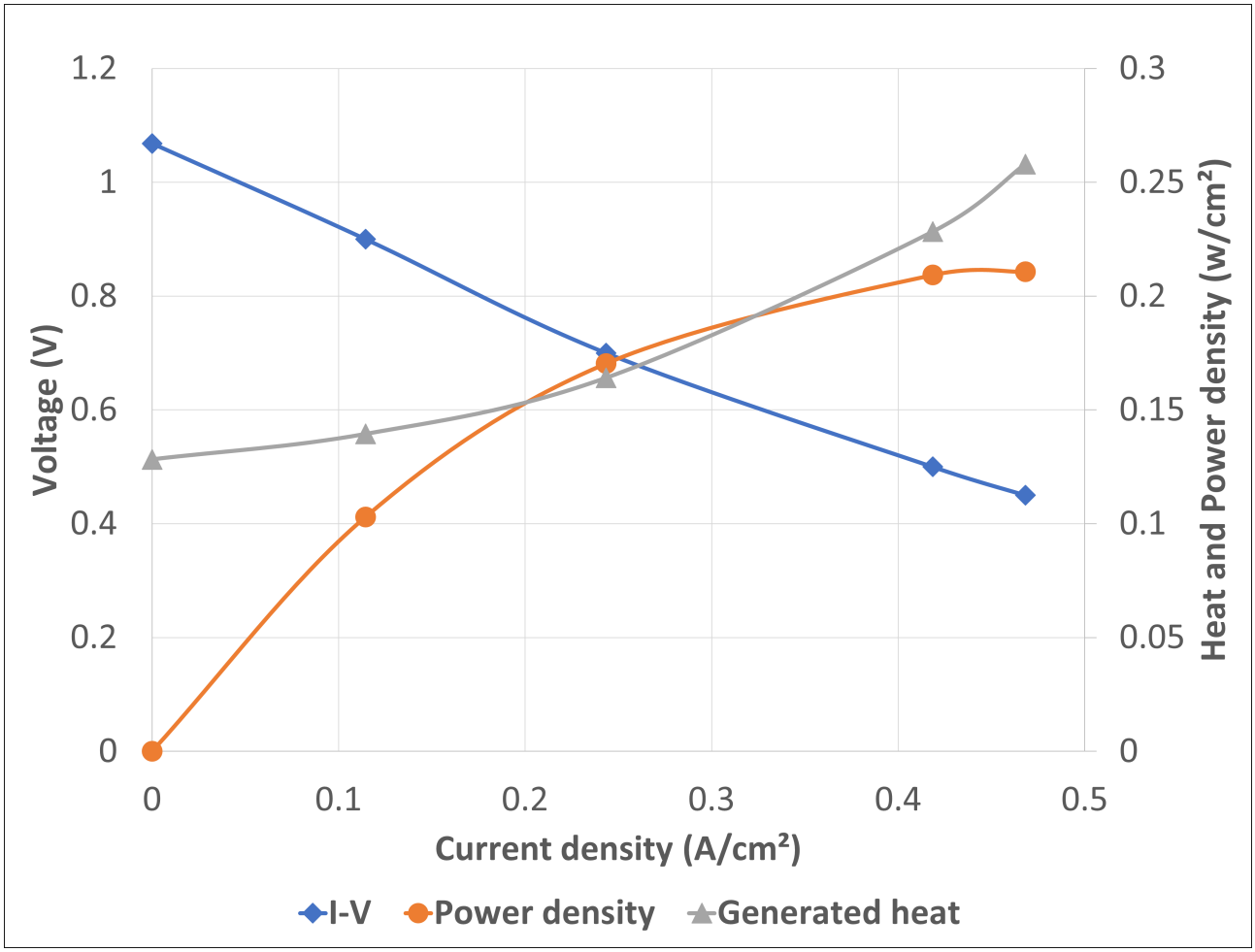

Figure 4.13: The figure represents the I-V curve, the power density, and the generated heat of the tubular cell.

Figure 4.14 represents the hydrogen mass fraction distribution across the NiO-YSZ anode layer surface; moreover, the CFD model can estimate the hydrogen mass fraction difference at the fuel inlet ports and fuel outlet ports, which allows for the calculation of the fuel utilisation factor and the total hydrogen consumption. By knowing the consumed hydrogen, the model can also calculate the fuel inlet energy, generated heat, and the cell's electrical and overall efficiency. The hydrogen mass fraction is scaled within the range of 0.94 to 1 in order to enhance the visual representation of the amount of how hydrogen is utilized inside the active area. While Figure 4.15 represents the oxygen mass fraction across the PNO cathode surface and how oxygen is consumed across the cell, the model shows the oxygen mass fraction at the air inlet ports is

0.21, and it reduced gradually until it reached the air outlet ports. The oxygen mass fraction is scaled within the range of 0.205 to 0.21 in order to enhance the visual representation of the amount of how oxygen is utilized. The results could be very beneficial to optimise the design of fuel and oxidant channels; additionally, the model could be used to predict the outlet hydrogen and air flow rate, which could be used to diagnose any gas leakage problem. Moreover, the model can calculate the fuel and air utilization factors by determining the utilised gas mass flow rate, which is equal to the outlet gas mass flow rate subtracted from the inlet gas flow rate divided by the inlet gas flow rate, as shown in the following equation:

$$U_f = \frac{\dot{m}_{fu}}{\dot{m}_{fi}} = \frac{\dot{m}_{fi} - \dot{m}_{fo}}{\dot{m}_{fi}} \tag{4.1}$$

Where U_f is the fuel utilization factor, $\dot{m}_{fu}$ is the utilized fuel mass flow rate, $\dot{m}_{fi}$ is the inlet fuel mass flow rate, and $\dot{m}_{fo}$ is the outlet fuel mass flow rate.

$$U_o = \frac{\dot{m}_{ou}}{\dot{m}_{oi}} = \frac{\dot{m}_{oi} - \dot{m}_{oo}}{\dot{m}_{oi}} \tag{4.2}$$

Where U_o is the oxygen utilization factor, $\dot{m}_{ou}$ is the utilized oxygen mass flow rate, $\dot{m}_{oi}$ is the inlet oxygen mass flow rate, and $\dot{m}_{oo}$ is the outlet oxygen mass flow rate.

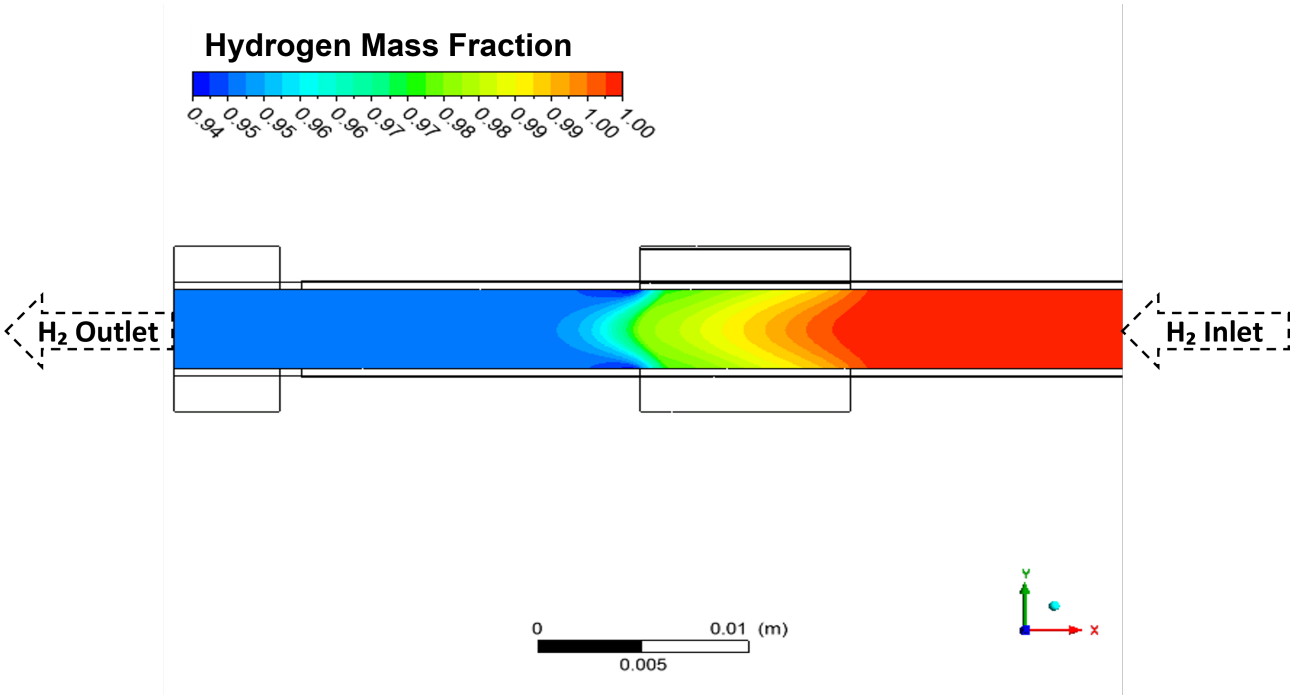

Figure 4.14: Hydrogen mass fraction across the tubular cell at the operating conditions shown in Table 4.3.

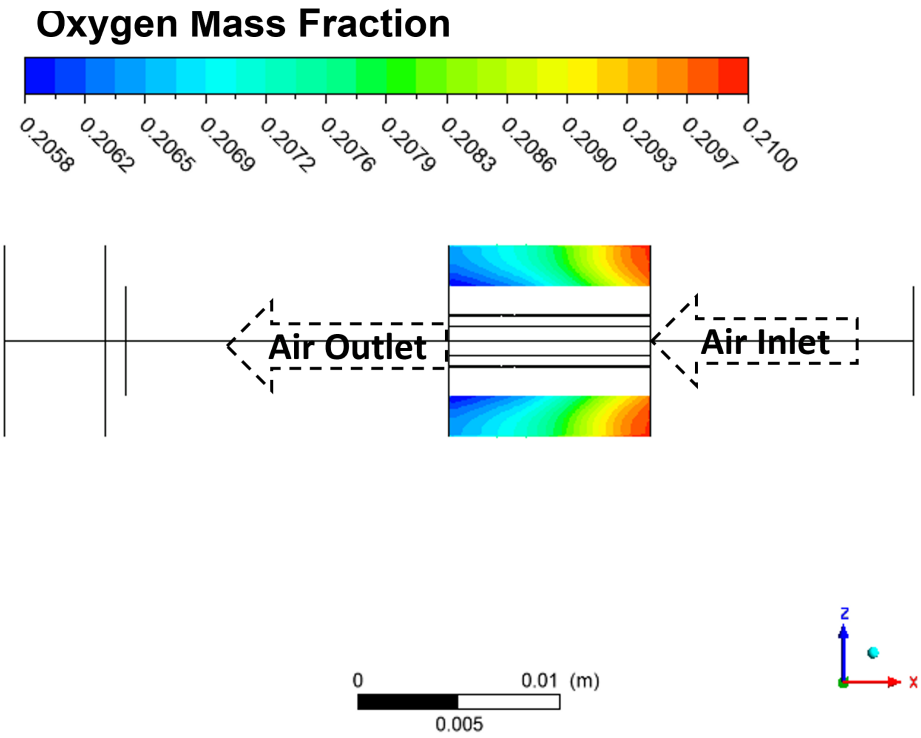

Figure 4.15: Oxygen mass fraction across the tubular cell at the operating conditions shown in Table 4.3.

Chapter 5

Planar cell model

5.1 Planar geometry model

Figure 5.1 shows the exploded diagram for a 9 x 9 cm single planar cell with an active area 81 of cm^2. The current collectors, electrodes, and the electrolyte are stacked together to form the single planar cell shown in Figure 5.2. The cell specifications are shown in Table 5.1:

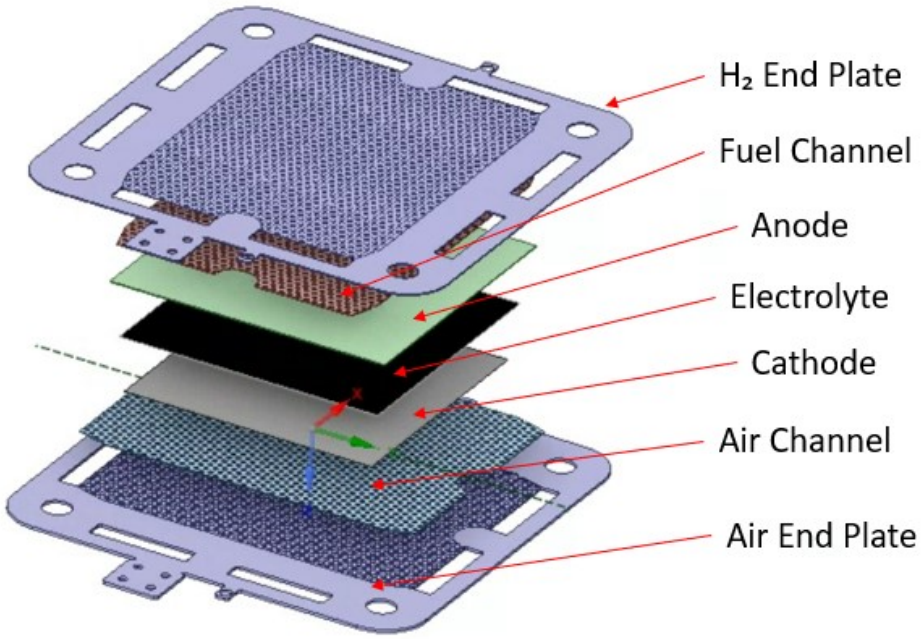

Figure 5.1: The exploded diagram of the studied planar cell in this thesis.

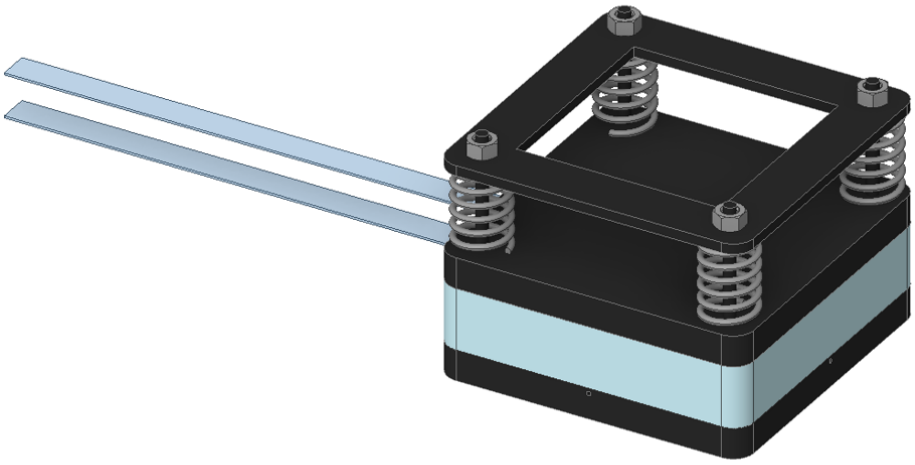

Figure 5.2: The assembled planar cell isometric view.

Table 5.1: The studied Planar SOFC specifications.

Zone	**Material**	**Dimension**
Anode Support Layer Thickness	NiO-YSZ	360 μm
Anode Functional Layer Thickness	NiO-YSZ	40 μm
Electrolyte Thickness	YSZ	6 μm
Cathode Thickness	LSC	15 μm

As discussed in the previous chapter, carrying out a mesh independence analysis is an essential step in CFD modeling. The process allows for determining the optimal mesh resolution to achieve precise and efficient results while at the same time minimising computational resources. Figure 5.3 shows the mesh independence study of the planar cell CFD model. The study investigates the effect of changing the number of elements for four different grids on the cell current density at a cell voltage equal to 1 V. While Figure 5.4 represents the number of elements and the error value for each grid, the results show the optimum mesh is mesh 3 (3530059 elements) because it has about 35% less number of elements than mesh 4 and almost

has the same accuracy. Therefore, a grid size of 3530059 elements has been used to perform all the planar cell modeling in this thesis. Figure 5.5 shows the selected mesh for the planar cell study, and the corresponding metrics associated with this mesh are provided in Table 5.2:

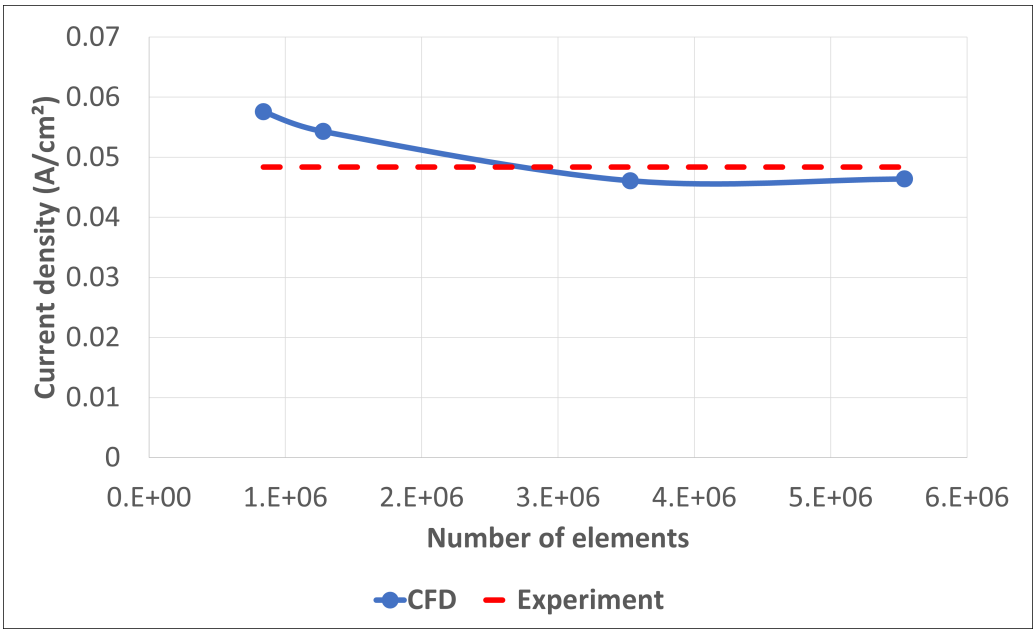

Figure 5.3: Planar CFD model mesh independence study.

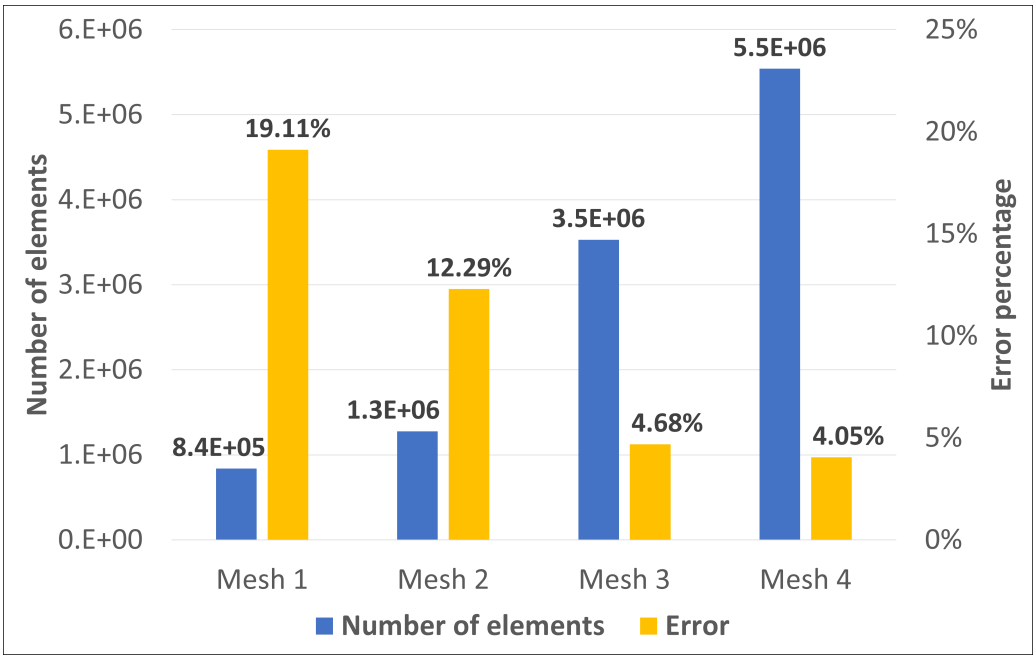

Figure 5.4: Planar CFD model number of elements and error percentage at each grid.

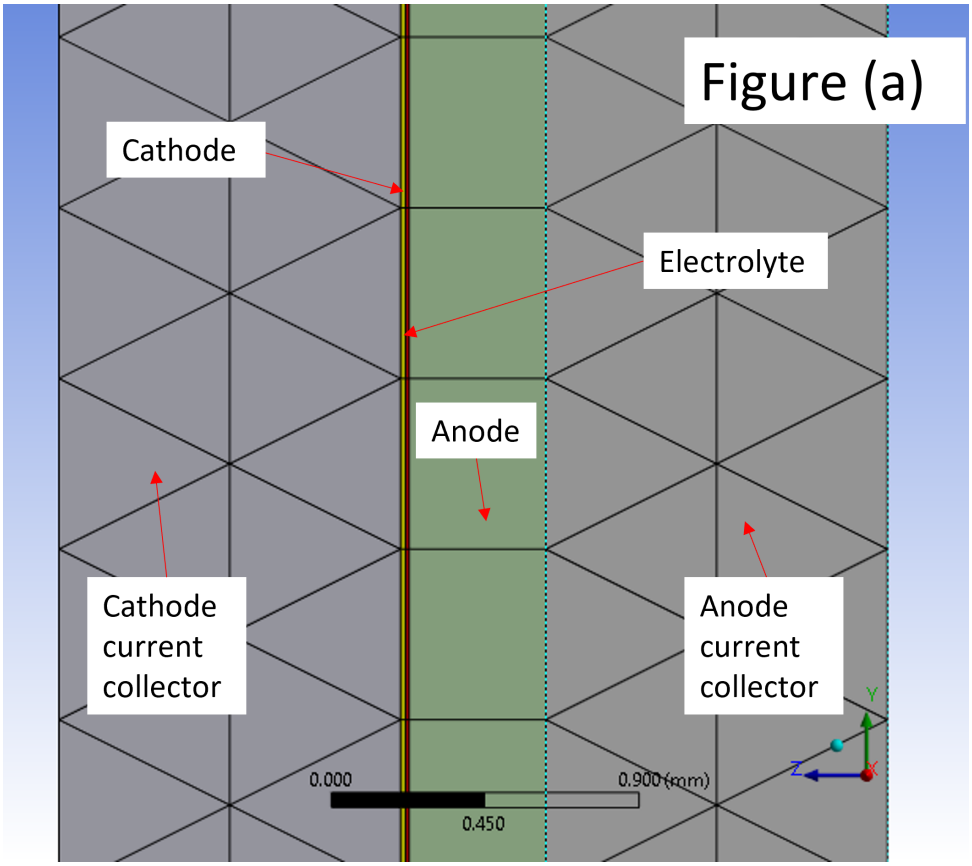

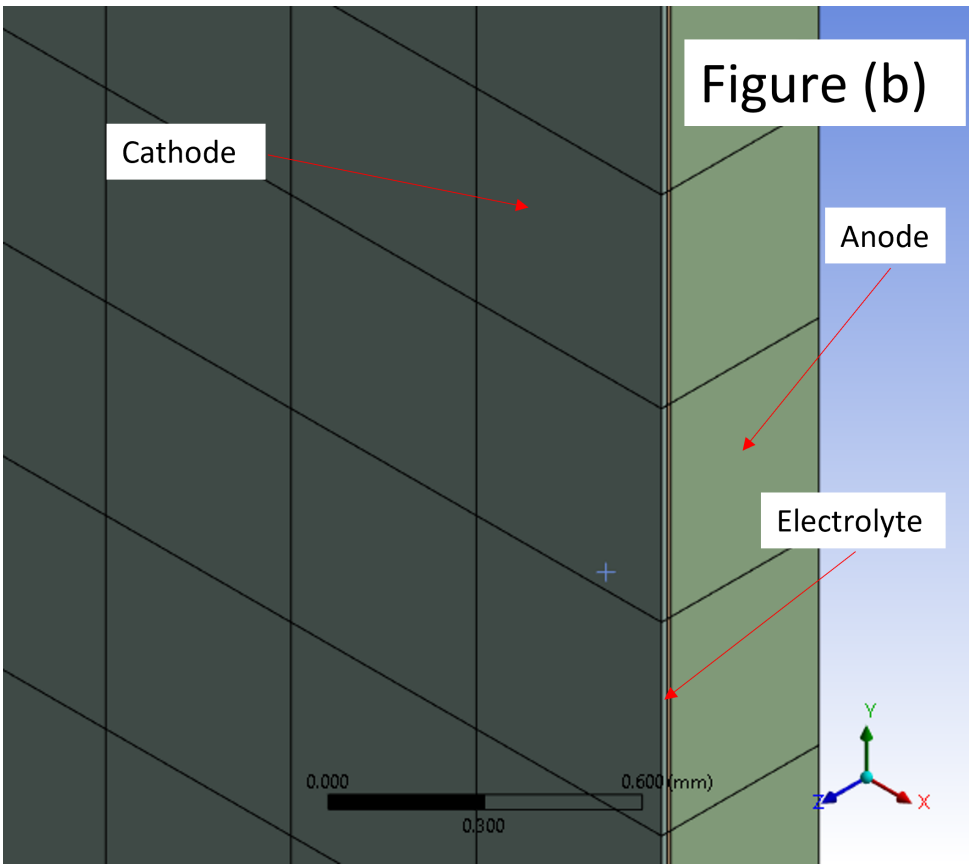

Figure 5.5: Mesh views for planar cell: a) the cell side view; b) the cell isometric view.

Table 5.2: Planar SOFC model grid metrics.

Metrics	**Value**
Elements Number	3530059
Element Size	0.5 mm
Element Quality	0.875
Aspect Ratio	2.1
Skewness	0.11

Table 5.3 shows the material specifications for the anode, the cathode, and the electrolyte, such as the porosity of each layer, specific heat, thermal and electrical conductivity, and density. While table 5.4 shows the operating conditions under which the temperature profile and thermal gradients were studied.

Table 5.3: Specifications of the planar cell study.

Parameter	**Value**	**Unit**	**References**
Anode porosity	0.4		SEM Imaging
Anode specific heat	377	J kg^{-1} K^{-1}	[54]
Anode thermal conductivity	11	W m^{-1} K^{-1}	[54]
Anode electrical conductivity	$\frac{9.0x10^7}{T}e^{-1150/T}$	sm^{-1}	[55]
Anode density	4760	kgm^{-3}	[56]
Cathode porosity	0.4		SEM Imaging
Cathode specific heat	377	J kg^{-1} K^{-1}	[55]
Cathode thermal conductivity	2.37	W m^{-1} K^{-1}	[56]
Cathode electrical conductivity	$\frac{4.0x10^7}{T}e^{-1200/T}$	sm^{-1}	[56]
Cathode density	4640	kgm^{-3}	[55]
Electrolyte specific heat	100	J kg^{-1} K^{-1}	[54]
Electrolyte thermal conductivity	2.7	W m^{-1} K^{-1}	[56]
Electrolyte electrical conductivity	3.34 x 10^4 $e^{-10300/T}$	sm^{-1}	[54]
Electrolyte density	6000	kg m^{-3}	[56]

Table 5.4: Operating conditions of the planar cell study.

Parameter	**Value**
Hydrogen flow rate	400 SCCM
Air flow rate	400 SCCM
Hydrogen inlet temperature	100 °C
Air inlet temperature	100 °C
Fuel flow Species (mass fraction)	100% H_2, 0%H_2O
Air flow Species (mass fraction)	79% N_2, 21%O_2

5.2 Planar model validation

At two different operating temperatures, 600 °C and 650 °C, which are in the recommended operating temperature range suggested by the cell manufacturer, the planar CFD model validation was carried out with the same air flow rate of 400 SCCM, two different nitrogen flow rates of 0 and 200 SCCM, and two different hydrogen flow rates of 200 and 400 SCCM. Figure 5.6 shows the comparison between the CFD model results and the experimental data results at three different operating conditions. The model total average error is less than 5%, the root mean square error is less than 6% and the maximum error is less than 10% which meets the required degree of accuracy of CFD models in the same application. The figure also shows how increasing the operating temperature improves the cell performance; for example, increasing the operating temperature from 600 °C to 650 °C at a constant hydrogen and air flow rate could increase the cell output voltage by 35% at the same current density.

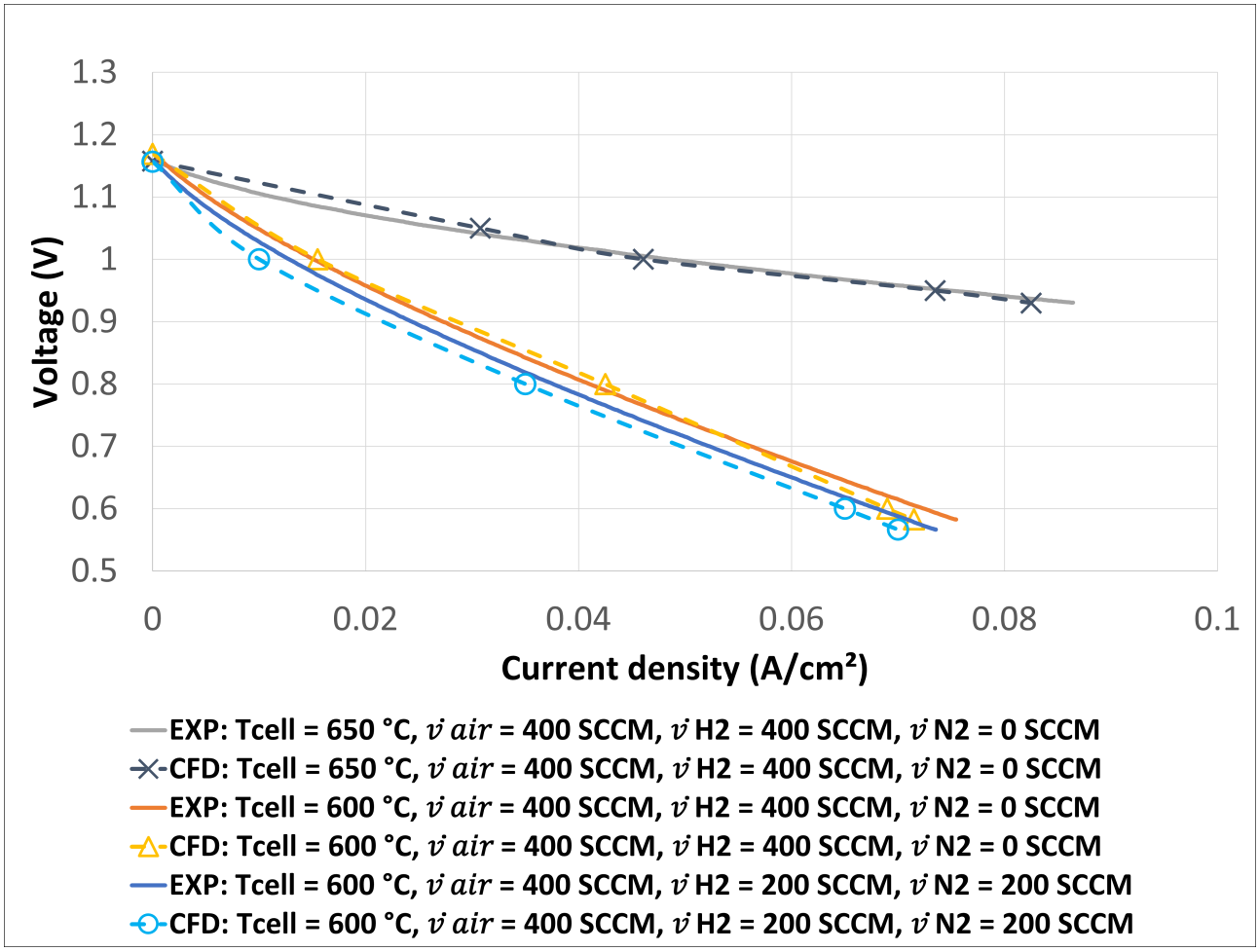

Figure 5.6: Comparison between CFD model results and experimental data for planar cell.

5.3 Planar CFD model results

The planar CFD model in this thesis focuses on studying the temperature profile, the thermal gradient across the cell, and the fuel and oxidant consumption. The importance of studying these parameters is to estimate the thermal gradient across the cell and how hydrogen and oxygen are consumed at the NiO-YSZ anode and LSC cathode sides, respectively. By having an accurate and reliable CFD model that can provide a better understanding of mass transfer, charge transfer, and the cell thermal gradient. This model can be utilised to improve cell performance by enhancing charge and mass transfer and decreasing the cell degradation rate by lowering the cell thermal gradient.

5.3.1 Planar cell temperature profile and thermal gradients

For the anode, cathode, and electrolyte, the CFD model is used to investigate the temperature profile and the thermal gradient in X and Y directions for each layer. Additionally, it displays the highest and average thermal gradients for each layer, which are represented by the temperature differential over a length in centimetres. Studying the cell temperature profile and thermal gradients play a crucial role to prevent operation failure that could be caused by excessive thermal stress within the SOFC components, the maximum allowable temperature gradient is 10 °C/cm. Higher thermal gradient could cause lead to cell breakdown due to high thermal stress [57].

Anode temperature profile and thermal gradient

Figure 5.7 shows the temperature profile on the NiO-YSZ anode surface in contact with the fuel channel. The hydrogen enters the cell from the left side and exits from the right side, and the air enters from the top of the cell and exists from the bottom. The figure shows the NiO-YSZ anode hot zone is at the right bottom of the cell. The coldest spots are at the inlet of hydrogen and air because the gases inlet temperature is 100 °C.

Figures 5.9 and 5.11 illustrate the temperature distribution and the thermal gradient across the x and y axes, respectively. The first figure represents the NiO-YSZ anode surface thermal gradient across the x-axis, and y is equal to 25 cm, and the second figure represents the NiO-YSZ anode surface thermal gradient across the y-axis, and x is equal to 90 cm. The location of the selected planes for the study is shown in Figures 5.8 and 5.10. The highest NiO-YSZ anode surface thermal gradient across the x-axis is equal to 60 °C/cm, which is six times higher than the maximum allowable thermal gradient and leads to a high thermal gradient, while the average NiO-YSZ anode surface thermal gradient across the x-axis is equal to 5.6 °C/cm. The highest NiO-YSZ anode surface thermal gradient across the y-axis is equal to 8.6 °C/cm, while the average NiO-YSZ anode surface thermal gradient across the x-axis is equal to 2.5 °C/cm, which is less than the maximum allowable thermal gradient.

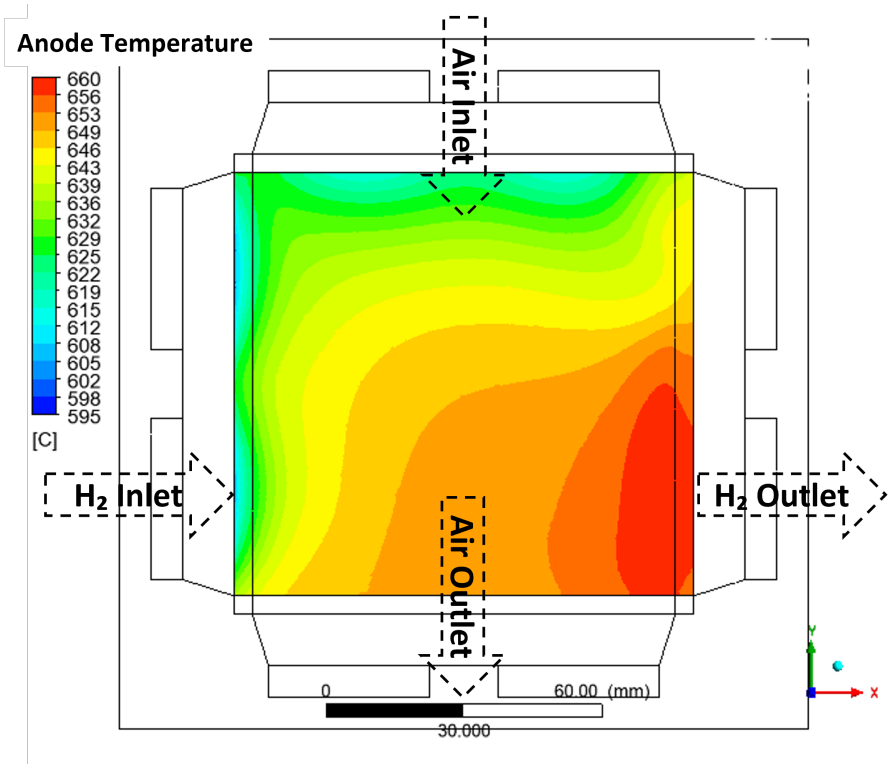

Figure 5.7: Anode surface temperature profile.

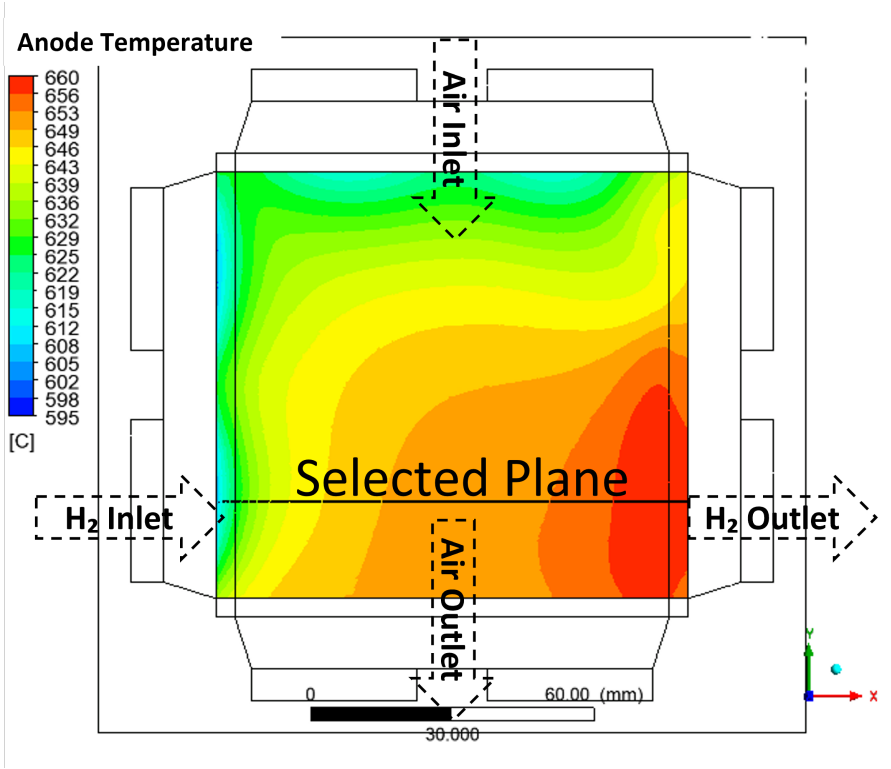

Figure 5.8: Anode surface temperature profile and the selected xz-plane for thermal gradient study.

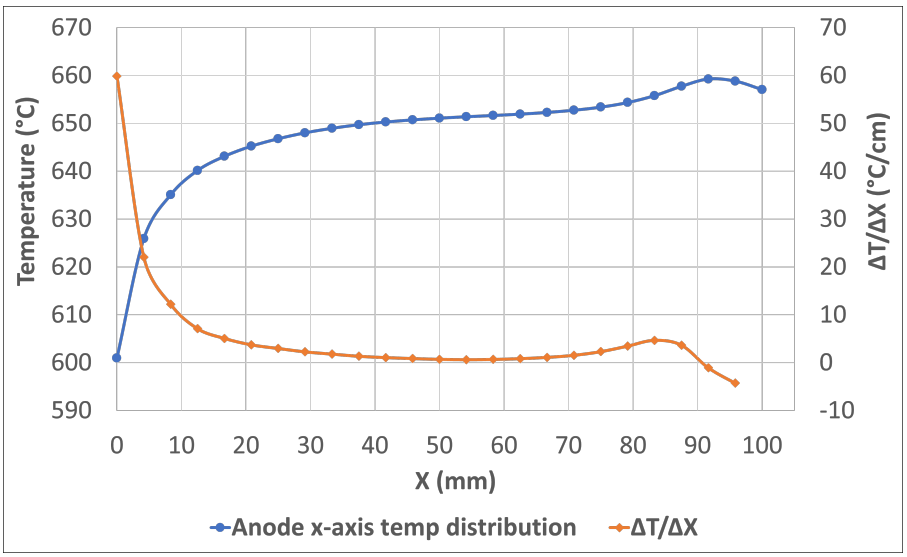

Figure 5.9: Anode surface temperature gradient across x-axis.

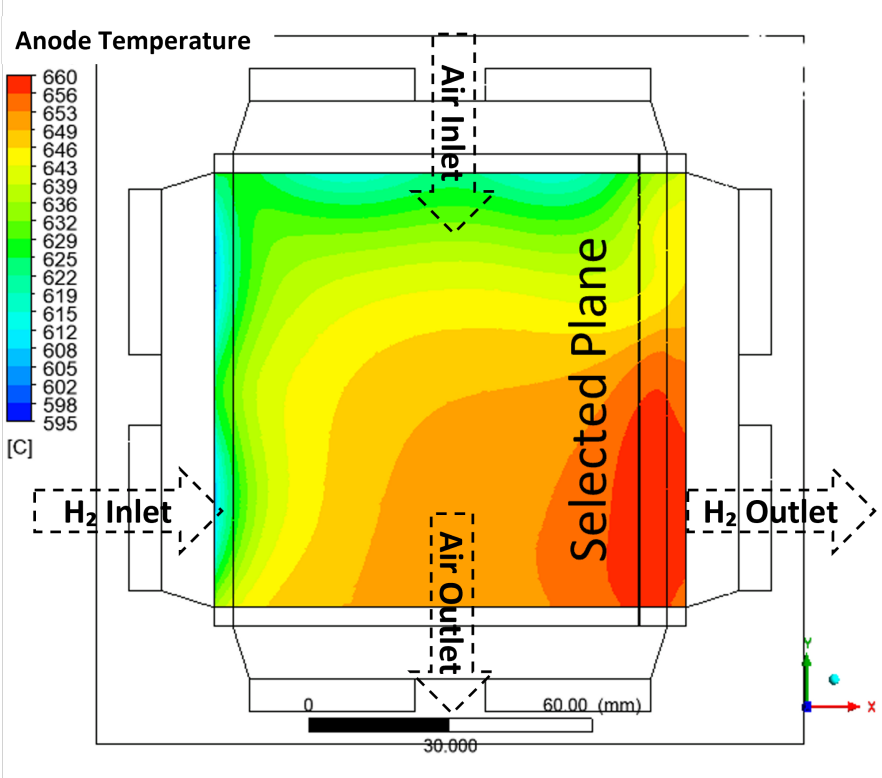

Figure 5.10: Anode surface temperature profile and the selected yz-plane for thermal gradient study.

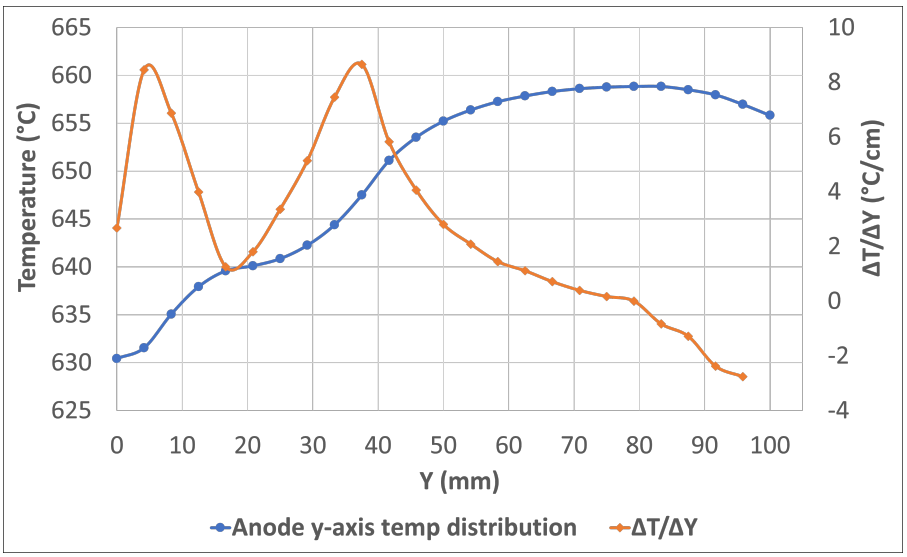

Figure 5.11: Anode surface temperature gradient across y-axis.

Cathode temperature profile and thermal gradient

Figure 5.12 shows the temperature profile on the LSC cathode surface in contact with the air channel. The LSC cathode surface's highest thermal gradient across the x-axis is 12 °C/cm, and the LSC cathode surface's average thermal gradient across the x-axis is 2.66 °C/cm, as shown in figure 5.14. While figure 5.16 shows the LSC cathode surface's highest thermal gradient across the y-axis is 8.7 °C/cm, and the LSC cathode surface's average thermal gradient across the x-axis is 3.6 °C/cm.

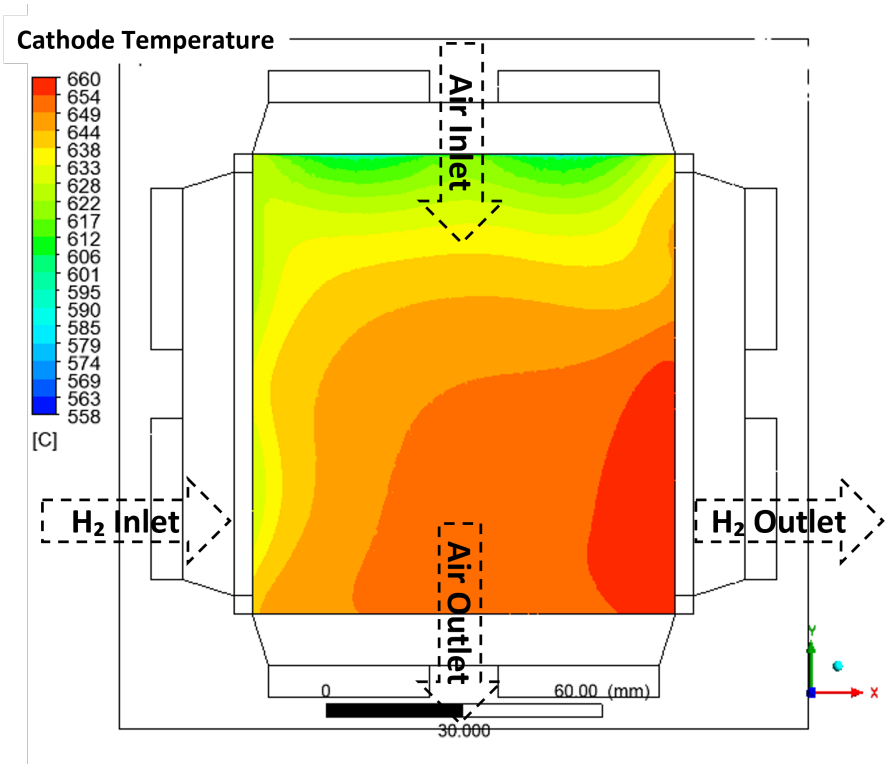

Figure 5.12: Cathode surface temperature profile.

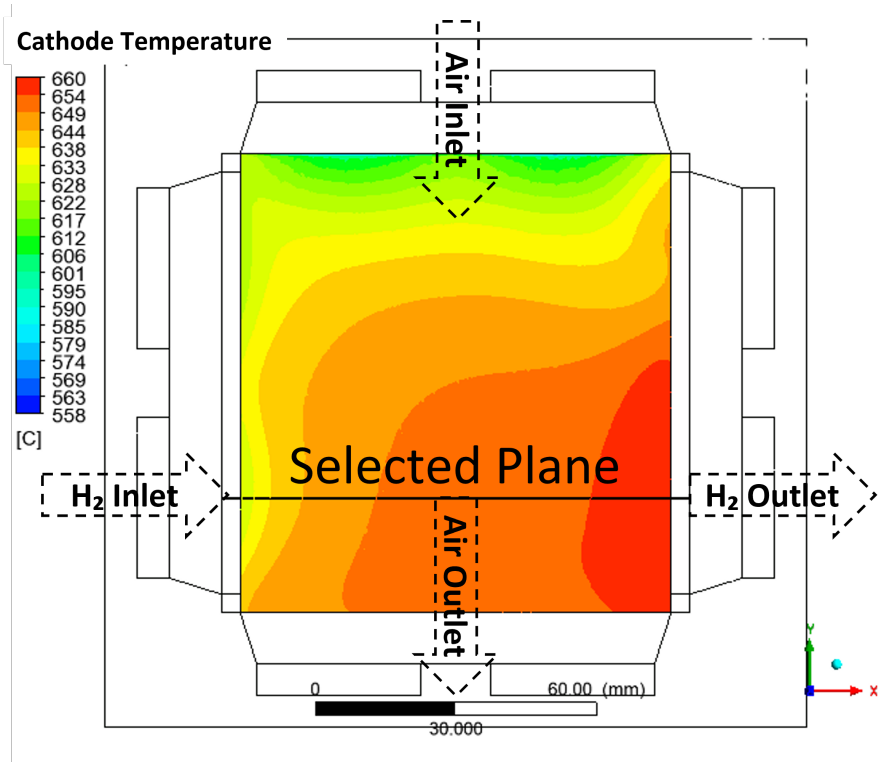

Figure 5.13: Cathode surface temperature profile and the selected xz-plane for thermal gradient study.

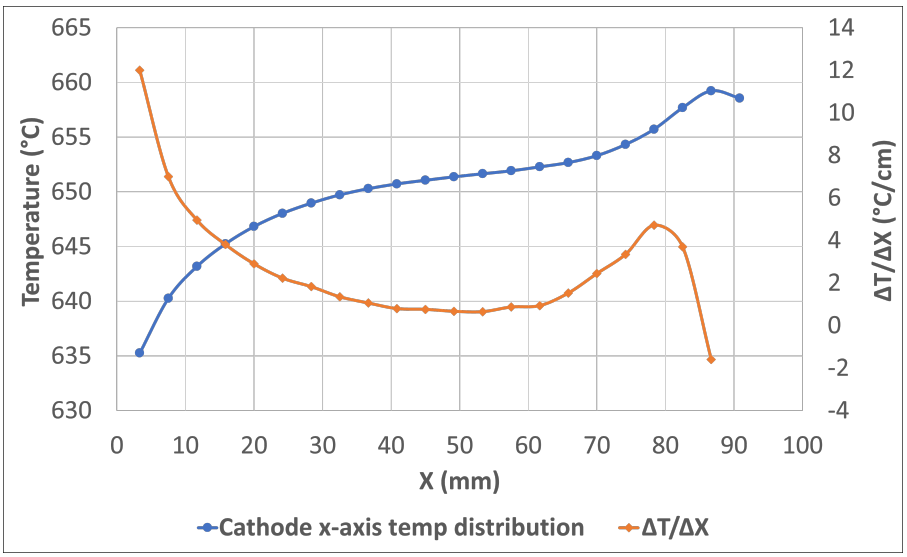

Figure 5.14: Cathode surface temperature gradient across x-axis.

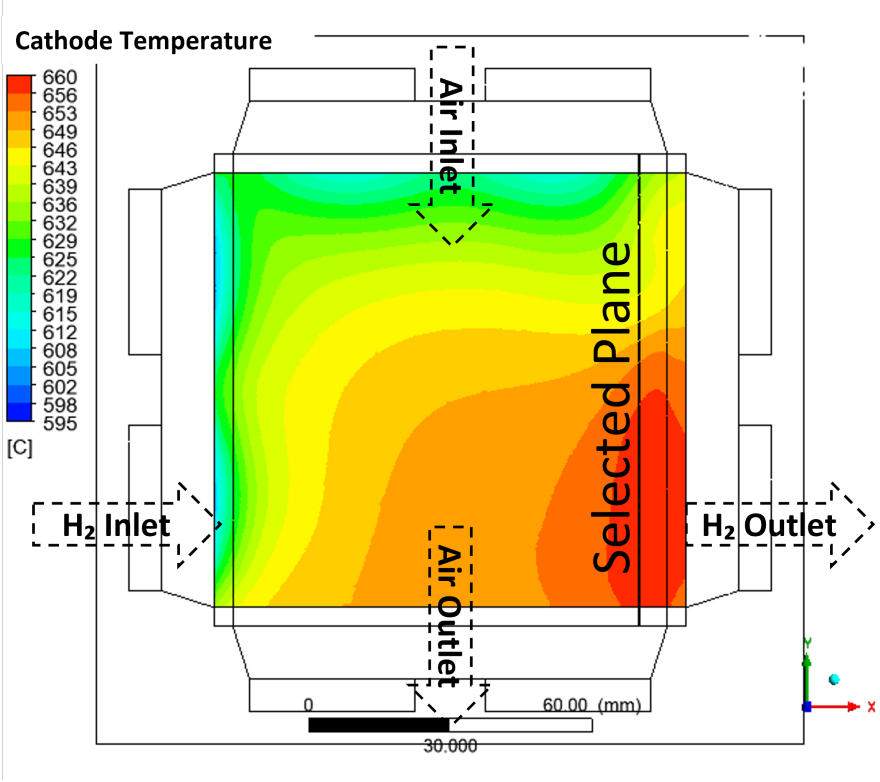

Figure 5.15: Cathode surface temperature profile and the selected yz-plane for thermal gradient study.

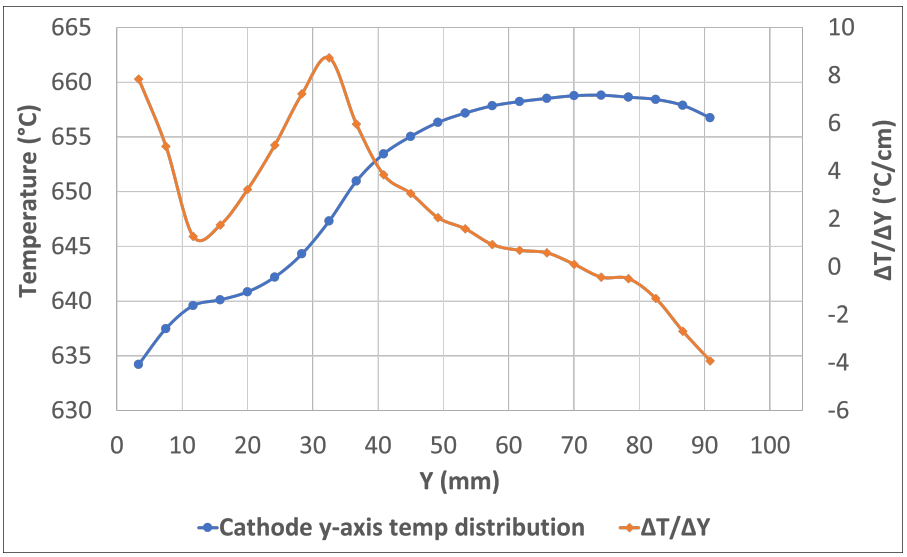

Figure 5.16: Cathode surface temperature gradient across y-axis.

Electrolyte temperature profile and thermal gradient

The YSZ electrolyte temperature distribution and thermal gradient were studied at two different YSZ electrolyte surfaces: the first surface is in contact with the anode layer, and the other surface is in contact with the cathode layer. The YSZ electrolyte surface's highest thermal gradient across the x-axis is 20 °C/cm, and the YSZ electrolyte surface's average thermal gradient across the x-axis is 3.6 °C/cm, as shown in figure 5.19. While figure 5.21 shows the YSZ electrolyte surface's highest thermal gradient across the y-axis is 9.3 °C/cm, and the YSZ electrolyte surface's average thermal gradient across the x-axis is 2.6 °C/cm.

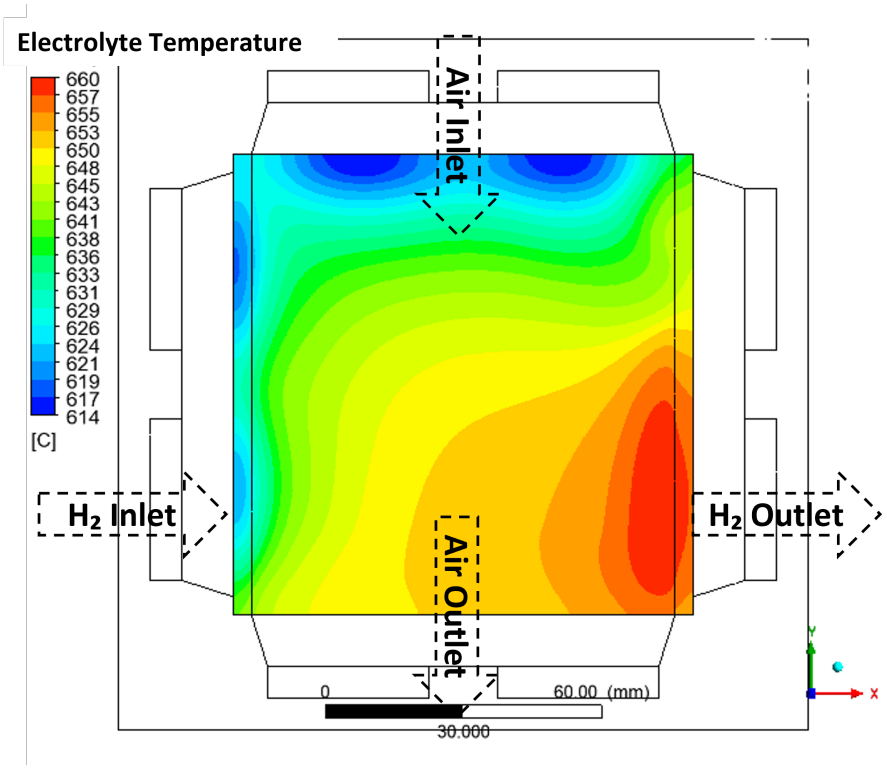

Figure 5.17: Electrolyte surface temperature profile.

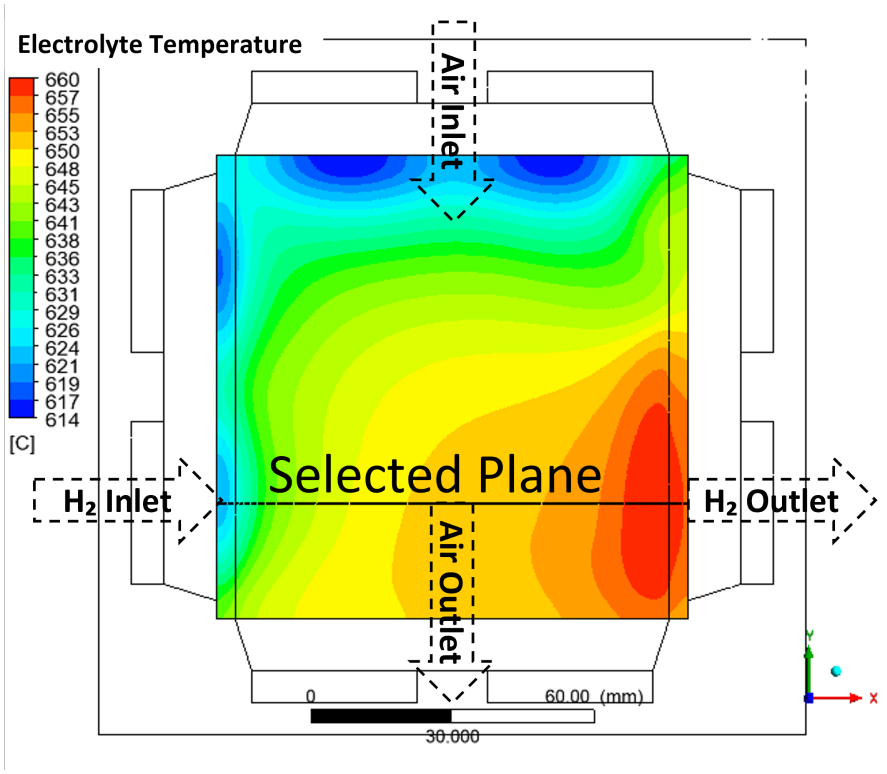

Figure 5.18: Electrolyte surface temperature profile and the selected xz-plane for thermal gradient study.

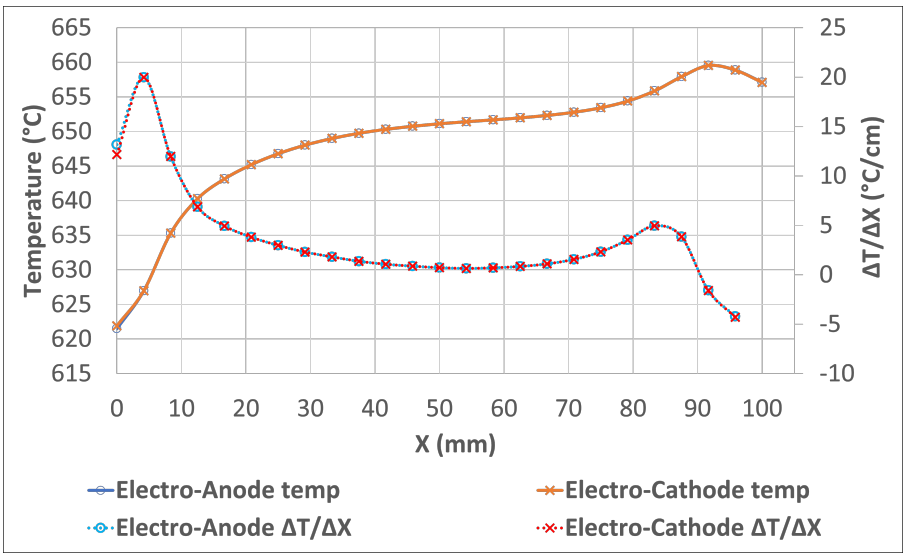

Figure 5.19: Electrolyte surface temperature gradient across x-axis.

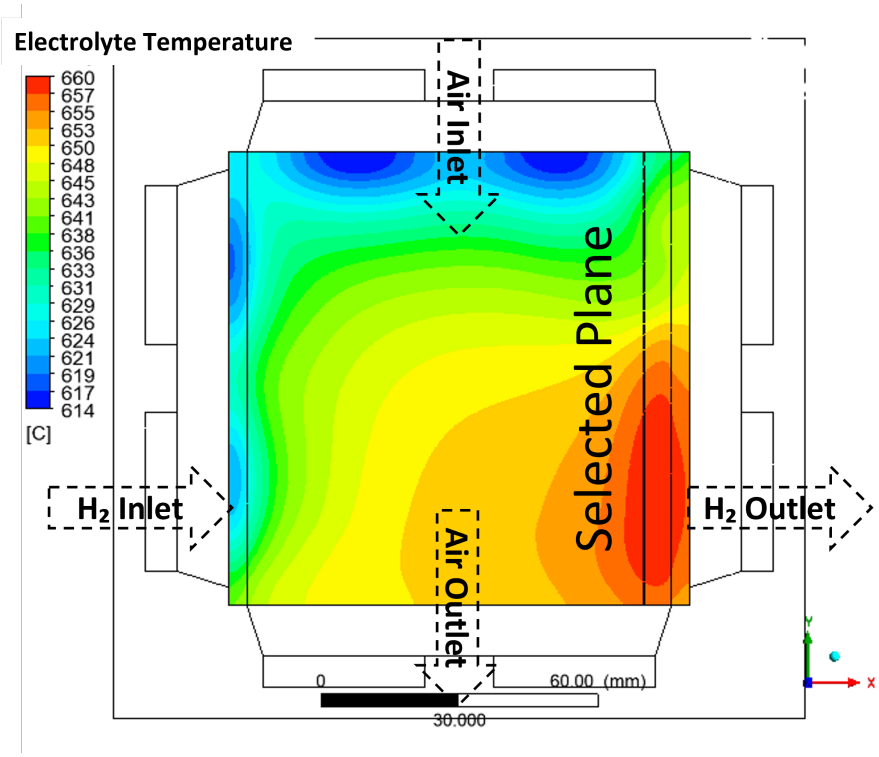

Figure 5.20: Electrolyte surface temperature profile and the selected yz-plane for thermal gradient study.

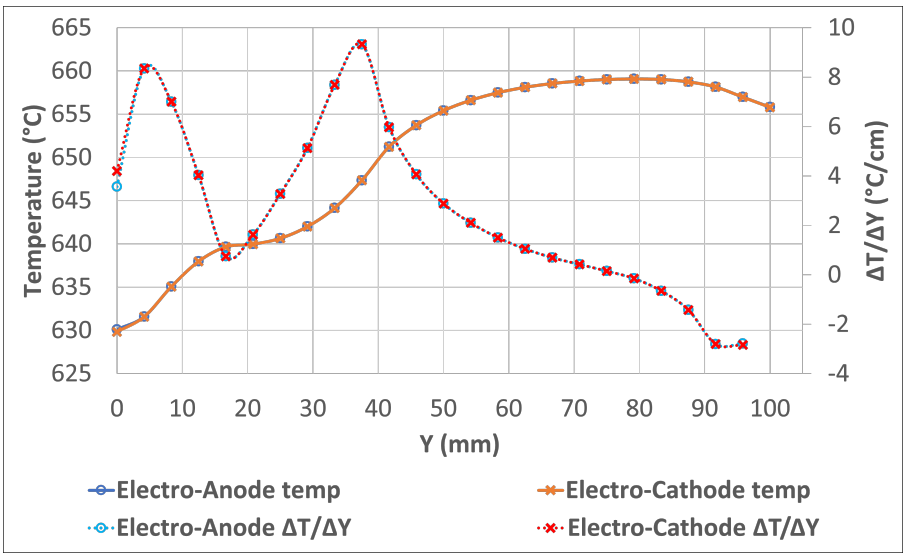

Figure 5.21: Electrolyte surface temperature gradient across y-axis.

Summary of the temperature profiles and thermal gradients

Table 5.5 summarises the values of the maximum and average thermal gradient at the surface of each layer. Because hydrogen flows across the cell parallel to the x-axis and in contact with the anode surface the results show the highest maximum thermal gradient was achieved at the anode surface across x-axis (59.9 °C/cm), while the air flows across the cell parallel to the y-axis and in contact with the cathode surface the results show the highest maximum thermal gradient was achieved at the cathode surface across y-axis (8.7 °C/cm). The temperature profiles shown in all three layers indicate that the coldest spot is identified at the north-west corner of the cell. The main reason for that is the closeness of this region to the hydrogen and air inlets, where the gases enter the cell at a temperature of 100 °C while the overall temperature within the cell reaches 650 °C. On the other hand, the hottest spot is located at the south-east corner of the cell because the two gases are heated across the cell reached to the maximum temperature before leaving the cell which significantly increase the reaction rate at this spot.

Because each layer of the cell has a different thermal expansion ratio and because the non-uniform temperature distribution can cause deformations or cracks in the components of the cell, it is essential to understand the thermal gradient of the anode, cathode, and electrolyte layers. can still have a substantial impact on cell performance for two primary reasons. Firstly, it can lead to insufficient electrical current contact, thereby limiting the electrical current flow.

Secondly, deformation can result in sealing issues, which in turn reduce the flow rate of reactions and may pose safety risks to the entire system. Additionally, studying the ceramic electrolyte layer thermal gradient is more challenging and requires extra attention because it is the weakest point of the anode support SOFC due to its very thin thickness compared to the other layers [58].

Table 5.5: Planar cell thermal gradient values at each layer.

Zone	Maximum	Average	Unit
Anode surface x-axis	59.9*	5.6	°C/cm
Anode surface y-axis	8.6	2.5	°C/cm
Cathode surface x-axis	12.0*	2.6	°C/cm
Cathode surface y-axis	8.7	2.2	°C/cm
Electrolyte surfaces x-axis	20.0*	3.6	°C/cm
Electrolyte surfaces y-axis	9.3	2.6	°C/cm

*The value is higher than the maximum allowable thermal gradient (10 °C/cm)

5.3.2 Planar cell fuel and oxidant consumption

Figure 5.22 shows how the hydrogen is consumed through the cell fuel channel. The used fuel for this experiment is dry hydrogen without any water vapour added, so the hydrogen mass fraction at the fuel inlet is about 100 %. From studying the hydrogen consumption rate, the average hydrogen mass fraction at the outlet ports is equal to 60 % with a fuel utilization factor of 0.4. The hydrogen mass fraction is scaled within the range of 0.45 to 1 in order to enhance the visual representation of the amount of how hydrogen is utilized.

While the oxygen inlet mass fraction is 21 % and the outlet fraction is 15 % with 0.28 oxygen utilization factor. The oxygen mass fraction is scaled within the range of 0.09 to 0.21 to improve the visual representation of the utilization of oxygen.

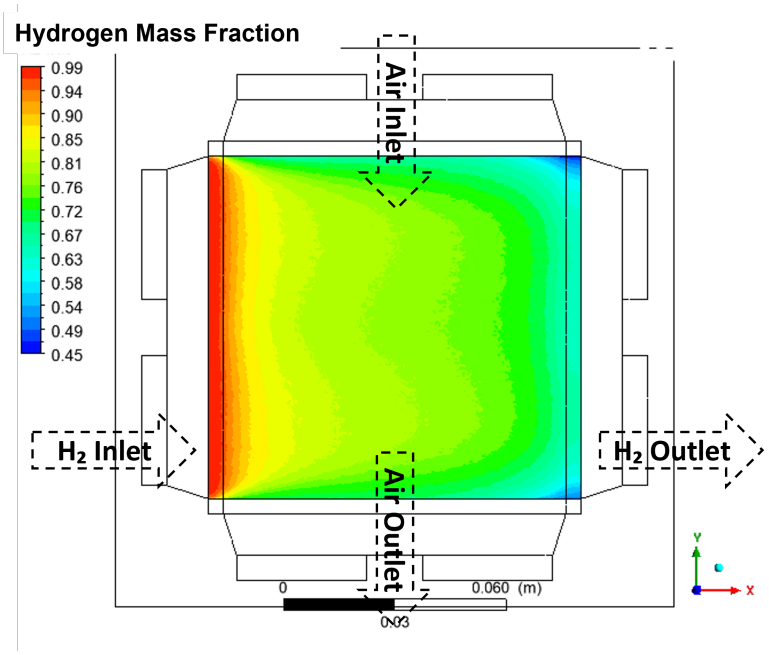

Figure 5.22: Hydrogen mass fraction across the planar cell fuel channel.

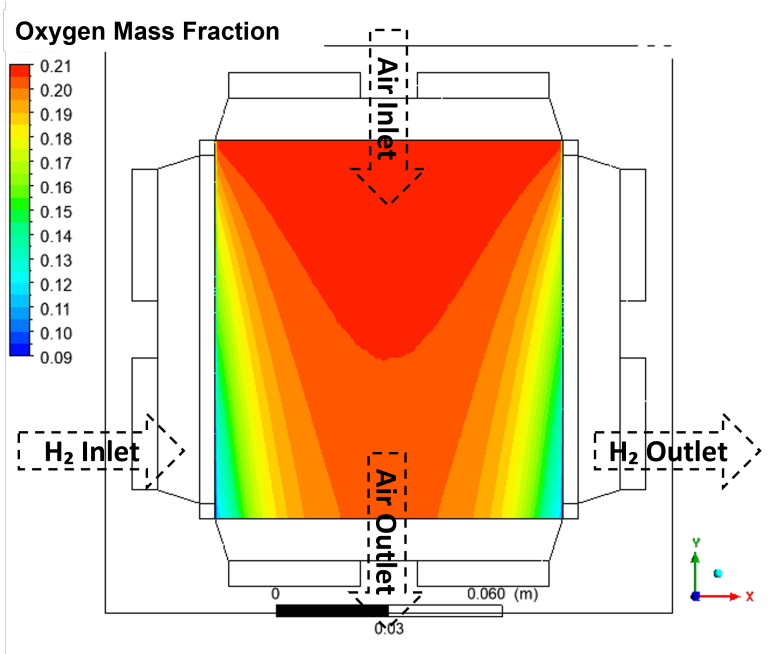

Figure 5.23: Oxygen mass fraction across the planar cell air channel.

Chapter 6

Parametric and thermal gradient analysis

The parametric analysis is a very important step in studying the effect of some crucial parameters that have a significant effect on the cell's performance. The parametric analysis represents a reliable approach to optimize the operational and structural parameters of the SOFC, increasing the confidence in the design phase, and improving the fabrication phase to maximize cell performance and reduce the cell degradation rate. In this chapter, the effects of three structural parameters on cell performance were investigated: anode porosity, anode thickness, and electrolyte thickness. The study of these three structural parameters was carried out because to their significant impact on optimizing cell design and improving cell performance. Following that, the results of this parametric analysis were utilized to predict the full capability of Elcogen planar cell performance, using the optimal design parameters and the suggested operating conditions as specified by the cell manufacturer. At the end of this chapter, the relationship between the operating conditions and the thermal gradient of the planar cell was investigated to determine the shape of the thermal gradient across the cell under different hydrogen and air flow rates, as well as varying gases inlet temperatures.

6.1 Effect of anode porosity

Figure 6.1 illustrates the effect of changing the anode porosity on the tubular cell performance, while Figure 6.2 illustrates the effect of changing the anode porosity on the planar cell performance. The figures show the highest cell performance was at porosity equal to 0.4. Although

reducing the porosity to 0.2 has higher performance at low current density, the performance sharply decreases at high current density regions. The main reason for that is that reducing the porosity increases the triple phase boundary (TPB) length, which significantly reduces the activation overpotential and explains why the cell has higher performance at low current density regions, but it also decreases the hydrogen diffusivity through the anode layer. This limits the mass transfer efficiency and increases the concentration overpotential, leading to lower cell performance at high current density regions.

On the other hand, although increasing the anode porosity to 0.6 improves the hydrogen diffusion rate, the cell performance sharply drops because the TPB is reduced, leading to a significant increase in the activation overpotential. A similar trend was observed in other studies [40, 41, 59].

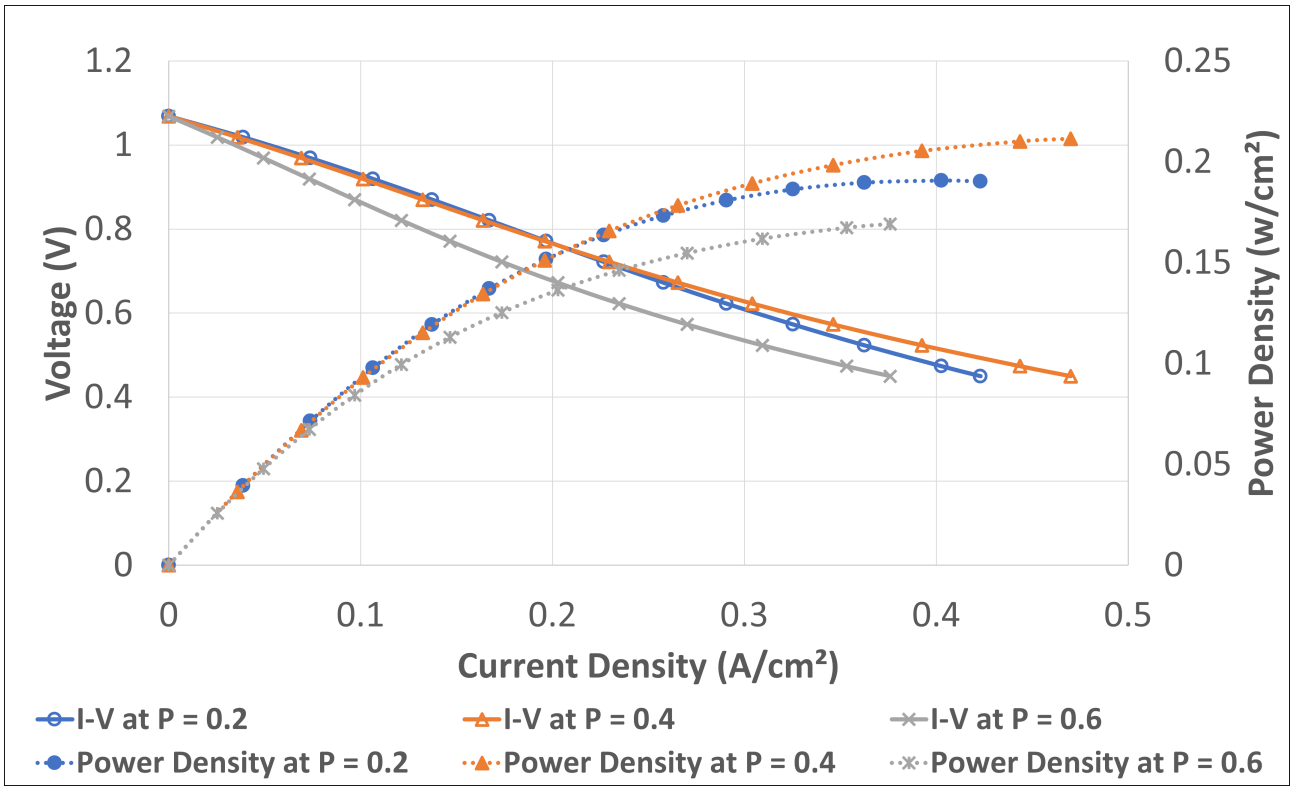

Figure 6.1: The effect of anode porosity (P) on the tubular SOFC.

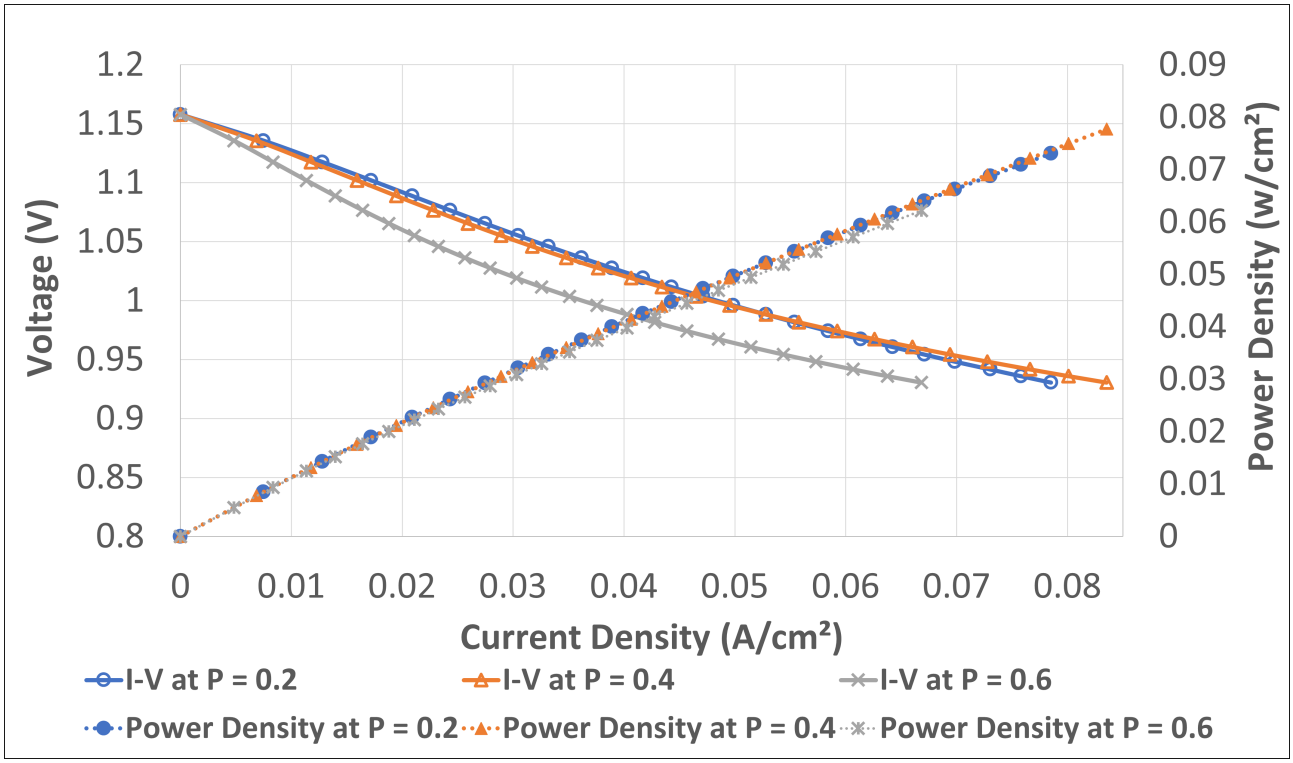

Figure 6.2: The effect of anode porosity (P) on the planar SOFC.

6.2 Effect of anode thickness

This section shows the effect of increasing the anode layer thickness on the planar and tubular cells performance. Figures 6.3 and 6.4 illustrate how varying anode layer thickness influences cell performance. Concentration overpotential and ohmic overpotential are affected by changing the anode layer thickness. Because a thicker anode restricts gas diffusion, which decreases the partial pressure of hydrogen at the TPB while at the same time raising the partial pressure of water vapour at the TPB. A thicker anode layer causes a major limitation of gas mass transfer and also an increase in the concentration overpotential [40, 41, 60]. In terms of the anode layer thickness effect on the ohmic overpotential, a thicker anode exhibits a minor increase in the ohmic overpotential.

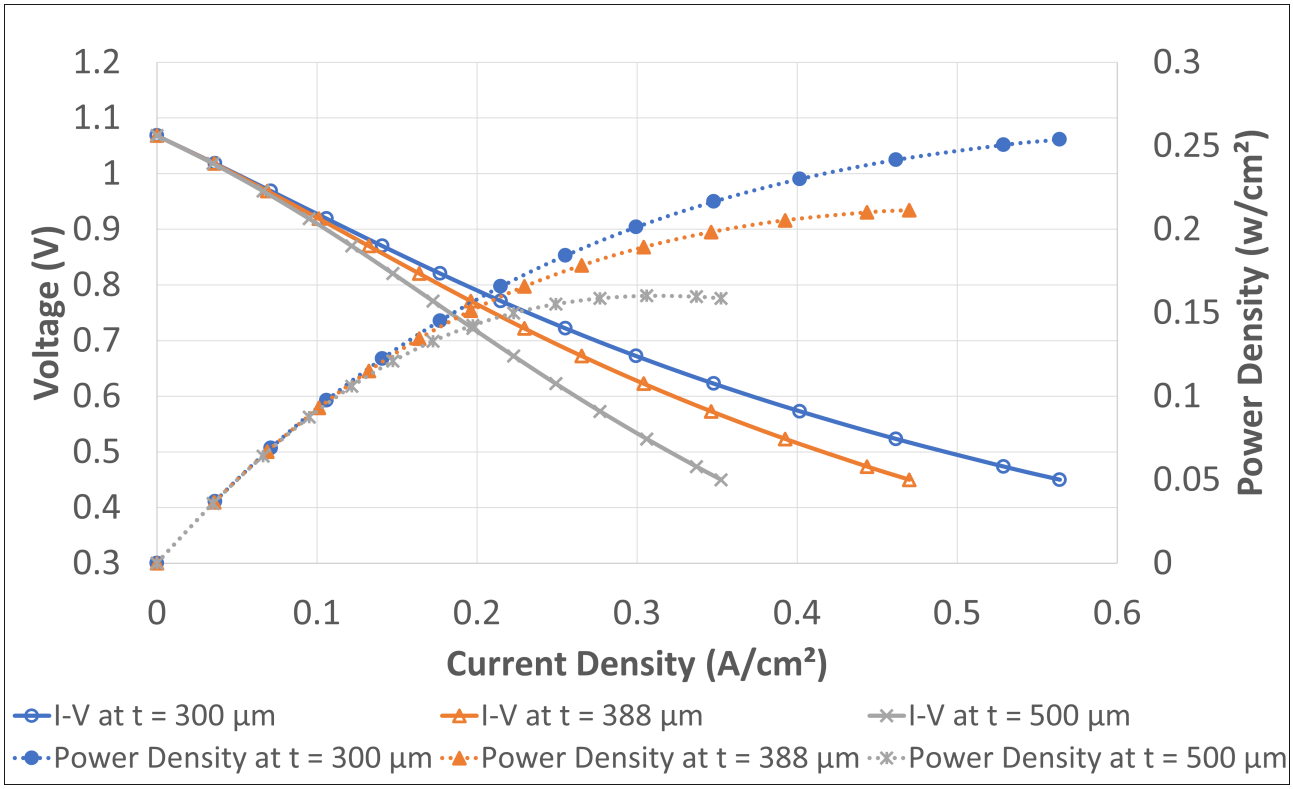

Figure 6.3: The effect of anode thickness (t) on the tubular SOFC.

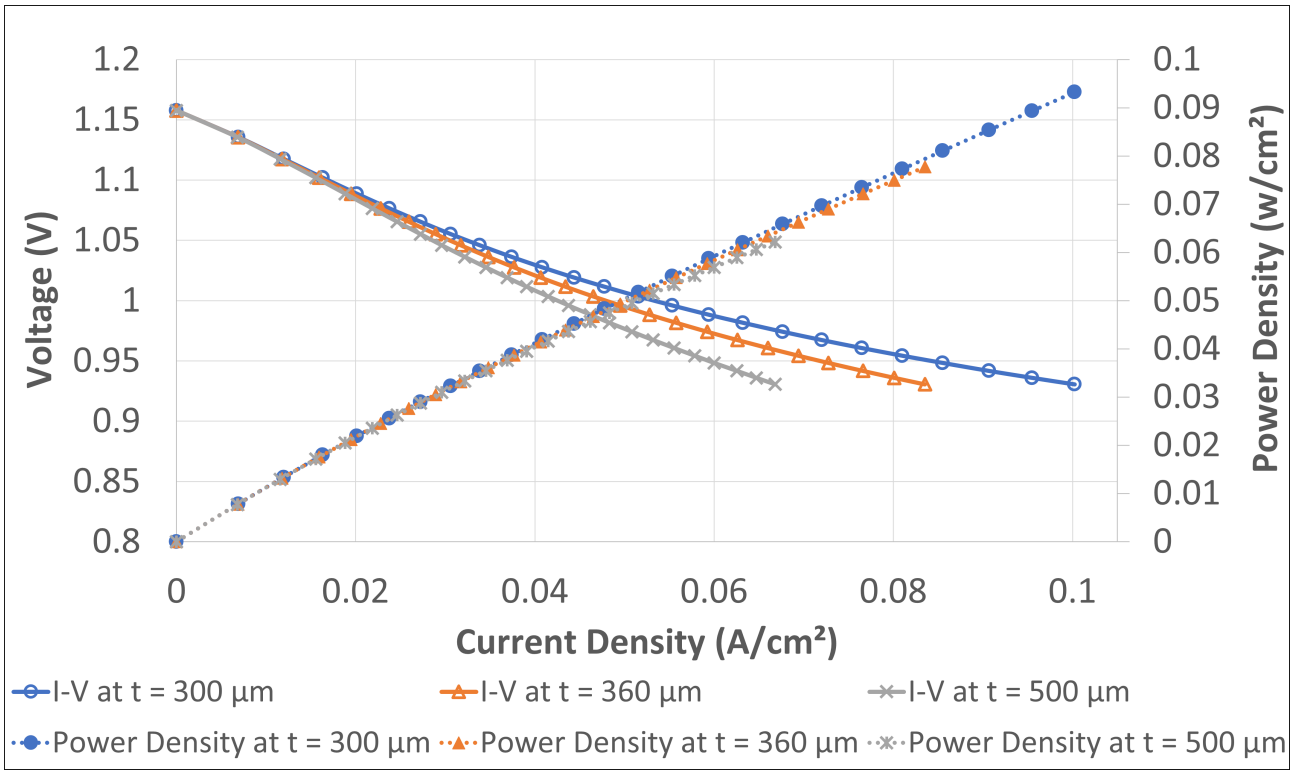

Figure 6.4: The effect of anode thickness (t) on the planar SOFC.

6.3 Effect of electrolyte thickness

Although lowering the electrolyte thickness enhances the performance of the cell and lowers the cost of cell fabrication, an excessive decrease in the electrolyte thickness may degrade the fuel cell's stability and lifespan. Figures 6.5 and 6.6 show how the tubular and planar cells' performance significantly increased while decreasing the electrolyte thickness because the thinner the electrolyte layer, the lower the ohmic overpotential [40, 41, 61]. This is the primary benefit of anode-support SOFCs over other supporting component designs, such as electrolyte-support or cathode-support, because anode-support SOFCs have a thin electrolyte with a relatively lower ohmic overpotential. While the electrolyte electrical conductivity proportionally increases with increasing the operating temperature to achieve a lower ohmic overpotential, anode-support SOFCs can run at as low an operating temperature as 500 °C and still have an acceptable ohmic overpotential, which plays a great role in decreasing the SOFC's degradation rate.

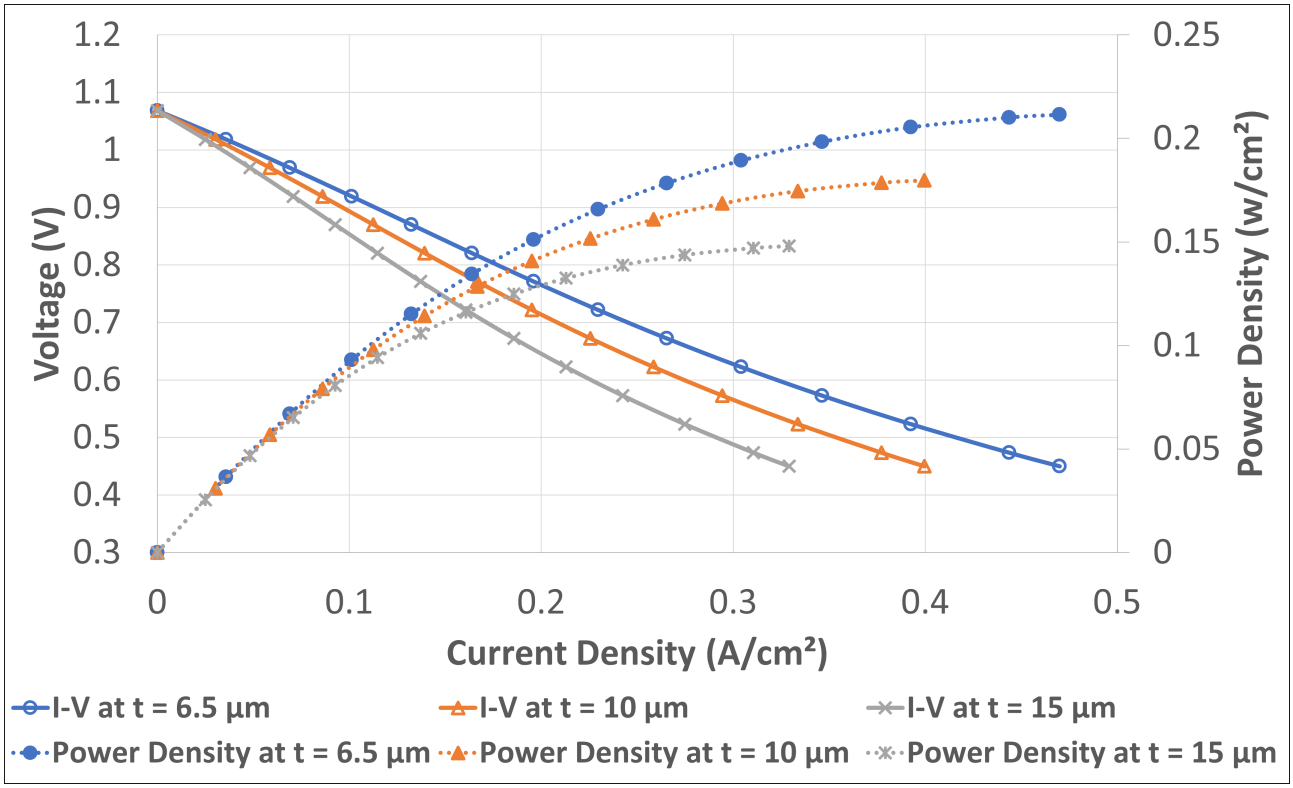

Figure 6.5: The effect of electrolyte thickness (t) on the tubular SOFC.

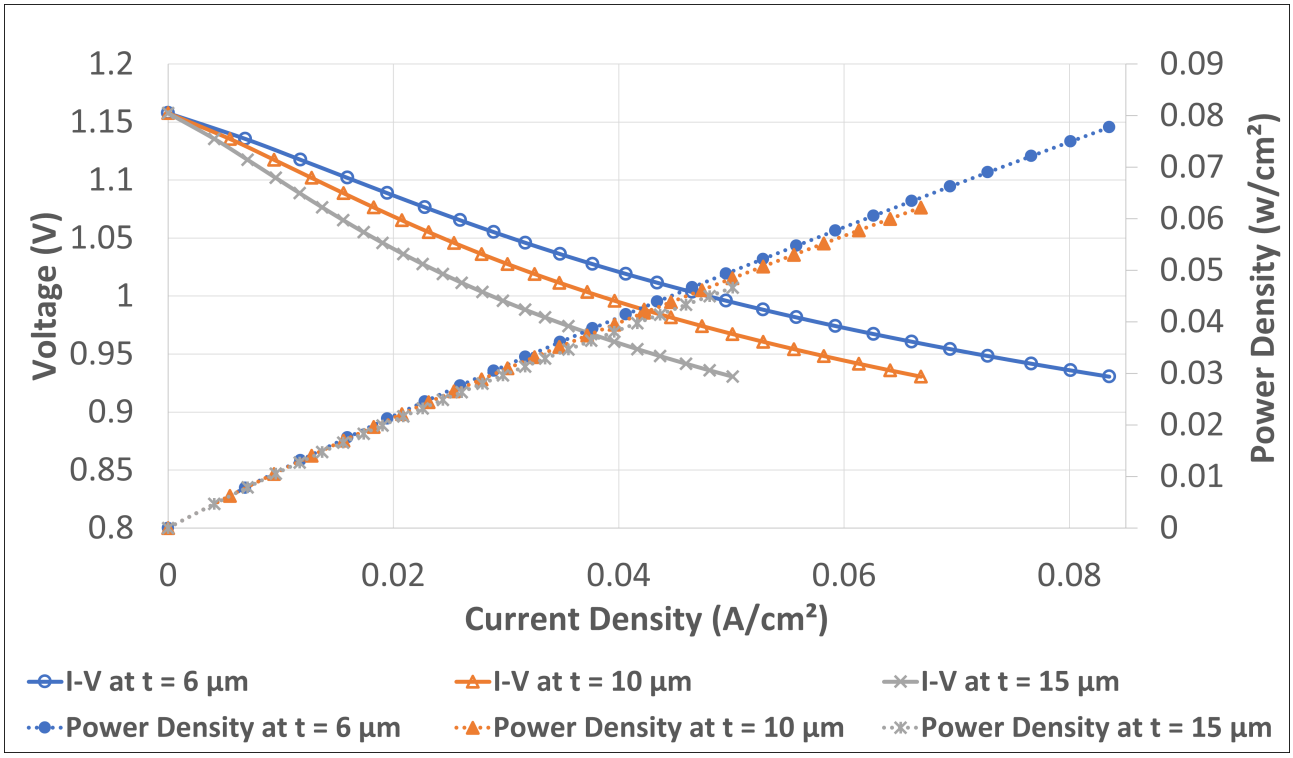

Figure 6.6: The effect of electrolyte thickness (t) on the planar SOFC.

6.4 Recommended operating conditions to maximize the plant cell's performance

Due to the limitations in the flow rates of the current experimental setup, which allows only a maximum flow rate of 400 SCCM for fuel and air, the CFD model is used to predict the required flow rates of hydrogen and air to get the full potential of the planar cell at 650 °C. Figure 6.7 illustrates the predicted I-V curve and power density curve at air flow rate 2000 SCCM and fuel flow rate 1000 SCCM, which is samilar to the flow rates listed in the cell manufacturer data sheet. The results show that the studied cell could achieve a power density as high as 0.725 w/cm^2 at a current density equal to 1 A/cm^2.

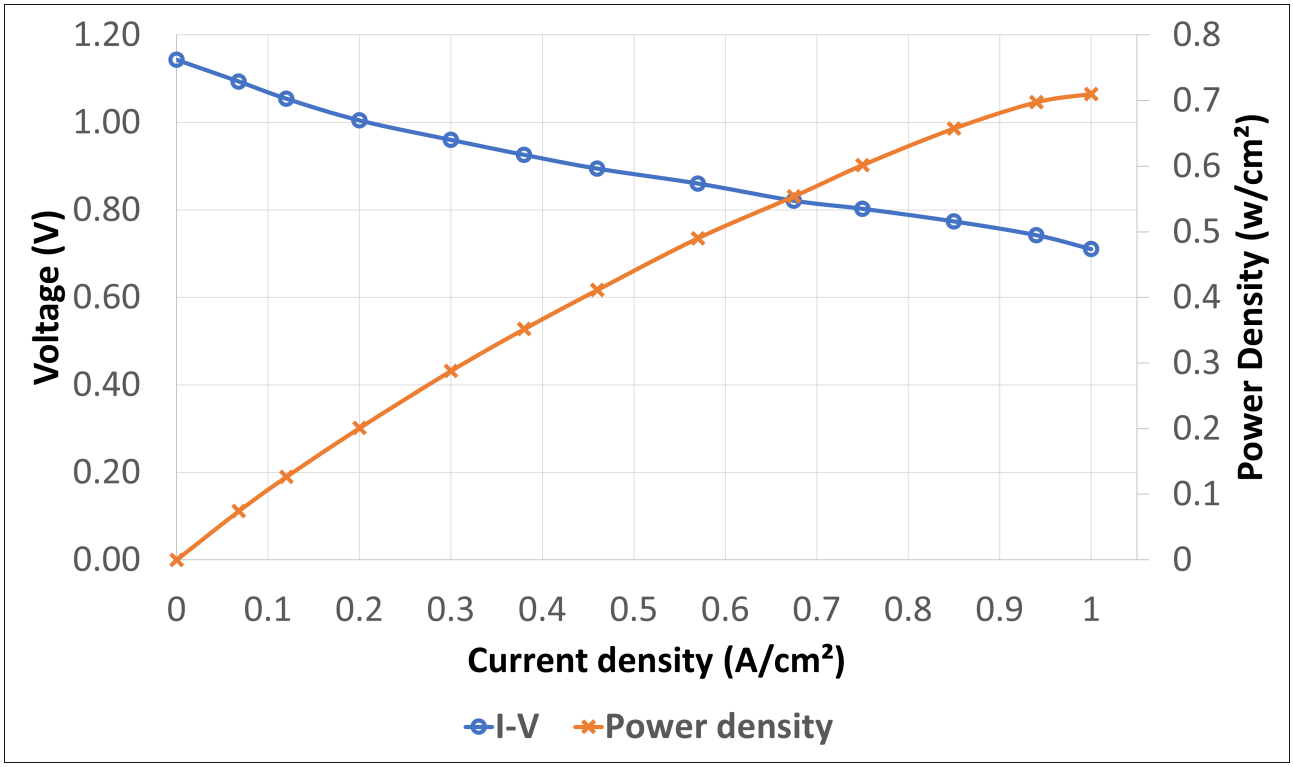

Figure 6.7: The planar cell potential performance at the recommended operating conditions at $\dot{v}_a =$ 2000 SCCM and $\dot{v}_f =$ 1000 SCCM.

6.5 Effect of operating conditions on the planar cell temperature gradients

In this section, the planar cell thermal gradient and temperature distribution have been investigated at three different operating conditions to study the effect of operating conditions on the cell thermal gradient, which can sharply influence the cell degradation rate. In an SOFC, the thermal gradient refers to the temperature difference across the cell. The temperature differential between the fuel, oxidant gases, and the cell temperature, as well as the heat generated through the electrochemical reactions, are the causes of the thermal gradient in SOFCs.

Studying the cell's thermal gradient is crucial for many reasons: the higher the temperature gradients across the cell, the higher the thermal stresses, which can sharply reduce the cell's durability and lifetime. Moreover, a non-uniform temperature distribution can also cause deviations in the electrochemical reactions rates, which can impact the performance and efficiency.

The CFD analysis is used to study the planar cell's thermal gradient and temperature dis-

tribution at three operating conditions: the first one is the healthy condition for the cell with high inlet fuel and oxidant gases temperature which would cause a low thermal gradient; and the second is the condition where inlet fuel and oxidant gases temperature and flow rates are as in the planar cell experiment discussed in Chapter two. Finally, the unhealthy condition is studied where the inlet fuel and oxidant gases temperature is equal to the ambient temperature which would cause a high thermal gradient. The comparison between the anode, cathode, and electrolyte surfaces temperature distribution and thermal gradients is illustrated in Figures 6.8, 6.9, 6.10, 6.11, 6.12, and 6.13. Table 6.1 shows the three studied operating conditions parameters:

Table 6.1: Various operating conditions of the planar cell for thermal gradient study.

Parameter	**Healthy**	**Experiment**	**Unhealthy**
Hydrogen flow rate	1000 SCCM	400 SCCM	1000 SCCM
Air flow rate	2000 SCCM	400 SCCM	2000 SCCM
Hydrogen inlet temperature	650 °C	100 °C	25 °C
Air inlet temperature	650 °C	100 °C	25 °C
Fuel flow Species (mass fraction)	100% H_2, 0%H_2O	100% H_2, 0%H_2O	100% H_2, 0%H_2O
Air flow Species (mass fraction)	79% N_2, 21%O_2	79% N_2, 21%O_2	79% N_2, 21%O_2
Voltage	1 V	1 V	1 V
Current density	0.201 A/cm^2	0.046 A/cm^2	0.183 A/cm^2

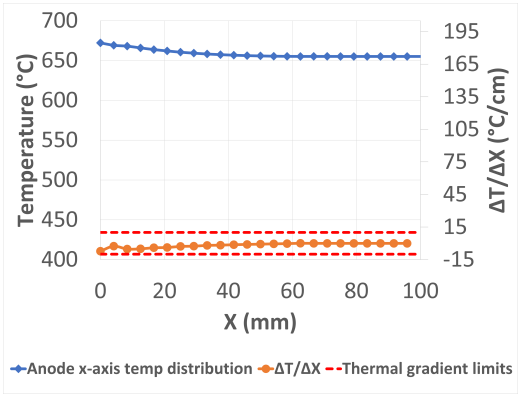

(a) Healthy operating conditions

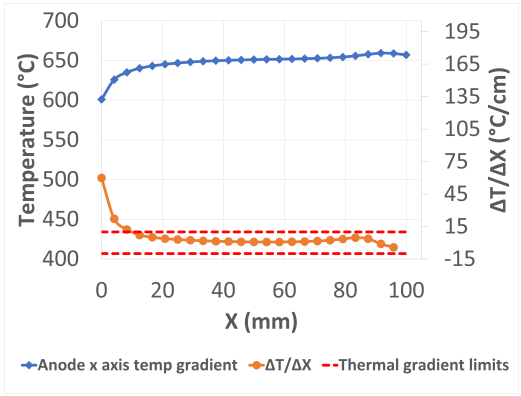

(b) Experiment operating conditions

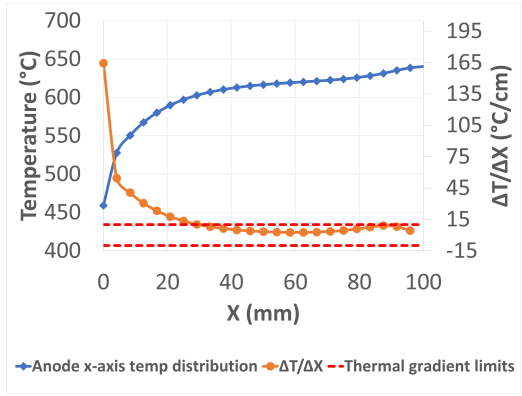

(c) Unhealthy operating conditions

Figure 6.8: Anode surface temperature gradient at the x-axis for various operating conditions listed in Table 6.1

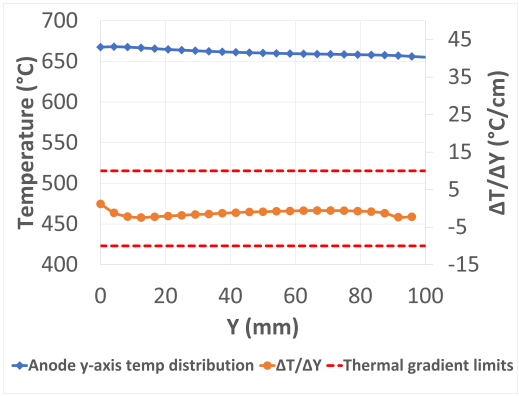

(a) Healthy operating conditions

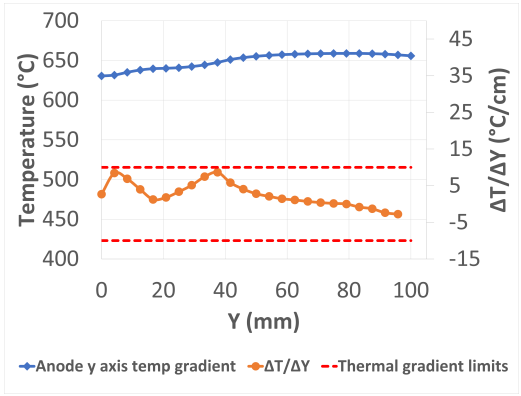

(b) Experiment operating conditions

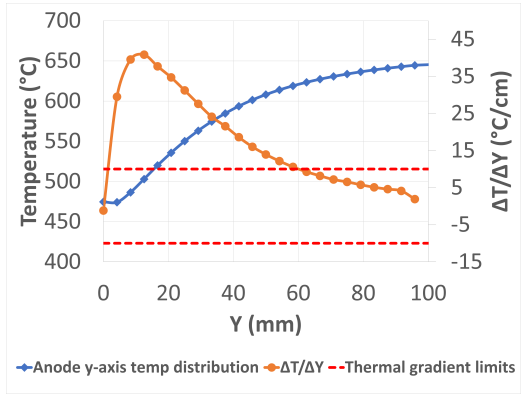

(c) Unhealthy operating conditions

Figure 6.9: Anode surface temperature gradient at the y-axis for various operating conditions listed in Table 6.1

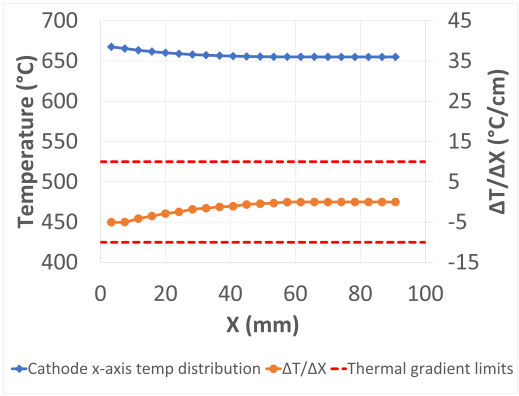

(a) Healthy operating conditions

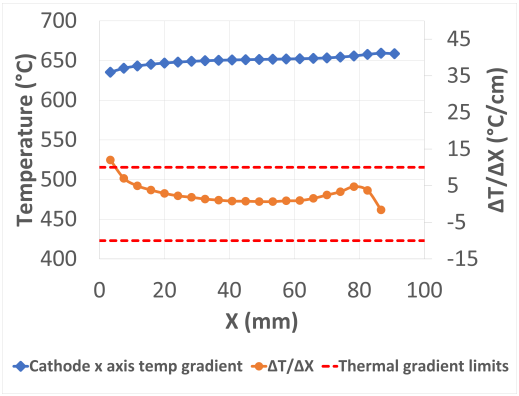

(b) Experiment operating conditions

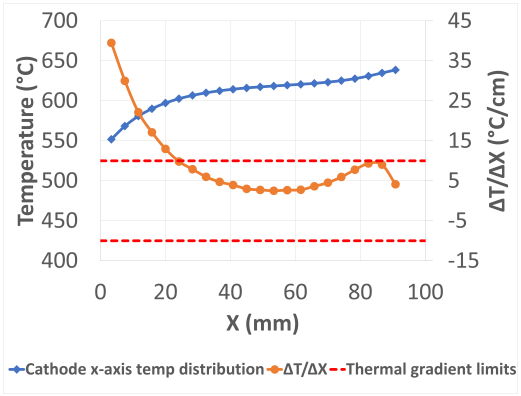

(c) Unhealthy operating conditions

Figure 6.10: Cathode surface temperature gradient at the x-axis for various operating conditions listed in Table 6.1

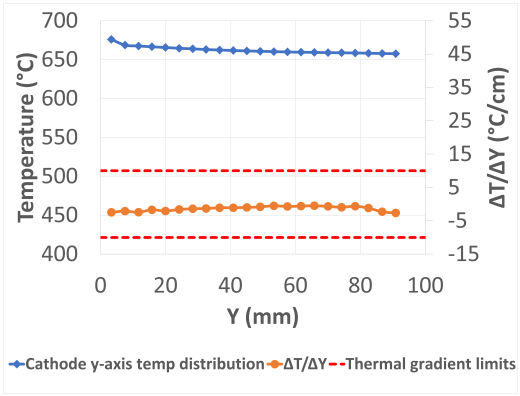

(a) Healthy operating conditions

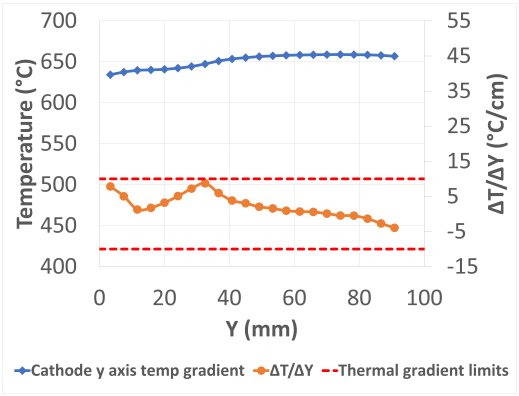

(b) Experiment operating conditions

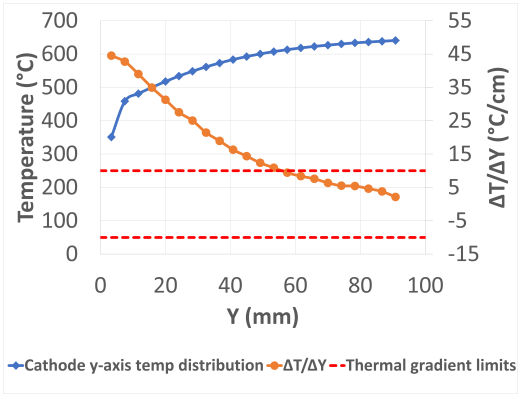

(c) Unhealthy operating conditions

Figure 6.11: Cathode surface temperature gradient at the y-axis for various operating conditions listed in Table 6.1

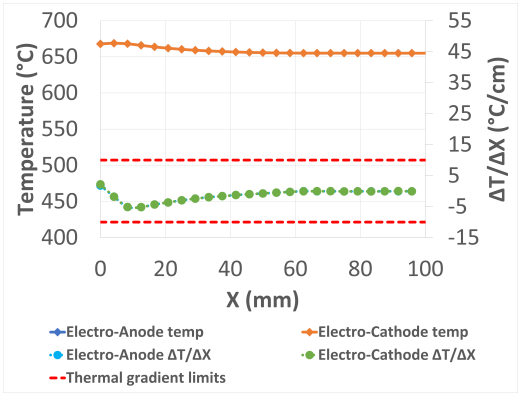

(a) Healthy operating conditions

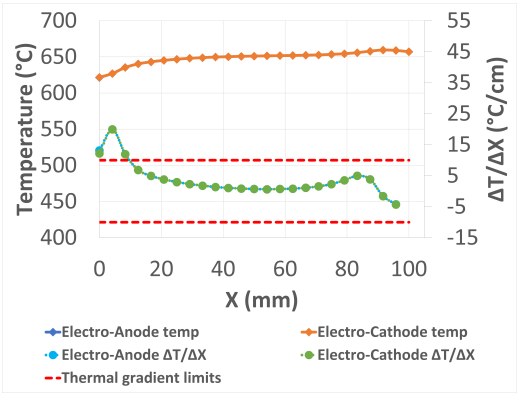

(b) Experiment operating conditions

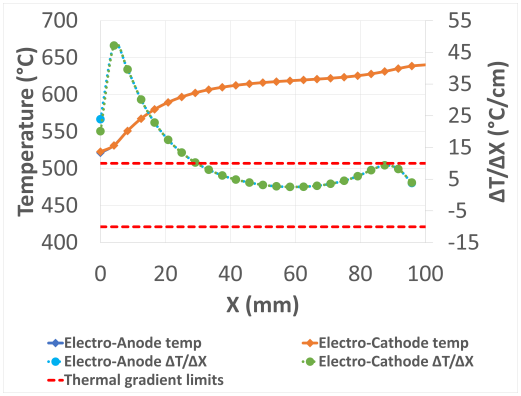

(c) Unhealthy operating conditions

Figure 6.12: Electrolyte surfaces temperature gradient at the x-axis for various operating conditions listed in Table 6.1

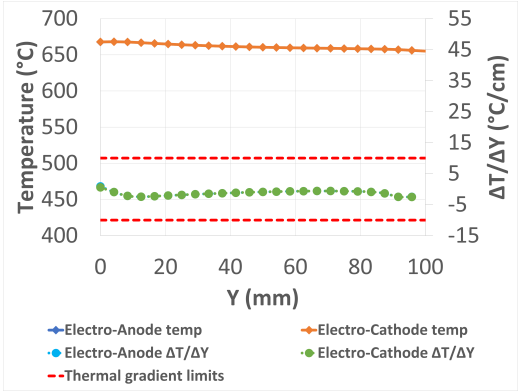

(a) Healthy operating conditions

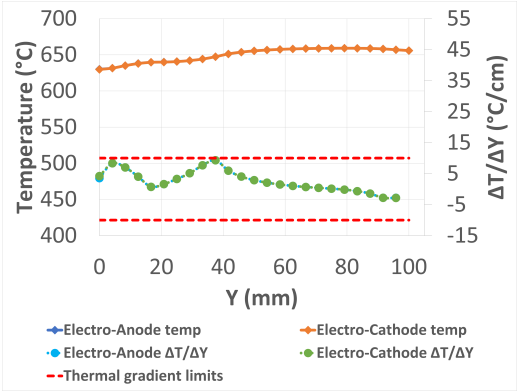

(b) Experiment operating conditions

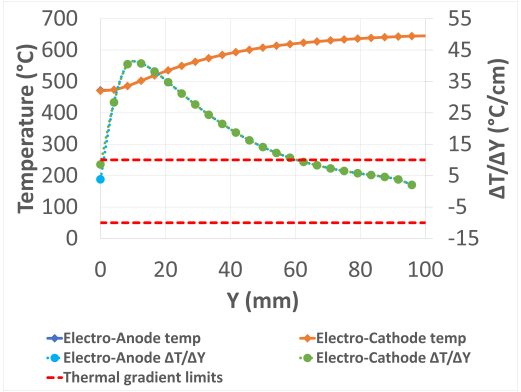

(c) Unhealthy operating conditions

Figure 6.13: Electrolyte surfaces temperature gradient at the y-axis for various operating conditions listed in Table 6.1

As shown in the previous figures, three CFD models results were presented to show the temperature distribution and thermal gradients of three cases: healthy operating conditions, experiment operating conditions, and unhealthy operating conditions. The temperature value in degrees Celsius is shown by the left y-axis, while the thermal gradient value in degrees Celsius per centimetre is represented by the right y-axis. The two dashed horizontal red lines represent the high and the low limits of the thermal gradient (±10 °C/cm). Any temperature gradient value falling within the range defined by these two lines is considered to be an acceptable thermal gradient value. Deviating from this range may result in cell failure.

The results of the healthy operating conditions show the lowest temperature gradients for the three SOFC layers, anode, cathode, and electrolyte, and the temperature distribution across the cell at the healthy operating conditions is more uniform than the experiment operating conditions and the unhealthy operating conditions. On the other hand, the highest temperature gradient results for the three SOFC layers were found while applying the unhealthy operating conditions; the temperature difference across the cell could reach up to 200 °C, while all the average thermal gradients for the three layers at the x and y axes are higher than the maximum allowable temperature gradient for SOFCs (10 °C/cm).

Table 6.2 represents the average and maximum thermal gradient at the three aforementioned operating conditions 6.1 for anode, cathode, and electrolyte surfaces. The results show the healthy operating condition achieved the highest current equal to 0.201 A at a voltage equal to 1 V and the lowest thermal gradient at the three cell components, anode, cathode, and electrolyte. The highest thermal gradients were observed under the unhealthy conditions, leading to anode, cathode, and electrolyte average thermal gradients equal to 18.1, 19.8, and 17.3 °C/cm, respectively.

Although the healthy and unhealthy conditions have the same fuel and oxidant flow rates, the generated current at the same voltage (1 V) is higher at the healthy condition than the unhealthy condition, and the main reason for that is that the inlet temperature of gases at the unhealthy condition is the ambient temperature (25 °C), which is much lower than the cell temperature (650 °C). Leading to a high thermal gradient and non-uniform temperature distribution across the cell, which reduces the cell's performance. For example, the output

power density of the healthy operating conditions is 10% higher than the output power density of the unhealthy operating conditions.

This study demonstrated the importance of preheating the fuel and air before entering the fuel cell to minimize the non-uniform temperature distribution which could significantly reduce the cell performance and increasing the cell thermal stress causing mechanical deformation and even cell breakdown. The results shows using hydrogen and air at the the ambient temperature (25 °C) with flow rates equal to 1000 SCCM and 2000 SCCM, respectively, could cause a catastrophic failure to the cell. After running the model with various combinations of fuel and air inlet temperatures while maintaining a constant flow rate ($\dot{v}_f$ = 1000 SCCM and $\dot{v}_a$ = 2000 SCCM). The objective was to identify the minimum permissible inlet temperature for both fuel and air, in order to ensure that the thermal gradients across the cell fall within an acceptable range and are lower than the minimum allowable thermal gradient (10 °C/cm). It was found that the minimum allowable inlet temperature for both fuel and air was 550 °C.

Table 6.2: Various operating conditions of the planar cell for thermal gradient study.

Condition	**Healthy**		**Experiment**		**Unhealthy**	
Zone	Average °C/cm	Maximum °C/cm	Average °C/cm	Maximum °C/cm	Average °C/cm	Maximum °C/cm
Anode surface x-axis	1.7	7.2	5.6	59.9*	18.1*	164.3*
Anode surface y-axis	1.3	2.4	2.5	8.6	17.0*	40.8*
Cathode surface x-axis	1.3	5.1	2.6	12.0*	9.6	39.4*
Cathode surface y-axis	1.3	2.6	2.2	8.7	19.8*	64.5*
Electrolyte surfaces x-axis	1.4	5.1	3.6	20.0*	11.8*	47.1*
Electrolyte surfaces y-axis	1.3	2.5	2.6	9.3	17.3*	40.7*

*The value is higher than the maximum allowable thermal gradient (10 °C/cm)

Chapter 7

Contributions, Conclusions and Future Work

In this chapter, the main contributions and findings from this thesis are summarized. In addition, further steps to improve this MSc thesis will be explained.

7.1 Contributions

In this master's thesis, experimental setups and computational fluid dynamics (CFD) models were designed to study the performance of solid oxide fuel cells (SOFCs) in order to optimise the design and performance of both tubular and planar SOFCs. For SOFC CFD modeling, several types of modeling approaches and software packages were developed. In this thesis, fluid dynamics, heat transfer, electrochemical reactions, and different aspects of SOFC performance were studied using the Ansys Fluent fuel cell package.

- **Design of experiments for SOFCs performance and temperature measurements:** Initially, a literature review was carried out to look into the experimental and modeling approach associated with tubular and planar solid oxide fuel cells (SOFCs) to determine any existing research gaps and identify the thesis objectives. Subsequently, two separate experimental setups were developed to investigate tubular and planar solid oxide fuel cells (SOFCs), which will be utilized to validate the SOFCs models and to study various operation and structural parameters as well.

- **0D and 3D models for tubular cell:** Then, two separate models were developed for the tubular cell. The first one is a zero-dimensional model, which is mainly utilized to predict cell performance and cell overpotentials at various operating temperatures for control and real-time diagnostic purposes. While the second model is a three-dimensional computational fluid dynamics (CFD) model used to analyse the impact of operating temperature and structural parameters, including anode porosity, anode thickness, and electrolyte thickness, on the performance of tubular cell. Additionally, this model provides predictions for the temperature distribution, heat generation, and the fuel and air mass fractions across the cell.

- **3D models for planar cell:** Meanwhile, another three-dimensional computational fluid dynamics (CFD) model for planar cell was developed to study the effect of operating temperature and structural parameters, including anode porosity, anode thickness, and electrolyte thickness, on the performance of a planar cell. Also, predicting the temperature distribution and the thermal gradients at each cell's layer anode, cathode, and electrolyte. Moreover, predicting the the fuel and air mass fractions across the cell.

- **Tubular and planar models validation:** The tubular cell model was validated using internal experimental data based on tubular cell current density measurements and thermocouples readings, while the planar cell model was validated using internal experimental data based on planar cell current density measurements only. The mesh sensitivity analysis was conducted for both CFD models to ensure the two model results are mesh independent and the two models show an average error values equal to 5%.

- **Parametric analysis:** In the parametric analysis section, several structural cell parameters were investigated for tubular and planar cells, which have a significant effect on the SOFCs performance. The studied parameters are the effects of changing anode layer porosity, anode layer thickness, and electrolyte thickness.

- **Thermal gradients analysis:** The thermal gradient across the planar cell layer was studied, which is caused by the differential in temperature between the cell's hot and cold

zones. Hot zones are where hydrogen oxidation reactions take place, while cold zones are where oxygen reductions take place. The temperature gradient can cause thermal stresses in the cell, which can lead to cracking or failure of the cell. Therefore, estimating the temperature gradient across a cell plays a great role in understanding the degradation mechanism of the cell.

A thermal gradient analysis was carried out to study the effect of operation conditions on the temperature distribution and thermal gradients across the planar cell and to identify unhealthy operating conditions with high thermal gradient values that could cause the cell to breakdown. By improving the fuel cell design to have a low thermal gradient and using materials with a low coefficient of thermal expansion, the stresses caused by thermal gradients could be reduced, and the fuel cell's life could potentially be extended. Overall, managing thermal gradients is an important aspect of designing and operating SOFCs to ensure their long-term performance and durability.

7.2 Conclusions

Major findings from this thesis are as follow:

- The tubular zero-dimensional model shows the effect of the operating temperature on the cell overpotentials and performance. It is observed that a decrease in the cell temperature by 15% may result in a significant rise in the cell activation overpotential by 150% and a more than three-times increase in the ohmic overpotential at constant current density, but on the other hand, it doesn't have a significant effect on the concentration overpotential.

- Parametric analysis of the tubular and planar models shows that porosity has two independent effects. The activation rises with increasing porosity, whereas the concentration overpotential falls. With the combined effect, cells operate optimally at porosity values between 0.2 and 0.4.

- Regarding the thickness of the anode layer, it is observed that while an increase in anode thickness results in a slight rise in the cell's ohmic overpotential, a thicker anode layer

causes a higher concentration overpotential due to its significant effect on limiting gas mass transfer.

- The reduction in the thickness of the electrolyte layer leads to a drop in the ohmic overpotential. However, it is important to note that an excessive decrease in the thickness of the electrolyte may have a negative impact on the durability and stability of the fuel cell.

- The thermal gradient analysis at various operating conditions provided helpful insights into the thermal gradient values observed at each layer of the cell. This analysis allows for the identification of areas where the cell thermal gradient exceeds the threshold of 10 °C/cm, which can lead to cell damage. Additionally, it is demonstrate that the more uniform temperature distribution, the higher the cell performance. The results show the output power density of the healthy cell operating conditions is 10% higher than that of the unhealthy cell operating conditions.

- The results of this study demonstrate that CFD modeling is a very powerful tool for SOFC research and development. The developed CFD model can be used to optimise both structural and operational SOFC parameters to maximise efficiency and performance and reduce the degradation rate of SOFCs.

7.3 Future Work

Here are several potential areas of future work for extending the outcomes from this thesis:

- Stack design and fabrication: The CFD model can be expanded to design a SOFC stack containing a number of single cells. The CFD model can be used to estimate the cell performance and thermal management of the whole stack; therefore, not only the stack electrical energy but also the generated thermal energy can be utilised for various heating applications to maximise the stack efficiency.

- Optimization: To increase the efficiency and durability of SOFCs, the design and operational parameters may be optimised using CFD models. This includes investigating a

wide range of design and operational parameters not only the operating temperature, but also, including the cell's shape, the fuel and air channels design, and the pressure, and flow rate of reactants.

- Advanced modeling techniques: The use of advanced modeling techniques, such as machine learning and artificial intelligence, and their integration with CFD modeling can enhance the accuracy and speed of the cell optimisation process.

- Transient CFD analysis: Analyzing the kinetics of each reaction, fluid dynamics, and mass transfer with respect to time can be very beneficial to understanding the behavior of SOFCs during startup, shutdown, operating conditions variations, and load changes.

- Experimental testing set-up: There are several improvements that can be implemented in both planar and tubular cells in the experimental testing setup to collect data about the temperature distribution and thermal gradient at stack level. Moreover, failure modes such as thermal cycling fatigue, sealing failure, fuel starvation, and voltage instabilities can be intentionally designed and tested to provide data for fault diagnosis models.

- Various fuel types: CFD analysis can be used to evaluate the SOFC performance and its environmental effect with using fuels that may be locally available, such as natural gas, biogas, and syngas.

Bibliography

[1] IEA, "International energy agency world energy outlook 2022," IEA Paris, France, 2022.

[2] H. Davy, *The Collected Works of Sir Humphry Davy: Agricultural lectures, pt. 2, and other lectures*. Johnson Reprint Corporation, 1840.

[3] R. Meldola, *Christian friedrich schönbein, 1799–1868. ein blatt zur geschichte des 19. jahrhunderts*, 1900.

[4] A. B. Stambouli and E. Traversa, "Fuel cells, an alternative to standard sources of energy," *Renewable and sustainable energy reviews*, vol. 6, no. 3, pp. 295–304, 2002.

[5] M. T. Gencoglu and Z. Ural, "Design of a pem fuel cell system for residential application," *international journal of hydrogen energy*, vol. 34, no. 12, pp. 5242–5248, 2009.

[6] A. Kirubakaran, S. Jain, and R. Nema, "A review on fuel cell technologies and power electronic interface," *Renewable and sustainable energy reviews*, vol. 13, no. 9, pp. 2430–2440, 2009.

[7] H. Guo, C. F. Ma, M. H. Wang, J. Yu, X. Liu, and F. Ye, "Heat and mass transfer and two phase flow in hydrogen proton exchange membrane fuel cells and direct methanol fuel cells," in *International Conference on Fuel Cell Science, Engineering and Technology*, vol. 36681, 2003, pp. 471–476.

[8] C. Marks, E. A. Rishavy, and F. A. Wyczalek, "Electrovan—a fuel cell powered vehicle," *SAE Transactions*, pp. 992–1028, 1968.

[9] G. Weaver and S. Barrett, "Marine applications of fuel cell technology," *Fuel Cells Bulletin*, vol. 2003, no. 1, pp. 11–12, 2003.

[10] T. Yoshida and K. Kojima, "Toyota mirai fuel cell vehicle and progress toward a future hydrogen society," *The Electrochemical Society Interface*, vol. 24, no. 2, p. 45, 2015.

[11] D. of Materials Science & Metallurgy, "Types of fuel cells," *The Electrochemical Society Interface*, 2006.

[12] A. B. Stambouli and E. Traversa, "Solid oxide fuel cells (sofcs): A review of an environmentally clean and efficient source of energy," *Renewable and sustainable energy reviews*, vol. 6, no. 5, pp. 433–455, 2002.

[13] R. O'hayre, S.-W. Cha, W. Colella, and F. B. Prinz, *Fuel cell fundamentals*. John Wiley & Sons, 2016, ch. 8.

[14] K. Wang, D. Hissel, M.-C. Péra, N. Steiner, and D. Marra, "A review on solid oxide fuel cell models," *International journal of hydrogen energy*, vol. 36, no. 12, pp. 7212–7228, 2011.

[15] G. De Lorenzo and P. Fragiacomo, "Energy analysis of an sofc system fed by syngas," *Energy Conversion and Management*, vol. 93, pp. 175–186, 2015.

[16] M. Z. Khan, A. Iltaf, H. A. Ishfaq, and F. N. Khan, "Flat-tubular solid oxide fuel cells and stacks: A review," *Journal of Asian Ceramic Societies*, vol. 9, no. 3, pp. 745–770, 2021.

[17] J. W. Fergus, "Electrolytes for solid oxide fuel cells," *Journal of power sources*, vol. 162, no. 1, pp. 30–40, 2006.

[18] E. V. Tsipis and V. V. Kharton, "Electrode materials and reaction mechanisms in solid oxide fuel cells: A brief review: Ii. electrochemical behavior vs. materials science aspects," *Journal of Solid State Electrochemistry*, vol. 12, pp. 1367–1391, 2008.

[19] B. S. Prakash, S. S. Kumar, and S. Aruna, "Properties and development of ni/ysz as an anode material in solid oxide fuel cell: A review," *Renewable and Sustainable Energy Reviews*, vol. 36, pp. 149–179, 2014.

[20] K. A. Kuterbekov, A. V. Nikonov, K. Z. Bekmyrza, and N. B. Pavzderin, "Classification of solid oxide fuel cells," *Nanomaterials*, vol. 12, no. 7, p. 1059, 2022.

[21] T. Estell, "Performance of solid oxide fuel cell electrodes," in *Proceedings of the Workshop on High Temperature Solid Oxide Fuel Cells*, 1977.

[22] M. Dokiya, "Sofc system and technology," *Solid State Ionics*, vol. 152, pp. 383–392, 2002.

[23] K. Kendall, "Progress in solid oxide fuel cell materials," *International materials reviews*, vol. 50, no. 5, pp. 257–264, 2005.

[24] N. Mahato, A. Banerjee, A. Gupta, S. Omar, and K. Balani, "Progress in material selection for solid oxide fuel cell technology: A review," *Progress in Materials Science*, vol. 72, pp. 141–337, 2015.

[25] S. Hussain and L. Yangping, "Review of solid oxide fuel cell materials: Cathode, anode, and electrolyte," *Energy Transitions*, vol. 4, pp. 113–126, 2020.

[26] J.-H. Lee, J.-W. Heo, D.-S. Lee, J Kim, G.-H. Kim, and H.-W. Lee, "The impact of anode microstructure on the power generating characteristics of sofc," *Solid State Ionics*, vol. 158, no. 3-4, pp. 225–232, 2003.

[27] Z. Jiao, N. Shikazono, and N. Kasagi, "Quantitative characterization of sofc nickel-ysz anode microstructure degradation based on focused-ion-beam 3d-reconstruction technique," *Journal of the Electrochemical Society*, vol. 159, no. 3, B285, 2012.

[28] S. D. Vora, G. Jesionowski, and M. C. Williams, "Overview of us department of energy office of fossil energy's solid oxide fuel cell program for fy2019," *ECS Transactions*, vol. 91, no. 1, p. 27, 2019.

[29] T Ackmann, L. De Haart, W Lehnert, and D Stolten, "Modeling of mass and heat transport in planar substrate type sofcs," *Journal of The Electrochemical Society*, vol. 150, no. 6, A783, 2003.

[30] Y. M. Barzi, A Raoufi, and H Lari, "Performance analysis of a sofc button cell using a cfd model," *international journal of hydrogen energy*, vol. 35, no. 17, pp. 9468–9478, 2010.

[31] E Achenbach, "Three-dimensional and time-dependent simulation of a planar solid oxide fuel cell stack," *Journal of power sources*, vol. 49, no. 1-3, pp. 333–348, 1994.

[32] J. Ferguson, J. M. Fiard, and R. Herbin, "Three-dimensional numerical simulation for various geometries of solid oxide fuel cells," *Journal of Power Sources*, vol. 58, no. 2, pp. 109–122, 1996.

[33] K. P. Recknagle, R. E. Williford, L. A. Chick, D. R. Rector, and M. A. Khaleel, "Three-dimensional thermo-fluid electrochemical modeling of planar sofc stacks," *Journal of Power Sources*, vol. 113, no. 1, pp. 109–114, 2003.

[34] C. Huang, S. Shy, and C. Lee, "On flow uniformity in various interconnects and its influence to cell performance of planar sofc," *Journal of Power Sources*, vol. 183, no. 1, pp. 205–213, 2008.

[35] S. Hosseini, K. Ahmed, and M. O. Tadé, "Cfd model of a methane fuelled single cell sofc stack for analysing the combined effects of macro/micro structural parameters," *Journal of Power Sources*, vol. 234, pp. 180–196, 2013.

[36] I. Khazaee and A. Rava, "Numerical simulation of the performance of solid oxide fuel cell with different flow channel geometries," *Energy*, vol. 119, pp. 235–244, 2017.

[37] Y. M. Chellehbari, K. Adavi, J. S. Amin, and S. Zendehboudi, "A numerical simulation to effectively assess impacts of flow channels characteristics on solid oxide fuel cell performance," *Energy Conversion and Management*, vol. 244, p. 114 280, 2021.

[38] K. I. Ahmed and M. H. Ahmed, "Developing a novel design for a tubular solid oxide fuel cell current collector," *Applied Sciences*, vol. 12, no. 12, p. 6003, 2022.

[39] J. R. Izzo Jr, A. A. Peracchio, and W. K. Chiu, "Modeling of gas transport through a tubular solid oxide fuel cell and the porous anode layer," *Journal of Power Sources*, vol. 176, no. 1, pp. 200–206, 2008.

[40] M. Ni, M. K. Leung, and D. Y. Leung, "Parametric study of solid oxide fuel cell performance," *Energy Conversion and Management*, vol. 48, no. 5, pp. 1525–1535, 2007.

[41] S. Yang, T. Chen, Y. Wang, Z. Peng, and W. G. Wang, "Electrochemical analysis of an anode-supported sofc," *International Journal of Electrochemical Science*, vol. 8, no. 2, pp. 2330–2344, 2013.

[42] A. Yahya, D. Ferrero, H. Dhahri, P. Leone, K. Slimi, and M. Santarelli, "Electrochemical performance of solid oxide fuel cell: Experimental study and calibrated model," *Energy*, vol. 142, pp. 932–943, 2018.

[43] A. K. ElKashat, A. R. Razmi, S. Vafaeenezhad, A. R. Hanifi, T. H. Etsell, and M. Shahbakhti, "Experimental and thermodynamic analyses of a novel anode supported solid oxide fuel cell," *The Canadian Society for Mechanical Engineering (CSME)*, 2022.

[44] D. Noren and M. A. Hoffman, "Clarifying the butler–volmer equation and related approximations for calculating activation losses in solid oxide fuel cell models," *Journal of Power Sources*, vol. 152, pp. 175–181, 2005.

[45] S. Haji, "Analytical modeling of pem fuel cell i–v curve," *Renewable Energy*, vol. 36, no. 2, pp. 451–458, 2011.

[46] S. L. Puthran, "3-dimensional computational fluid dynamics modeling of solid oxide fuel cell using different fuels," Ph.D. dissertation, Missouri University of Science and Technology, 2011.

[47] J. R. Selman and C. W. Tobias, "Mass-transfer measurements by the limiting-current technique," in *Advances in chemical engineering*, vol. 10, Elsevier, 1978, pp. 211–318.

[48] H. M. Schey and H. M. Schey, *Div, grad, curl, and all that: an informal text on vector calculus*. WW Norton New York, NY, USA: 2005.

[49] K Vafai and S. Kim, "On the limitations of the brinkman-forchheimer-extended darcy equation," *International Journal of Heat and Fluid Flow*, vol. 16, no. 1, pp. 11–15, 1995.

[50] E. L. Cussler, *Diffusion: mass transfer in fluid systems*. Cambridge university press, 2009.

[51] R. T. Nishida, *Computational fluid dynamics modelling of solid oxide fuel cell stacks*. Queen's University (Canada), 2013.

[52] "Fuel cells module manual 12.0," *Theory Guide*, 2009.

[53] H. Ren, Y. H. Lee, E. A. Wu, and H. Chung, "Nano-ceramic cathodes via co-sputtering of gd–ce alloy and lanthanum strontium cobaltite for low-temperature thin-film solid oxide fuel cells," *ACS Applied Energy Materials*, vol. 3, no. 9, pp. 8135–8142, 2020.

[54] M. Chyu, "Numerical modeling of transport phenomena in solid oxide fuel cells," in *2005 Taiwan Solid Oxide Fuel Cell Symposium*, 2005.

[55] G. Anandakumar, N. Li, A. Verma, P. Singh, and J.-H. Kim, "Thermal stress and probability of failure analyses of functionally graded solid oxide fuel cells," *Journal of Power Sources*, vol. 195, no. 19, pp. 6659–6670, 2010.

[56] S. Horr, H. Mohcene, H. Bouguettaia, and H. B. Moussa, "Performance analysis of as-sofc fuel cell combining single and sinusoidal flow field: Numerical study," *Renewable Energy and Environmental Sustainability*, vol. 6, p. 18, 2021.

[57] P. Aguiar, C. Adjiman, and N. Brandon, "Anode-supported intermediate-temperature direct internal reforming solid oxide fuel cell: Ii. model-based dynamic performance and control," *Journal of Power Sources*, vol. 147, no. 1-2, pp. 136–147, 2005.

[58] H. Yoshida and H. Iwai, "Thermal management in solid oxide fuel cell systems," in *Proceedings of fifth international conference on enhanced, compact and ultra-compact heat exchangers: science, engineering and technology, Engineering Conferences International, Hoboken, NJ, USA*, 2005.

[59] J. Yu, Y. Wang, S. Weng, and Y. Hui, "The effect of anode porosity on the performance of planar electrode supported solid oxide fuel cell," in *International Conference on Micro/Nanoscale Heat Transfer*, vol. 43901, 2009, pp. 259–264.

[60] J.-W. Kim and A. V. Virkar, "The effect of anode thickness on the performance of anode-supported solid oxide fuel cells," *ECS Proceedings Volumes*, vol. 1999, no. 1, p. 830, 1999.

[61] J. M. Park, D. Y. Kim, J. D. Baek, Y.-J. Yoon, P.-C. Su, and S. H. Lee, "Effect of electrolyte thickness on electrochemical reactions and thermo-fluidic characteristics inside a sofc unit cell," *Energies*, vol. 11, no. 3, p. 473, 2018.

Appendix A: Planar SOFC stack assembly procedures

1. The four bolts are fixed on the lower plate, which has the inlet and outlet fuel and oxidant pipes.

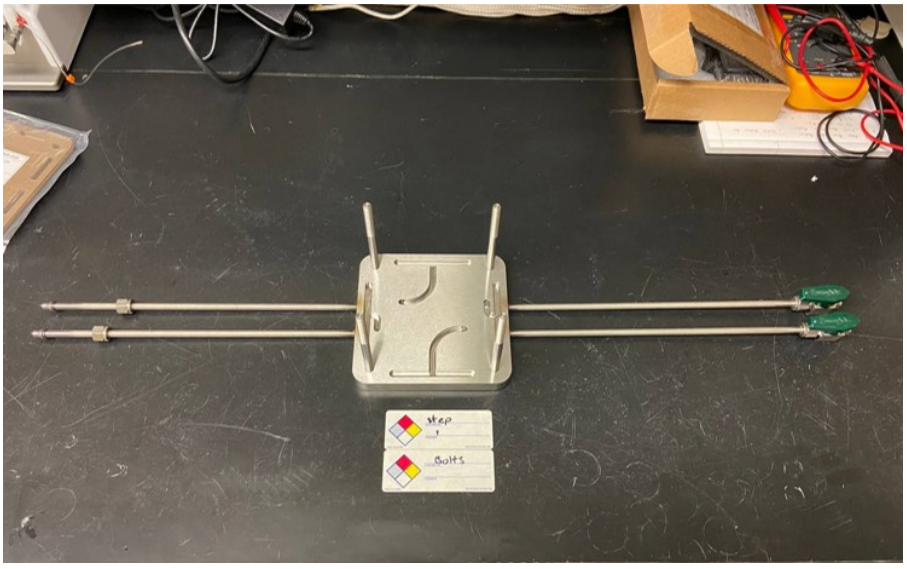

Figure A.1: Planar SOFC stack assembly step 1

2. Install the isolation plate, 0.5 mm thick, on top of the lower plate guided through the four bolts.

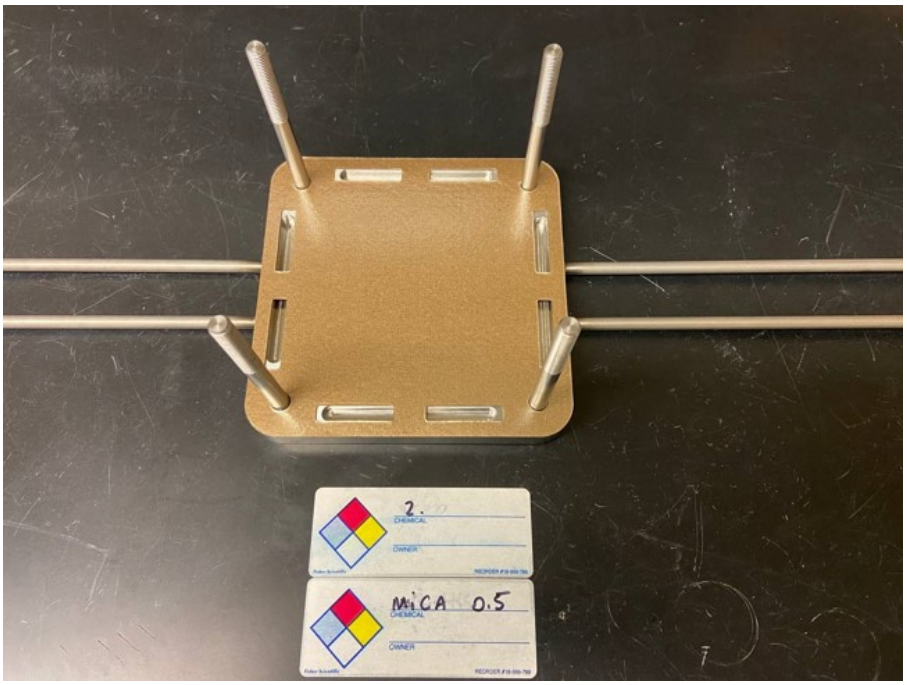

Figure A.2: Planar SOFC stack assembly step 2

3. Install the fuel side end plate on top of the isolation plate, guided by the four bolts, with the fuel channel facing up.

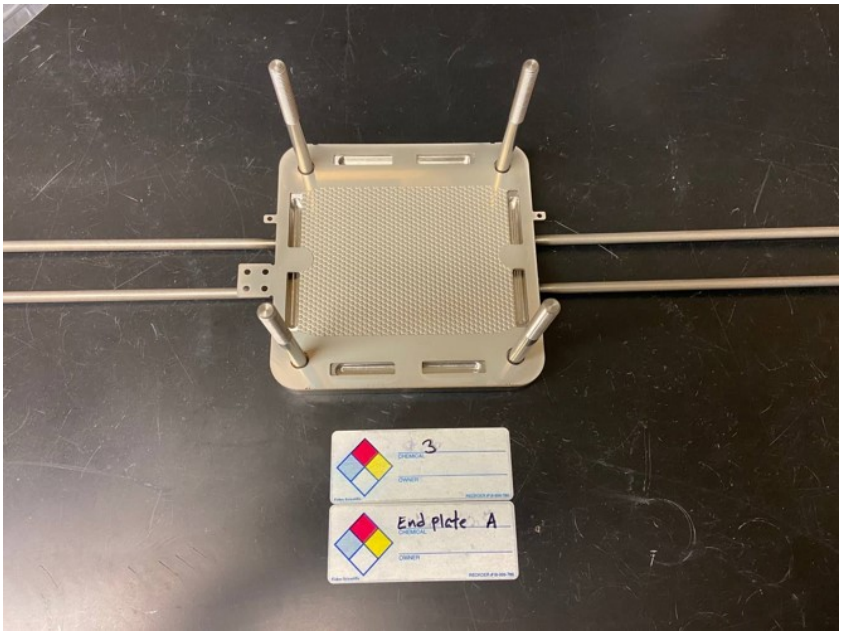

Figure A.3: Planar SOFC stack assembly step 3

4. Install the metal spacer, 0.2 mm thick, on top of the fuel side end plate, guided through the four bolts.

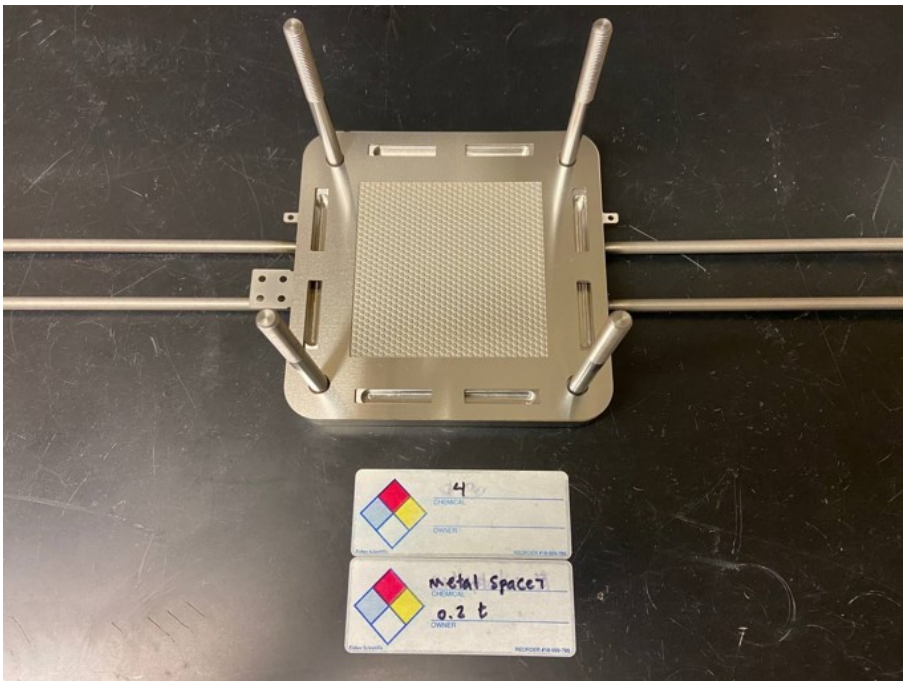

Figure A.4: Planar SOFC stack assembly step 4

5. Install the nickel mesh current collector on the space inside the metal spacer.

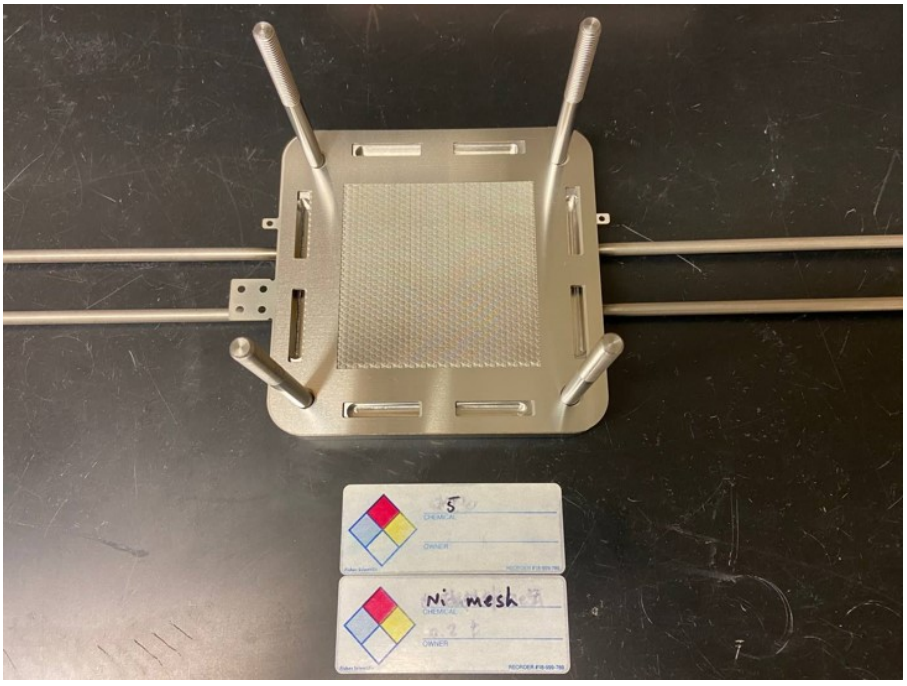

Figure A.5: Planar SOFC stack assembly step 5

6. Install the two metal spacers, 0.2 mm in thick, on top of the nickel mesh, guided through the four bolts.

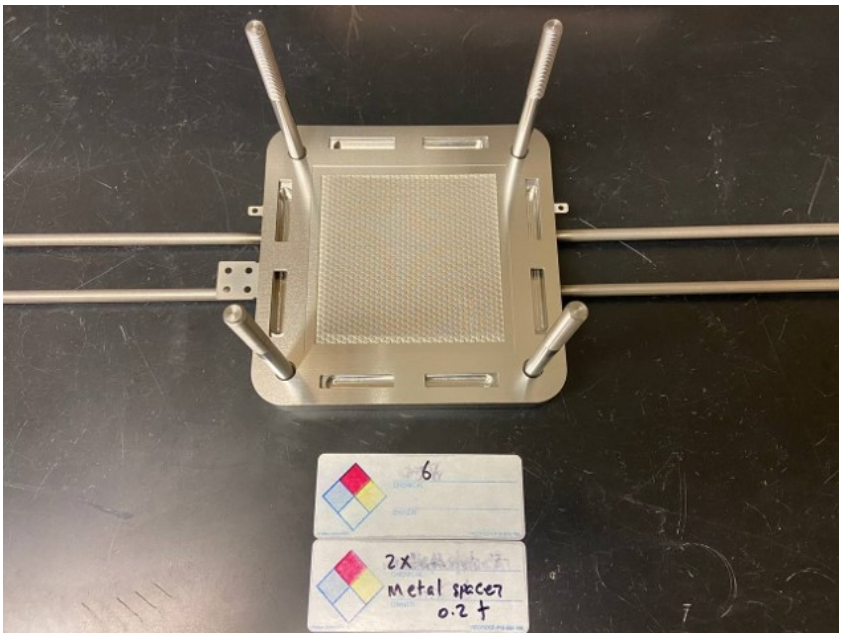

Figure A.6: Planar SOFC stack assembly step 6

7. Install the planar SOFC cell with anode facing down on the space inside the metal spacer and touching the nickel mesh.

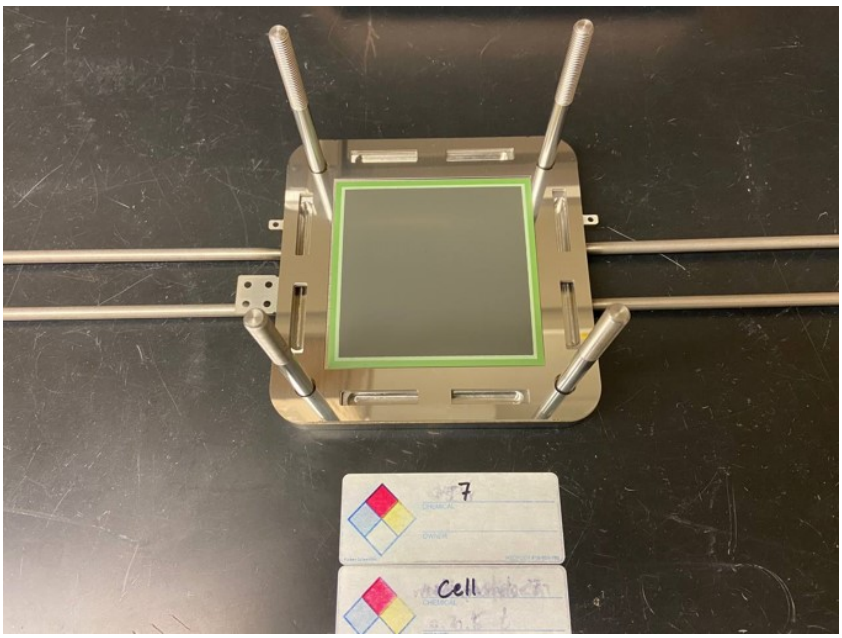

Figure A.7: Planar SOFC stack assembly step 7

8. Install the isolation spacer, 0.15 mm thick on top of the cell guided through the four bolts.

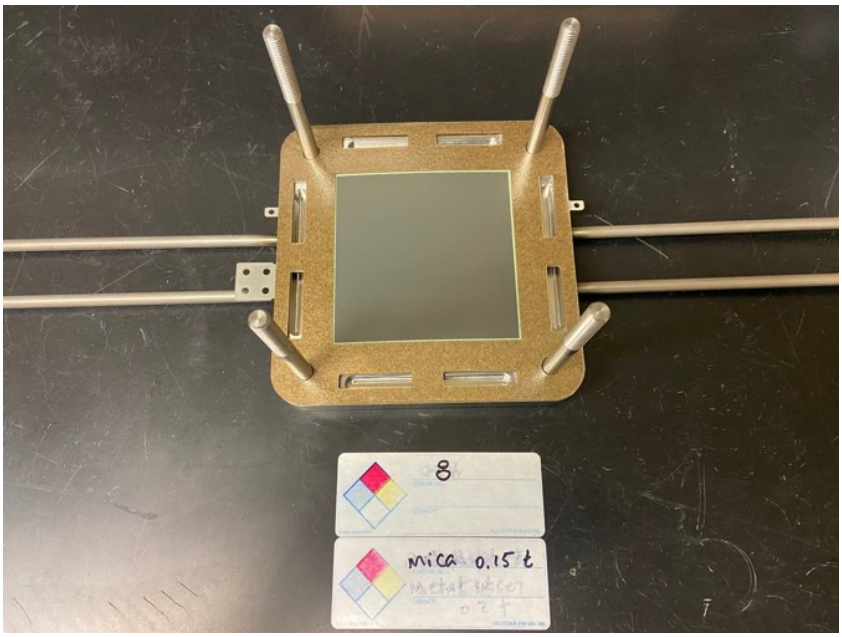

Figure A.8: Planar SOFC stack assembly step 8

9. Install the crofer mesh current collector on the space inside the isolation plate and touching the cell cathode side.

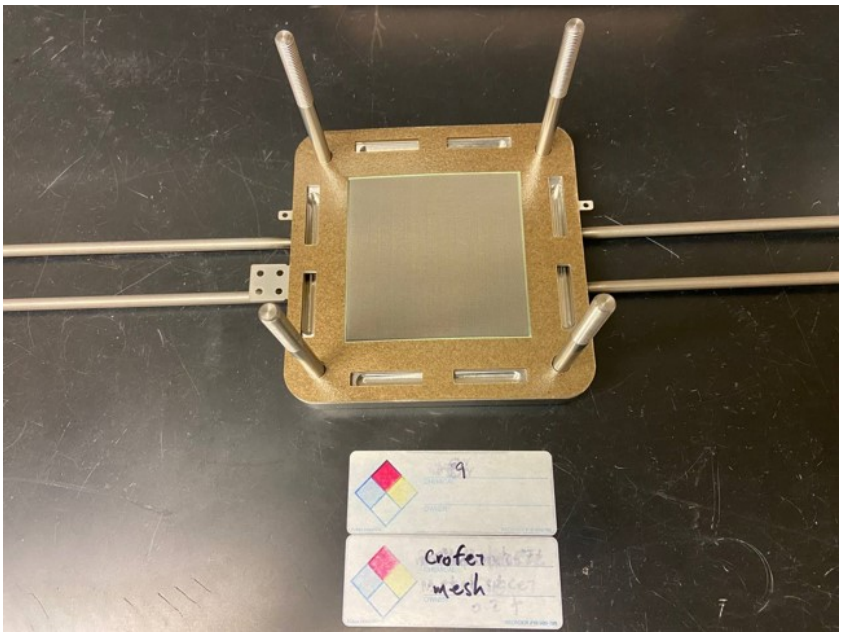

Figure A.9: Planar SOFC stack assembly step 9

10. If the stack has multiple cells, install the interconnect on top of the isolation plate, guided by the four bolts, and if the stack has a single cell, go directly to step 12.

11. Repeat the steps from 4 to 10

12. Install the oxidant side end plate on top of the isolation plate, guided by the four bolts, with the air channel facing down.

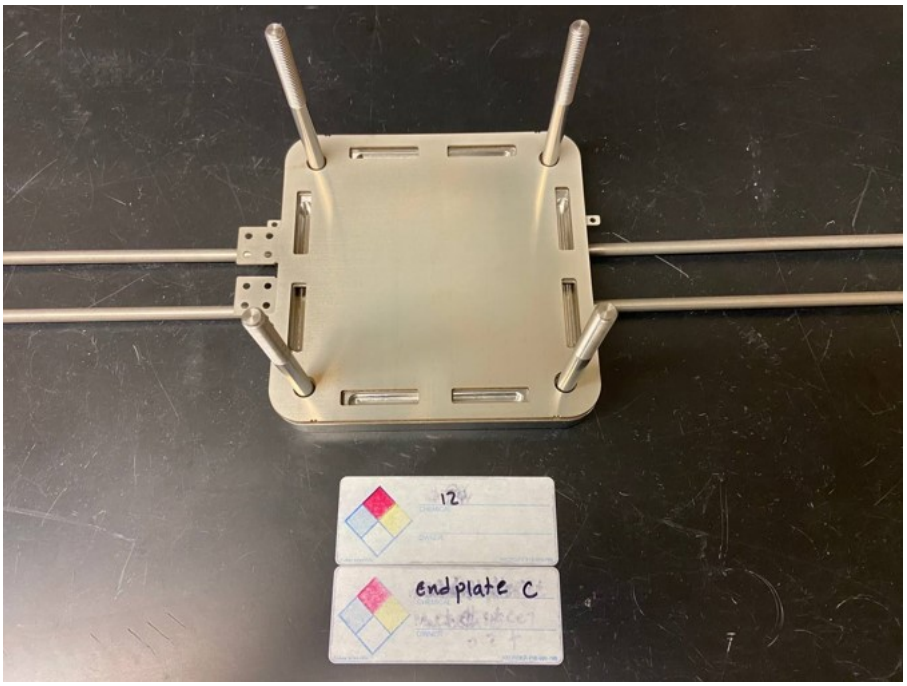

Figure A.10: Planar SOFC stack assembly step 12

13. Install the isolation plate, 0.5 mm thick, on top of the oxidant side end plate guided through the four bolts.

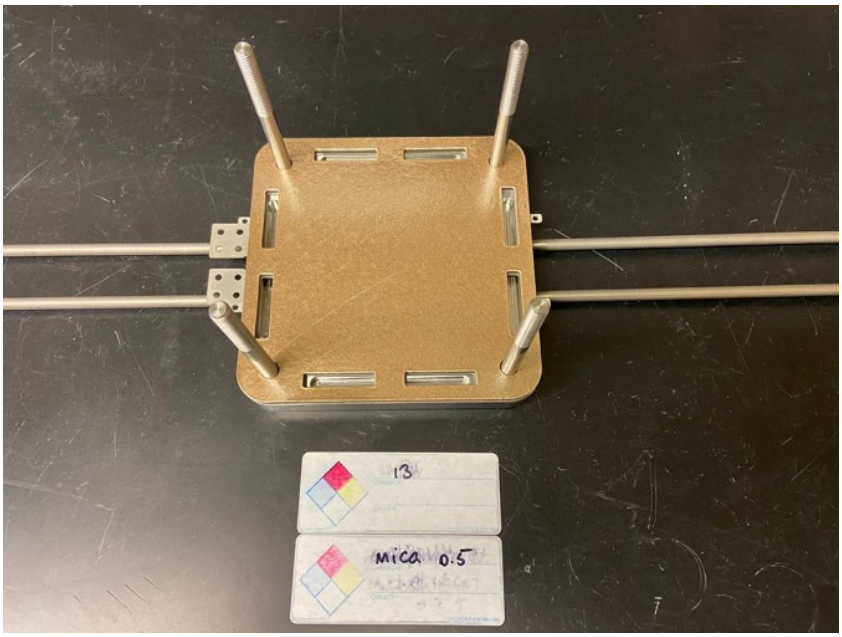

Figure A.11: Planar SOFC stack assembly step 13

14. Install the upper plate on top of the isolation plate, 0.5 mm thick guided through the four bolts.

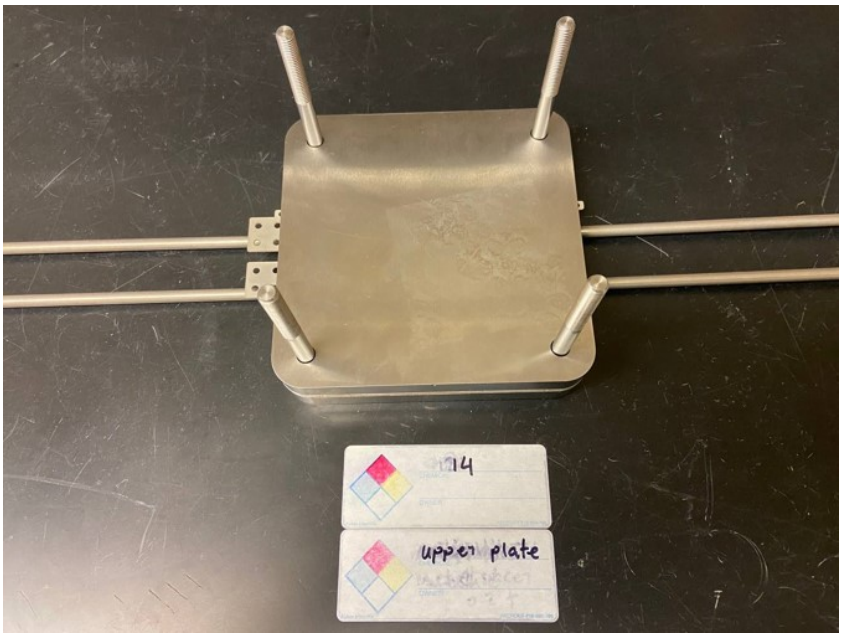

Figure A.12: Planar SOFC stack assembly step 14

15. Install the four sleeves on top of the upper plate through the four bolts.

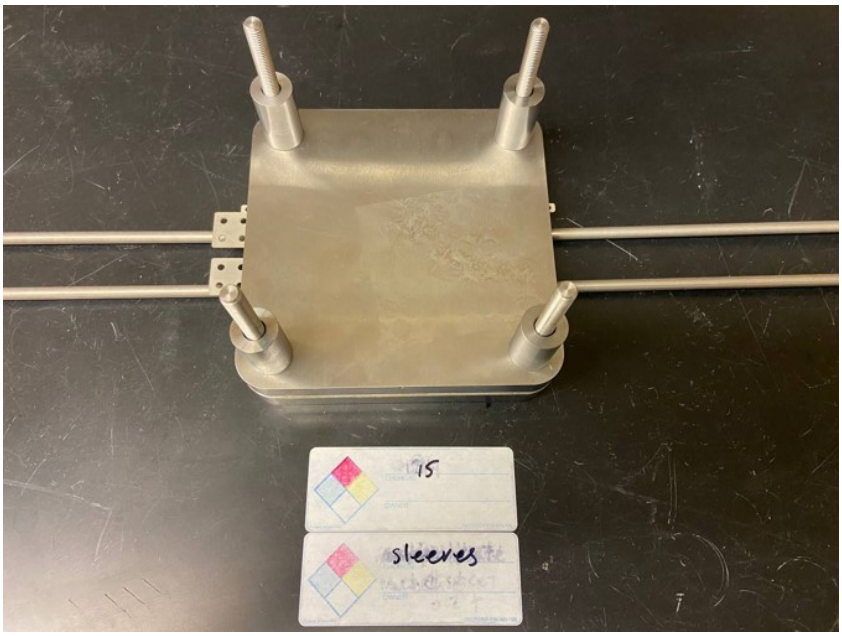

Figure A.13: Planar SOFC stack assembly step 15

16. Install the four ceramic springs on top of the upper plate, guided by the four sleeves.

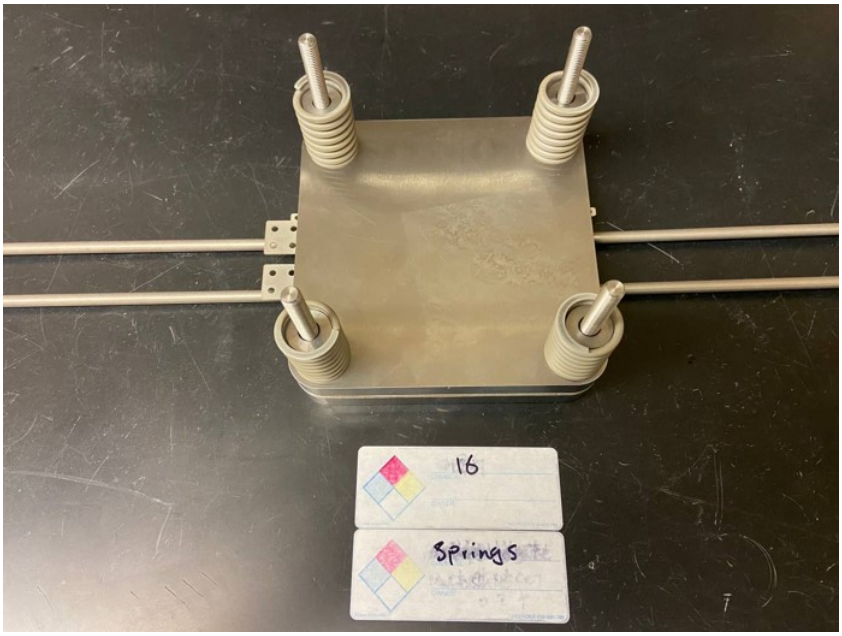

Figure A.14: Planar SOFC stack assembly step 16

17. Install the springs fix plate on top of the four springs, guided by the four bolts.

Figure A.15: Planar SOFC stack assembly step 17

18. Tighten the four nuts against the springs fix plate to provide external compression to the stack components.

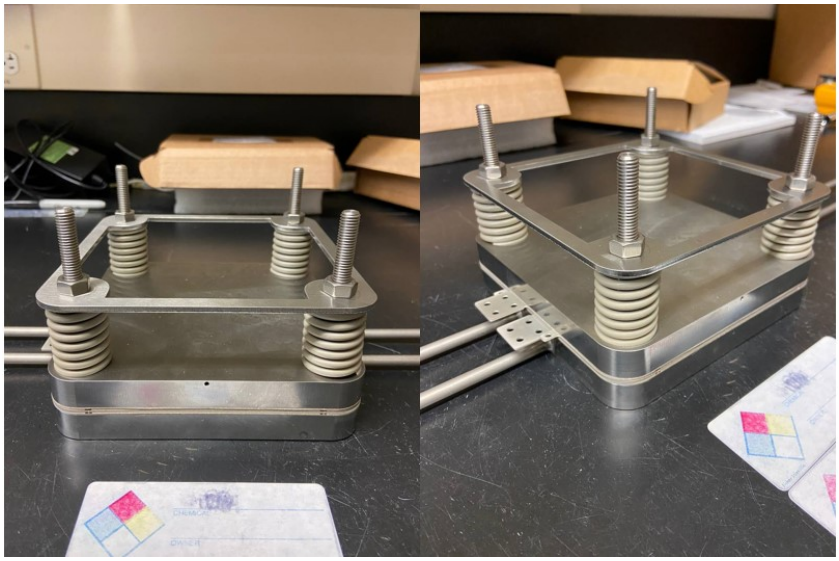

Figure A.16: Planar SOFC stack assembly step 18

Appendix B: Program and Data File Summary

The following files were used in this thesis.

B.1 Chapter 1

Table B.1: Chapter 1 Figure files.

File name	File Description
Fuel cell types.jpg	Figure 1.1
Fuel cell types comparison.jpg	Figure 1.2
SOFC operating principle.png	Figure 1.3
SOFC reactions.png	Figure 1.4
Planar SOFC geometry.jpg	Figure 1.5 (a)
Tubular SOFC geometry.jpg	Figure 1.5 (b)
Self supporting SOFC.jpg	Figure 1.6

B.2 Chapter 2

Table B.2: Chapter 2 Figure files.

File name	File Description
Planar experiment schematic.jpg	Figure 2.1
Planar experiment components.jpg	Figure 2.2
Elcogen cell.jpg	Figure 2.3 (a)
Elcogen cell schematic.jpg	Figure 2.3 (b)
Tubular experiment schematic.jpg	Figure 2.4
thermocouples placement.jpg	Figure 2.5

B.3 Chapter 4

Table B.3: Chapter 4 Figure files.

File name	File Description
Tubular 0-D validation.png	Figure 4.1
Operating temperature effect 0-D.png	Figure 4.2
Activation overpotential 0-D.png	Figure 4.3
Ohmic overpotential 0-D.png	Figure 4.4
Concentration overpotential 0-D.png	Figure 4.5
Tubular SOFC geometry.jpg	Figure 4.6
Tubular cell SEM image.png	Figure 4.7
Tubular mesh independence.png	Figure 4.8
Tubular grid comparison.png	Figure 4.9
Tubular cell mesh side view.jpg	Figure 4.10 (a)
Tubular cell mesh isometric view.jpg	Figure 4.10 (b)
Tubular 3-D validation.png	Figure 4.11
Tubular 3-D temperature validation.png	Figure 4.12
Tubular 3-D IV and heat.png	Figure 4.13
Tubular 3-D hydrogen mf.png	Figure 4.14
Tubular 3-D oxygen mf.png	Figure 4.15

Table B.4: Chapter 4 models files.

File name	File Description
Tubular 0-D model.m	Figure 4.1
	Figure 4.2
	Figure 4.3
	Figure 4.4
	Figure 4.5
Tubular cfd model.wbpj	Figure 4.6
	Figure 4.10 (a)
	Figure 4.10 (b)
	Figure 4.14
	Figure 4.15

Table B.5: Chapter 4 results files.

File name	File Description
Tubular 0-D validation.xlsx	Figure 4.1
Operating temperature effect 0-D.xlsx	Figure 4.2
Activation overpotential 0-D.xlsx	Figure 4.3
Ohmic overpotential 0-D.xlsx	Figure 4.4
Concentration overpotential 0-D.xlsx	Figure 4.5
Tubular 3-D validation.xlsx	Figure 4.11
Tubular 3-D temperature validation.xlsx	Figure 4.12
Tubular 3-D results.xlsx	Figure 4.13

B.4 Chapter 5

Table B.6: Chapter 5 Figure files.

File name	File Description
Planar exploded diagram.jpg	Figure 5.1
Planar stack isometric view.png	Figure 5.2
Planar mesh independence.png	Figure 5.3
Planar grid comparison.png	Figure 5.4
Planar cell mesh side view.png	Figure 5.5 (a)
Planar cell mesh isometric view.png	Figure 5.5 (b)
Planar cfd validation.png	Figure 5.6
Anode temperature profile.png	Figure 5.7
Anode temperature profile xz.png	Figure 5.8
Anode thermal gradient x.png	Figure 5.9
Anode temperature profile yz.png	Figure 5.10
Anode thermal gradient y.png	Figure 5.11
Cathode temperature profile.png	Figure 5.12
Cathode temperature profile xz.png	Figure 5.13
Cathode thermal gradient x.png	Figure 5.14
Cathode temperature profile yz.png	Figure 5.15
Cathode thermal gradient y.png	Figure 5.16
Electrolyte temperature profile.png	Figure 5.17
Electrolyte temperature profile xz.png	Figure 5.18
Electrolyte thermal gradient x.png	Figure 5.19
Electrolyte temperature profile yz.png	Figure 5.20
Electrolyte thermal gradient y.png	Figure 5.21
Planar hydrogen mf.png	Figure 5.22
Planar oxygen mf.png	Figure 5.23

Table B.7: Chapter 5 models files.

File name	File Description
Planar cfd model.wbpj	Figure 5.1
	Figure 5.2
	Figure 5.5
	Figure 5.7
	Figure 5.12
	Figure 5.17
	Figure 5.22
	Figure 5.23

Table B.8: Chapter 5 results files.

File name	File Description
Planar validation.xlsx	Figure 5.6
Planar cfd results.xlsx	Figure 5.9
	Figure 5.11
	Figure 5.14
	Figure 5.16
	Figure 5.19
	Figure 5.21

B.5 Chapter 6

Table B.9: Chapter 6 Figure files.

File name	File Description
Tubular anode porosity.png	Figure 6.1
Planar anode porosity.png	Figure 6.2
Tubular anode thickness.png	Figure 6.3
Planar anode thickness.png	Figure 6.4
Tubular electrolyte thickness.png	Figure 6.5
Planar electrolyte thickness.png	Figure 6.6
Planar rec operating conditions.png	Figure 6.7
Healthy anode temperature gradient x.png	Figure 6.8 (a)
Experiment anode temperature gradient x.png	Figure 6.8 (b)
Unhealthy anode temperature gradient x.png	Figure 6.8 (c)
Healthy anode temperature gradient y.png	Figure 6.9 (a)
Experiment anode temperature gradient y.png	Figure 6.9 (b)
Unhealthy anode temperature gradient y.png	Figure 6.9 (c)
Healthy cathode temperature gradient x.png	Figure 6.10 (a)
Experiment cathode temperature gradient x.png	Figure 6.10 (b)
Unhealthy cathode temperature gradient x.png	Figure 6.10 (c)
Healthy cathode temperature gradient y.png	Figure 6.11 (a)
Experiment cathode temperature gradient y.png	Figure 6.11 (b)
Unhealthy cathode temperature gradient y.png	Figure 6.11 (c)

Healthy electrolyte temperature gradient x.png	Figure 6.12 (a)
Experiment electrolyte temperature gradient x.png	Figure 6.12 (b)
Unhealthy electrolyte temperature gradient x.png	Figure 6.12 (c)
Healthy electrolyte temperature gradient y.png	Figure 6.13 (a)
Experiment electrolyte temperature gradient y.png	Figure 6.13 (b)
Unhealthy electrolyte temperature gradient y.png	Figure 6.13 (c)

Table B.10: Chapter 6 models files.

File name	File Description
Planar healthy model.wbpj	Figure 6.8 (a)
	Figure 6.8 (a)
	Figure 6.9 (a)
	Figure 6.10 (a)
	Figure 6.11 (a)
	Figure 6.12 (a)
	Figure 6.13 (a)
Planar cfd model.wbpj	Figure 6.8 (b)
	Figure 6.8 (b)
	Figure 6.9 (b)
	Figure 6.10 (b)
	Figure 6.11 (b)
	Figure 6.12 (b)
	Figure 6.13 (b)
Planar unhealthy model.wbpj	Figure 6.8 (a)
	Figure 6.8 (c)
	Figure 6.9 (c)
	Figure 6.10 (c)
	Figure 6.11 (c)
	Figure 6.12 (c)
	Figure 6.13 (c)

Table B.11: Chapter 6 results files.

File name	File Description
Anode temp gradient comparison.xlsx	Figure 6.8
	Figure 6.9
Cathode temp gradient comparison.xlsx	Figure 6.10
	Figure 6.11
Electrolyte temp gradient comparison.xlsx	Figure 6.12
	Figure 6.13

Appendix C: SEM images

The figure shows the SEM images for the studied tubular and planar cells. These images were used to determine the thickness of the anode function layer, the anode support layer, the electrolyte, and the cathode, as well as the porosity of the anode and cathode layers. These data were used in Chapters four and five to develop the SOFC models.

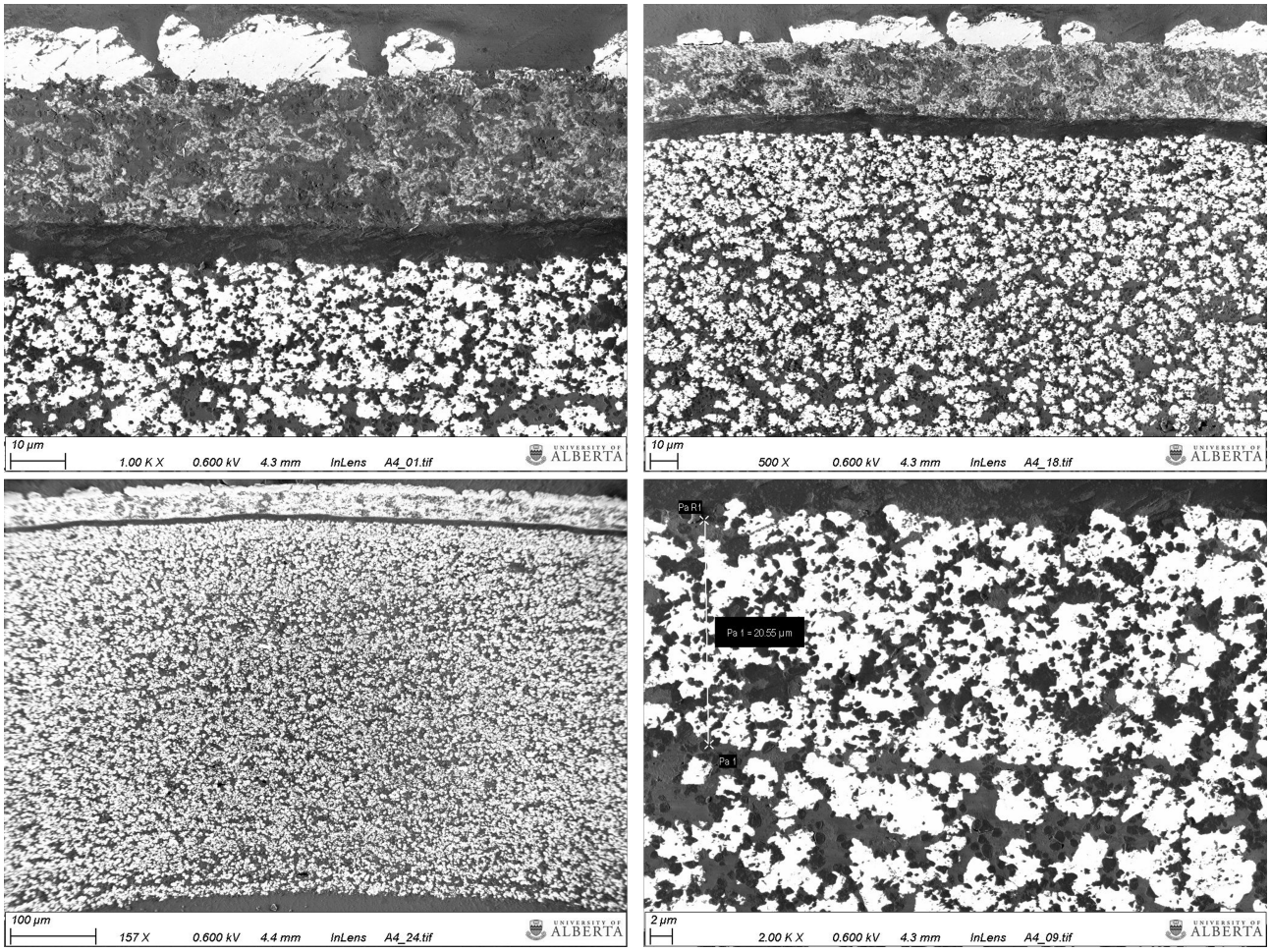

Figure C.1: Tubular cell SEM images.

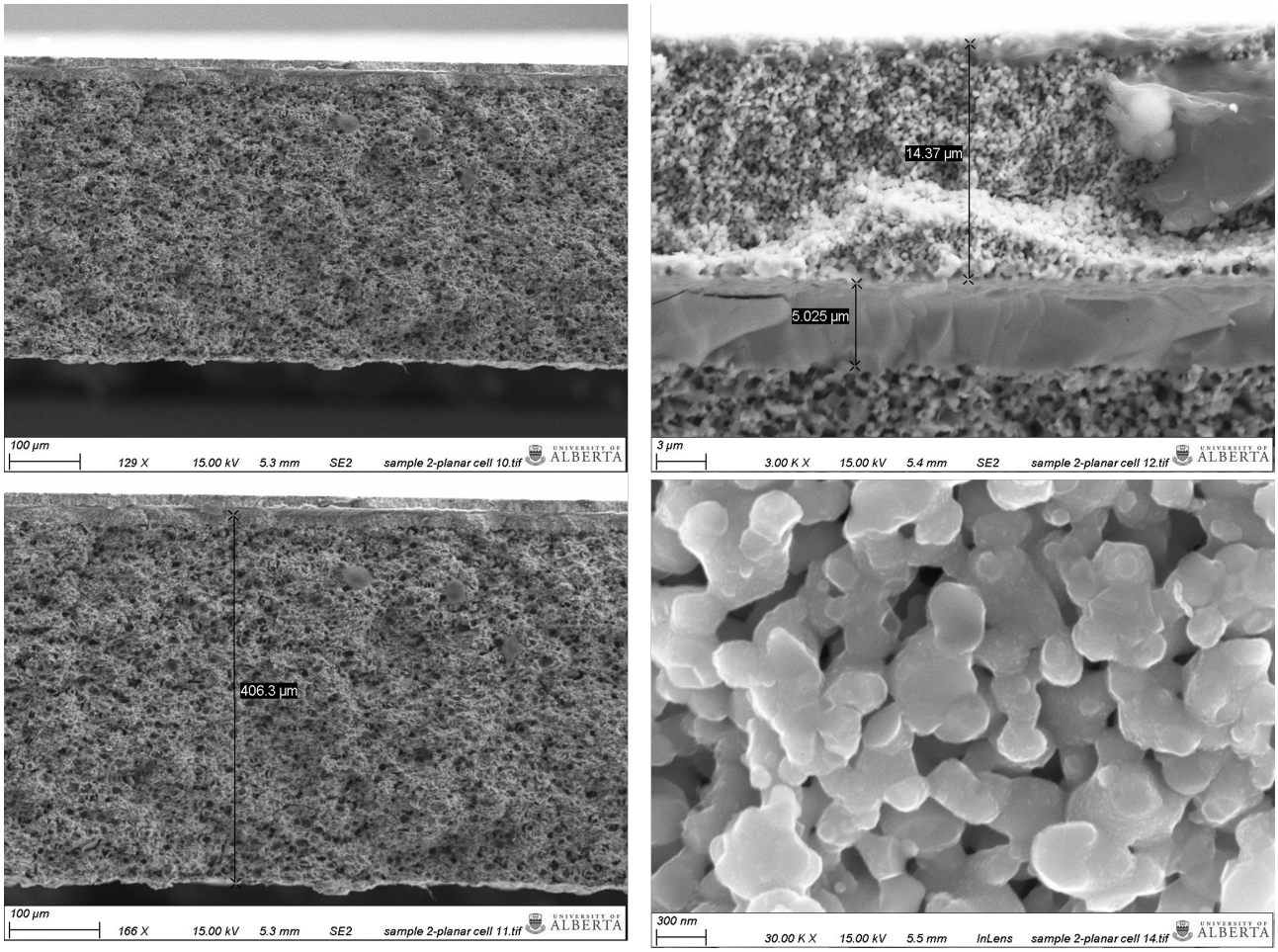

Figure C.2: Planar cell SEM images.

Appendix D: Ansys Fluent models structure

D.1 General

Solver:

- Pressure based.
- Absolute velocity formulation.
- Steady State.
- No gravity.

D.2 Models

- Multiphase – off
- Energy – on
- Viscous – Laminar
- Radiation – off
- Heat exchanger – off
- Species - Species Transport
- Discrete phase – off
- SOFC (Unresolved Electrolyte) - on

D.3 Materials

The materials properties for tubular cell components were selected based on the materials used in the fabrication (Table 4.1), while the materials of the planar cell as mentioned in the manufacturer data sheet (Table 5.1).

D.4 Boundary conditions

Table D.1: Boundary conditions for tubular and planar SOFC CFD models

Parameter	**Tubular**	**Planar**
Fuel inlet flow rate	50 SCCM	400 SCCM
Air inlet flow rate	100 SCCM	400 SCCM
Fuel inlet temperature	700 °C	100 °C
Fuel inlet temperature	700 °C	100 °C
Fuel outlet pressure	0 Psig	0 Psig
Fuel outlet pressure	0 Psig	0 Psig
Surrounding temperature	700 °C	650 °C

D.5 Solution Methods

Pressure velocity coupling:

- Scheme – Simple

Spatial discretization:

- Gradient – Least squares cell based
- Pressure – Second order
- Density – Second order upwind
- Momentum - Second order upwind
- Energy - Second order upwind

- Electric Potential - First order upwind
- Protonic Potential - First order upwind

D.6 Monitors

The convergence criterion values for all equations have been set the same for tubular and planar models.

Table D.2: The convergence criterion values

Equation	**Value**
Continuity	1e-5
X-velocity	1e-5
Y-velocity	1e-5
Z-velocity	1e-5
Energy	1e-6
H_2 mass fraction	1e-5
O_2 mass fraction	1e-5
H_2O mass fraction	1e-5
Current density	1e-5